


Kathryn Volk

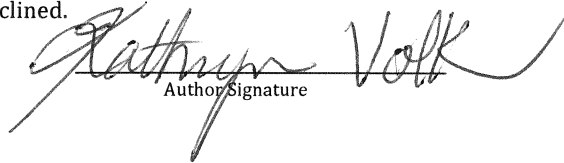
**Geological review of the Alaska-Aleutian Arc and exploration of 3D
subduction zone modeling**

submitted in partial fulfillment of the requirements for the degree of
Master of Science in Earth and Environmental Sciences
Department of Earth and Environmental Sciences
The University of Michigan

 Signature	Accepted by: <u>ERIC HETLAND</u>	<u>12/7/15</u> Date
<u>Jeroen Ritsema</u> Signature	Name <u>JEROEN RITSEMA</u>	<u>12/7/15</u> Date
<u>Chris J. Poulsen</u> Department Chair Signature	Name <u>Chris J. Poulsen</u>	<u>12/10/15</u> Date

I hereby grant the University of Michigan, its heirs and assigns, the non-exclusive right to reproduce and distribute single copies of my thesis, in whole or in part, in any format. I represent and warrant to the University of Michigan that the thesis is an original work, does not infringe or violate any rights of others, and that I make these grants as the sole owner of the rights to my thesis. I understand that I will not receive royalties for any reproduction of this thesis.

- Permission granted.
 Permission granted to copy after: _____
 Permission declined.


Author Signature



Abstract

The Alaska-Aleutian subduction system spans more than 3,000 km along the northern boundary of the Pacific Ocean and is the location of both devastating earthquakes and frequent volcanic eruptions. The potential for loss of life and destruction compels us to study the nature of the Alaska-Aleutian subduction system. However, numerous studies have raised more questions than they have answered, illuminating the complex nature of this arc such as changes in arc water content along arc, trench parallel shear wave splitting directions, and locked versus slipping regions of the subducting and overriding plate. A necessary component to understanding the complexities of this arc is 3D subduction zone models. I have verified that the 3D thermal and velocity models using the Sepran finite element package correspond to previously published 2D. However, 3D model resolution no greater than 2 km in the mantle wedge region where temperature and velocity change most rapidly is necessary. The desired mesh resolution requires that the mesh spanning the Alaska Peninsula to the western Aleutians must comprise more than 23 million elements. The Sepran package version 0310 is limited to 4 Gb of memory per core or roughly 2 million elements and does not support parallel programming. Thus in order to run the full 23 million element Alaska-Aleutian model, the newest version of Sepran 0315 which does support parallel programming must be utilized. Finally, solving for velocity in the subducting slab of a large, variable slab shape often results in violations of conservation of mass as required for the Boussinesq approximation. A combination of defining velocity parallel to the incoming plate velocity to a depth of 170 km in the slab followed by a method that defines velocity according to the elements dip is the best approach to minimizing deformation in the subducting slab.

1. Introduction

The most destructive earthquakes in the world occur at subduction zones, a tectonic setting in which a dense oceanic plate subducts, or dives, under a continental or another oceanic plate (Figure 1). The 1960 Valdivia earthquake in Chile, generated from the Nazca Plate subducting under South America, had a moment magnitude (M_w) of 9.5, designating it the largest earthquake ever recorded. The earthquake resulted in over 1,500 deaths, left 2,000,000 people homeless, and caused \$550 million dollars in damage in southern Chile (Talley and Cloud, 1962). It also generated a tsunami that traveled across the Pacific Ocean, causing damage and casualties as far away as Japan (Figure 2; National Geophysical Data Center, 2015).

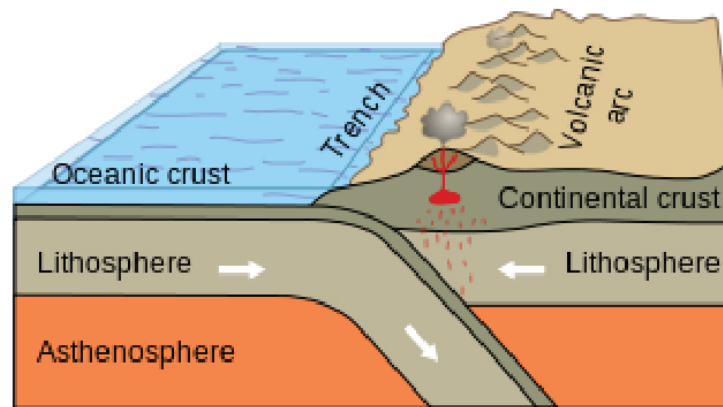


Figure 1: Illustration of a subduction zone from USGS. The dense oceanic crust and lithosphere subducts under the continental lithosphere generating melt in the mantle wedge and a volcanic arc at the surface.

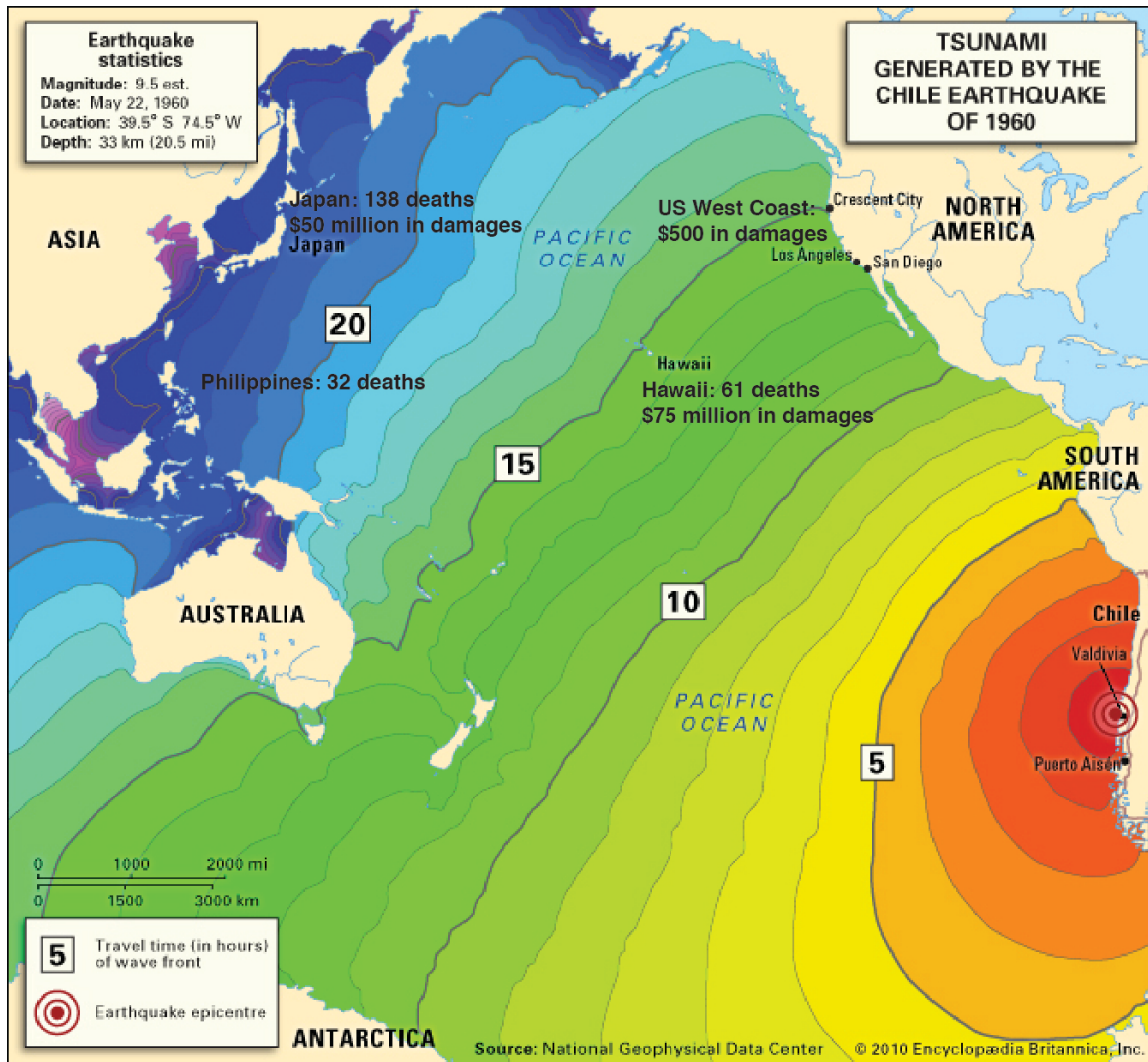


Figure 2: Image of tsunami travel time in hours. Data for number of deaths and cost of damage from the National Geophysical Data Center.

Only 4 years later in 1964, the second largest earthquake ever recorded, Mw 9.2, occurred near Prince William Sound in Alaska. The earthquake resulted in measurable surface offsets and deformation over an area larger than 177,000 km² (Plafker, 1969). The coast of the Gulf of Alaska experienced uplift on average of 1.8 m, exposing large areas of the seafloor (Figure 3 and 4). Along with the uplift, an area of 64,000 km² in and around Prince William Sound systematically shifted more than 19 m in the seaward direction (Plafker, 1969).



Figure 3: Photo showing the amount of tectonic uplift on Glacier Island. Before the earthquake, the top of the brown section marks the upper limit of the intertidal zone algae growth. The algae that were living at the top of the pre-earthquake intertidal area are now brown and desiccated. The new location of the high tide after the earthquake is marked by the top of the yellow-green section, where algae is able to survive. The approximate height change between the top of the brown section and the top of the yellow section is 1 m. Photo by J.K. McGregor and C. Abston, USGS.



Figure 4: Photo showing the uplift of a dock on Hinchinbrook Island near Prince William Sound. The dock and surrounding land was uplifted by nearly 2.5 m during the earthquake. Photo by J.K. McGregor and C. Abston, USGS.

Chile and Alaska are just two examples of subduction zones, most of which are aligned in a ring around the entire Pacific Ocean and result in heightened seismic and volcanic activity (Figure 5). Clearly subduction zones are extremely active tectonic regions that impact our societies. This alone should compel us to study subduction zones and drive us to understand the dynamics that are operating in these systems.

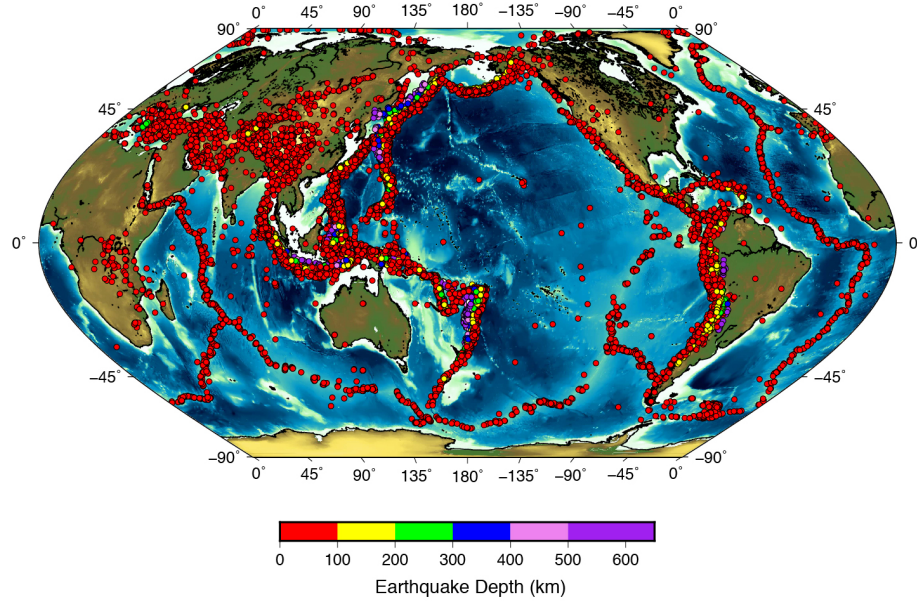


Figure 5: Global earthquakes outline the Pacific Ocean which is ringed by subduction of the Pacific plate. Earthquake data from (International Seismological Center, 2009)

The generation of large earthquakes is not the only reason subduction zones are an interesting tectonic setting. Subduction zones are also the location of the deepest earthquakes in the world, with earthquakes as deep as ~ 700 km recorded (Figure 6). At all other tectonic settings earthquakes occur in the crust, generally shallower than 50 km depth. Occurrence of these deep earthquakes is not rare. Of the nearly 10,000 earthquakes that happened globally from July to August 7, 2015, nearly 900 of them were between 70 and over 600 km depth, constituting around 10% of all earthquakes in just one month (USGS earthquake catalog).

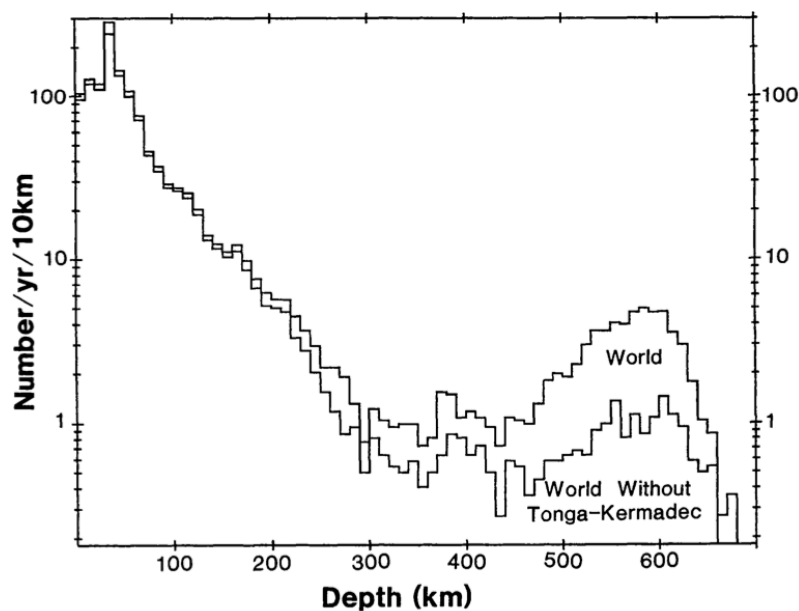


Figure 6: Plot of number of earthquakes per year in 10 km depth intervals. The earthquakes were reported by ISC and occurred between January 1964 and February 1986. The upper line shows global earthquakes while the lower line excludes Tonga-Kermadec. Figure from Frohlich (1989).

In general intermediate and deep earthquakes are smaller in magnitude than shallow earthquakes. However, some deep earthquakes have been very large. The largest deep earthquake ever recorded occurred in May of 2013 in the Pacific Plate as it subducts under the Sea of Okhotsk near the northeast corner of Russia. The earthquake was over 600 km depth and had a M_w of 8.3. It was felt all across Asia, in Moscow, and on the West Coast of the United States (USGS, 2013). In May of 2015 an earthquake at 660 km depth occurred in Japan. The moment tensor of the deep Japan earthquake indicates it was an oblique-normal fault (Figure 7). At the surface, a normal fault indicates extension, but at ~ 660 km depth the confining pressure is nearly 24 GPa (240,000 times the pressure of the atmosphere), and the focal mechanism rather indicates the principal direction of the stress change. These extremely large and deep earthquakes remain enigmatic to geophysicists today.

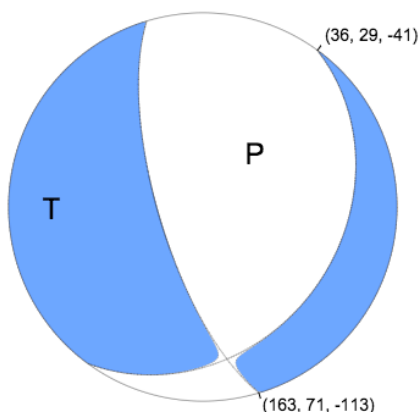


Figure 7: moment tensor solution from USGS of the M_w 7.8 earthquake that occurred May, 2015 in Japan. The earthquake occurred at 660 km depth.

Deep earthquakes were first discovered in the 1920's by Kiyoo Wadati in Japan. We now refer to the plane of deep seismicity extending well into the mantle as the Wadati-Benioff zone, named after those who first observed this feature. We still use the nomenclature proposed by Wadati that intermediate earthquakes are between 70 and 300 km deep and deep earthquakes exceed 300 km (Figure 8). The Wadati-Benioff zone outlines the top of the subducting plate, indicating that the intermediate seismicity is associated with the cold, negatively buoyant subducting plate.

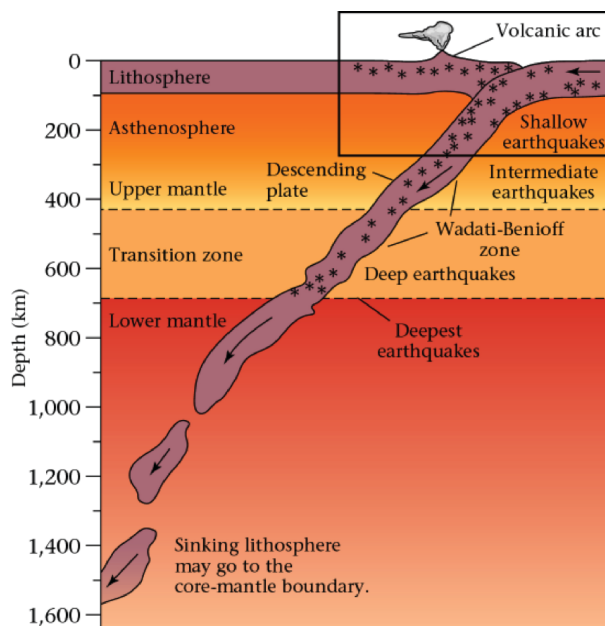


Figure 8: Illustration from (Marshak and Repcheck, 2004) of subducting slab sinking into the mantle with the Wadati-Benioff zone labeled as intermediate and deep earthquakes occurring in the slab

While deep seismicity was first observed in the early part of the 20th century, it was not until the mid-1960's that laboratory studies began to shed light onto why earthquakes might happen so far beneath the brittle-ductile transition of the crust. The work of Raleigh and Paterson (1965) proposed that dehydration of minerals such as serpentine, amphiboles, or micas could reduce the effective confining pressure to values that allowed for brittle fracturing to occur. The role of water during melting and crystal fractionation in subduction zones became apparent in the 1970's with the experimental work of Ringwood (1974). He used finite element modeling to show that densification to eclogite in the subducting slab produced extensional stresses generating earthquakes within the slab to great depths. In the 1990's, Kirby et al. (1996) used finite element modeling to show that densification to eclogite in the subducting slab produced extensional stresses generating earthquakes within the slab to great depths. Furthermore Kirby et al. (1996) explained that the transformation to eclogite in older, colder subduction zones was delayed, accounting for the observation that old, cold subduction zones produced the deepest earthquakes while young, warm subduction zones experienced only shallow earthquakes. It is now well established that rocks undergo weakening and embrittlement during dehydration, resulting in fracturing (e.g., Kirby and Kronenberg, 1987; Hacker et al., 1990; Dobson et al., 2002; Yamasaki, 2003; Nakajima et al., 2013). Hence, dehydration of the subducting slab, intermediate depth seismicity and generation of arc melt are all linked together in the subduction zone system (e.g., Ishikawa and Nakamura, 1994; Ferris et al., 2003; Abers, 2005; Abers et al., 2006; Barcheck et al., 2012).

The next questions addressed by the scientific community were, for example, the exact dehydration reactions and depths of those reactions in the slab and the amount of

water involved in the subduction process. Schmidt and Poli (1998) were some of the first experimentalists to determine the phase relationships of water saturated basalts. The authors pinpoint the location in the subducting crust in which blueschists, a hydrated metamorphic phase that can have up to 6 weight percent (wt%) H₂O, transitions to dry eclogite as around 600°C and 15-22 kbar. Water is most likely released continuously as blueschist undergoes metamorphic facies reactions down to 700°C and 30 kbar, below which dry eclogite persists. Since the Schmidt and Poli (1998) work, other experimental metamorphic facies work has been conducted in detail (e.g., Iwamori, 2004; Grove et al., 2006).

The depth at which metamorphic facies changes and dehydration occurs depends on the age of the subducting oceanic crust and subduction rate. Old, cold subducting slabs such as northern Japan can retain bound H₂O to depths greater than 250 km when 2 wt% H₂O is assumed present in the upper 2 km of the subducting slab. Warm, young subducting slabs such as Cascadia completely dehydrate by around 100 km depth under the same assumptions (van Keken et al., 2011). As the Jurassic aged Pacific Plate subducts under northern Japan, it heats up very slowly so that temperature conditions allowing for the blueschist to eclogite transition occur at much deeper depths than for the very young Juan de Fuca plate subducting under Cascadia. van Keken et al. (Figure 9; 2011) find that the location of the dehydration reactions in Japan correspond to the location of intermediate and deep seismicity in Japan (Kita et al., 2006). Furthermore, the age and rate of subduction determine the dehydration pathway for the slab because dehydration of mafic rocks has a positive Claperyon slope while dehydration for the upper mantle has a negative Claperyon slope below 200 km depth. Hence in hot subduction zones, the upper mantle completely dehydrates, as it easily crosses the negatively sloping transition from chlorite to garnet. The subducting slab must remain very cold for the upper mantle to carry any H₂O to greater depths. In contrast, cold and intermediate subduction zones can carry H₂O to great depths in the gabbro section despite having less H₂O bound in this section and despite being at a relatively similar temperature as the mantle below because the Claperyon slope is positive. In summary, intermediate depth seismicity, metamorphic facies changes, and dehydration reactions are all intimately linked within a subducting slab, and the depth at which we see these phenomenon depends on physical parameters of the subduction zone itself, such as age of the subducting slab and rate of subduction.

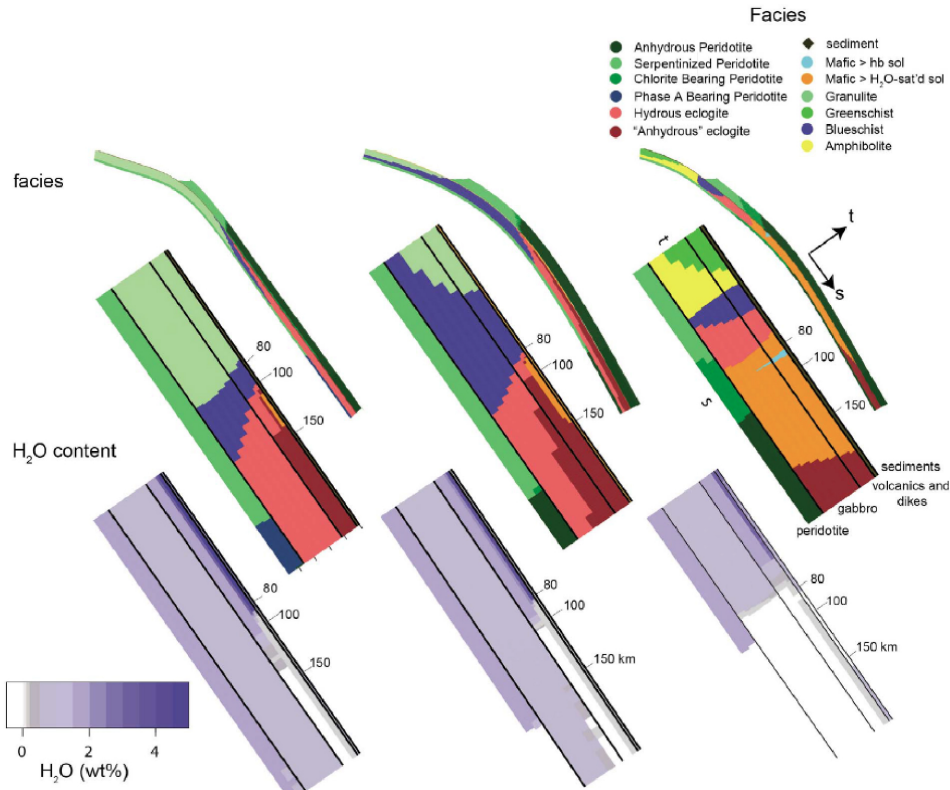


Figure 9: Figure from van Keken et al. (2011) showing metamorphic facies (top) and H₂O content (bottom) for three different subduction systems northern Japan (left) Nicaragua (middle) and Cascadia (right).

The link of intermediate depth seismicity and dehydration reactions can be further explored with thermal and petrological models of subduction zones. Previous subduction zone modeling has focused on 2D slices of subduction systems (e.g., Peacock, 1999; van Keken et al., 2002; van Keken et al., 2008; Wada and Wang, 2009; Hasegawa et al., 2009; Syracuse et al., 2010; van Keken et al., 2011). However, it has been demonstrated that for complex subduction zones, for example curved slabs or oblique subduction, 2D cross-sections are not sufficient to describe the thermal and velocity structure within the slab and mantle wedge (Bengtson and van Keken, 2012). Others have described the need for 3D models to explain along arc variations in subduction zones (Hasegawa et al., 2009). In order to get a full and realistic picture of the 3D thermal structure of a subduction zone, we must build 3D models.

In this thesis I focus on the 3D thermal and velocity models of the Alaska-Aleutian arc from the Alaska Peninsula to the western Aleutians. The Alaska-Aleutian arc is of interest because as illustrated above, it is a highly seismically active subduction zone that has had major, damaging earthquakes in the past as well as volcanic eruptions. Also this region is the target site of the GeoPrisms community, which includes geochemical, petrological, and seismological work.

The Alaska-Aleutian subduction system is created as the Pacific plate subducts beneath the North American Plate at a rate of 57 to nearly 77 mm/yr (Figure 1). The angle

of subduction changes greatly along arc from trench perpendicular in the east to nearly strike-slip in the west. The more studies conducted on the Alaska-Aleutian Arc, the more complex the picture becomes. For example, Zimmer et al. (2010) showed that water content in melt inclusions spans the range of global values, 2 to 7 wt%, from arc magma, but it is not understood why the water content varies along arc non-systematically. Seismic shear wave splitting studies have found trench parallel fast axes along the arc, contrary to the the trench normal splitting directions predicted by 2D cornerflow models (Yang et al., 1995; Christensen and Abers, 2010). Many hypotheses have been proposed to explain unexpected splitting axes in subduction zones (e.g., Kneller et al., 2005; Kneller et al., 2007; Kneller and van Keken, 2008; Kneller et al., 2008), however, an explanation for the splitting directions in Alaska has not been determined. We also see changes in the depth of seismicity along the Alaska-Aleutian arc. In Alaska, seismicity rarely exceeds 100 km in Alaska. In the central Aleutians seismicity can extend 300 km depth. Seismicity is extremely shallow in the far western Aleutians, with all seismicity above 50 km depth. A large scale 3D thermal and velocity model of the entire Alaska-Aleutian Arc would provide insight into understanding trench parallel fast axes, changes in water content at the arc and depths of seismicity. With the full 3D model we can get a comprehensive picture of the temperature structure in the subducting slab, allowing us to pinpoint the locations of metamorphic facies changes and dehydration reactions at depth which have been linked to intermediate depth seismicity.

Previous modeling work of the Alaska-Aleutian Arc has been 2D and only considered the subduction of the Yakutat block in eastern Alaska (Abers et al., 2006). The finite element program, Sepran, is written in Fortran77, which has a structural limit of 4 Gbyte per core. I have found that 4 Gbytes is capable of running a model with 2 million elements. I have built a 3D finite element model of the entire Alaska-Aleutian subduction system, composed of more than 23 million elements. The present version of Sepran is thus unable to compute this 3D model. As a result, a simulation of the flow in my higher fidelity 3D mode will have to wait for the next generation Sepran, or be ported to another fluid dynamics package. This thesis focuses on background information about the Alaska-Aleutian Arc, putting the 3D Alaska-Aleutian model into a geologic context. I also focus on resolution testing of 3D models of 2 million elements to determine the mesh resolution required to generate accurate results. Finally, I examine how velocity should be prescribed on a 3D slab that has a variable shape. In the models I do present, the mantle wedge rheology is estimated as dry, olivine dislocation creep based on the empirical results of Karato and Wu (1993).

I have found that for a 3D model, resolution can be no greater than 2 km in regions of high velocity such as where the overriding plate, subducting slab, and wedge meeting. Also, the area of incoming mantle must be resolved to no greater than 7 km. The models use the Boussinesq approximation to solve for velocity in the slab, and as a result the conservation of mass must be maintained. I have determined that a combination of defining velocity vectors parallel to the incoming plate velocity and parallel to the dip of the element is the best means of minimizing deformation in the subducting slab.

2. Previous Studies

2a. Tectonic history of Alaska

The Alaska-Aleutian subduction zone borders the northern extent of the Pacific Ocean, extending nearly 3,000 km from southern Alaska to Kamchatka. The Aleutian Ridge, which includes the Aleutian Islands, extends westward of the Alaska Peninsula. It has some of the most dramatic relief of the world, spanning 9,300 m in elevation from the Aleutian Trench to the summit of Vsevidof volcano on the island of Umnak (Scholl et al., 1987). The ridge acts as a divider between the Pacific Ocean and the Bering Sea to the north. In the east, the Pacific Plate subducts nearly orthogonal to southern Alaska at a rate of 55 mm/yr (DeMets et al., 1994). An anomalously thick block called the Yakutat terrane subducts under eastern Alaska. The block terminates against the Queen Charlotte-Fairweather transform fault system, which is a dextral fault accommodating 49 mm/yr of motion (Plafker and Berg, 1994; Ferris et al., 2003). Towards the west, subduction becomes more oblique, ending with nearly strike-slip motion near Kamchatka. The subduction rates also increase toward the west, reaching 77 mm/yr in the far western Aleutians (DeMets et al., 1994). The subducting Pacific plate is oldest in the central Aleutians where it is 68.7 million years (Myr) old. To the east and west of the central Aleutians, the Pacific plate is younger between 40 and 50 Myr old (Lonsdale, 1988). The age of the subducting plate is offset at times by several fracture zones, the two most prominent being the Amlia fracture zone location at 170 °W and the Rat fracture zone location at 178 °E (Figure 10; Lonsdale, 1988).

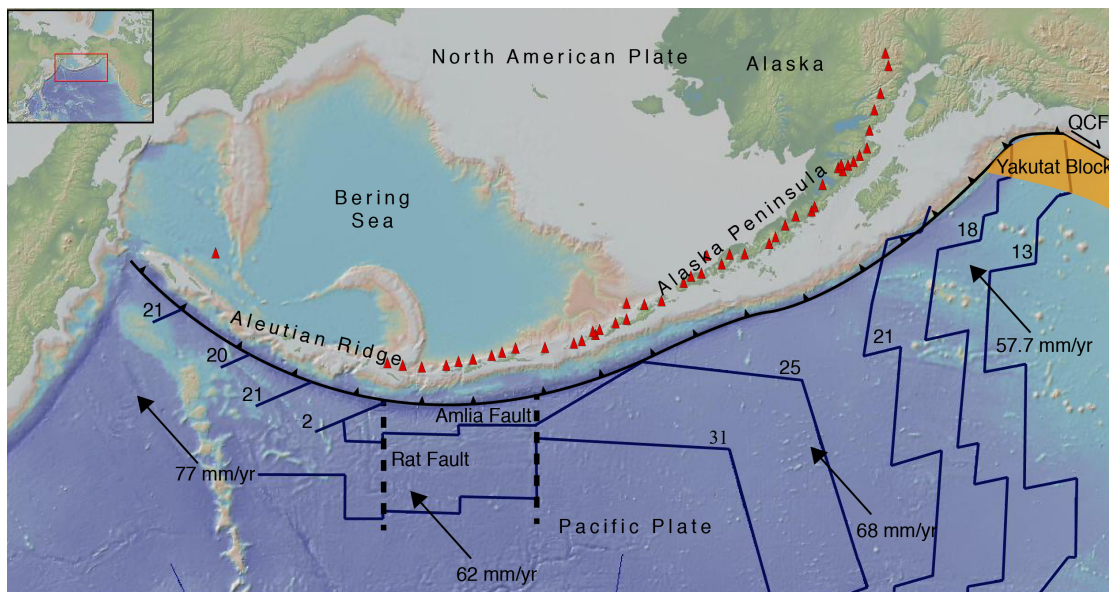


Figure 10: GeoMapApp image of the Alaska-Aleutian subduction system. The magnetic anomaly identifiers are labeled in blue: anomaly 13 corresponds to 33 million years ago (Ma), 18 to 40.2 Ma, 20 to 43.8 Ma, 21 to 47.9 Ma, 23 to 52 Ma, 25 to 56 Ma, and 31 to 68.7 Ma. The Amlia fault occurs at the 173 °W parallel and offsets the magnetic anomaly 25

(Scholl et al., 1982). The Rat Fault occurs at the 178 °E parallel and also offsets the magnetic anomaly 25 (Lonsdale, 1988). The magnetic isochron identifiers are from Müller (1997) and Lonsdale (1988). QCF is the Queen Charlotte Fault. Volcanoes labeled by red triangles.

Alaska and the northern Pacific ocean has been an active subduction zone for at least 100 Myr, starting with the subduction of the Farallon Plate from 100 to 85 million years ago (Ma) (Hillhouse, 1987). The Farallon plate split during late Cretaceous rifting, forming the Kula plate. The Kula plate subducted in the northern Pacific from 85 to 55 Ma (Rea and Dixon, 1983; Hillhouse, 1987). There are still remnants of the Kula plate under the Bering Sea (Figure 11). Today, the Pacific plate subducts under Alaska and the Aleutian Islands (Hillhouse, 1987). The Alaska-Aleutian Arc can be roughly subdivided into two sections: The Alaska and Alaska Peninsula section, and the Aleutian ridge and Aleutian Islands section. Prior to 43 Ma, the two sections evolved separately (Vallier et al., 1994). The entire subduction zone, Alaska, the Alaska Peninsula, the Aleutian ridge, and the Aleutian Islands, began evolving together in the Late Eocene, when the Pacific Plate changed directions (Clague, 1981).

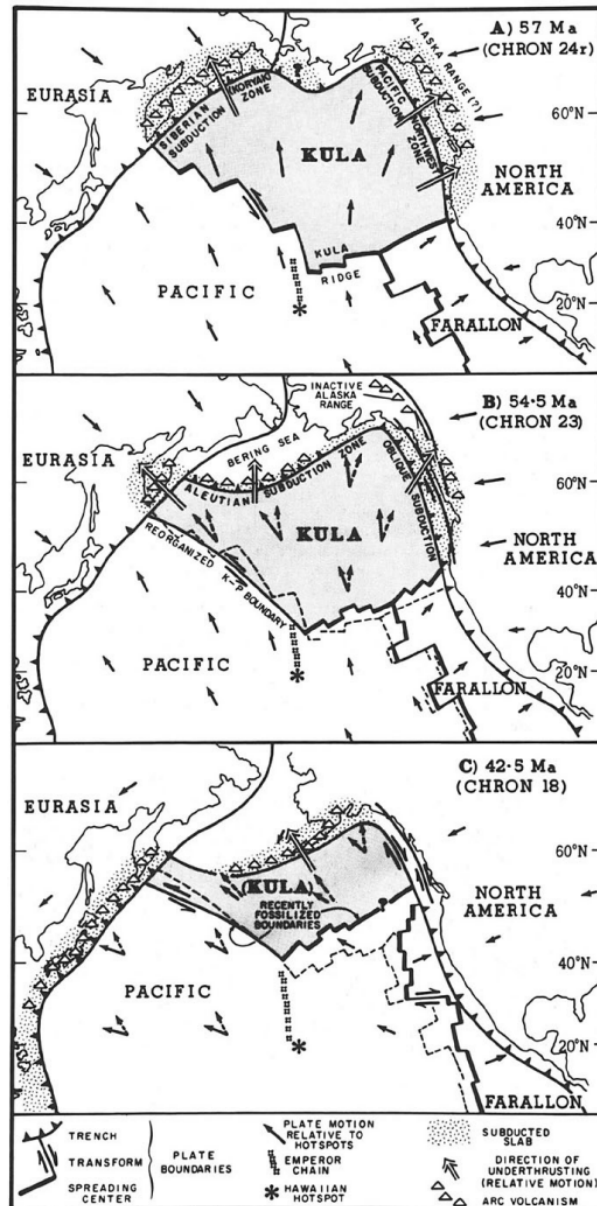


Figure 11: Reconstruction of the Kula plate. Panel A illustrates the Kula plate before the Eocene, panel B after the early Eocene, and panel C after the middle Eocene. Dashed lines and arrows show plate boundaries and plate motions respectively. Panel A shows the northern boundary of the Kula plate subducting north of the present day position of the Aleutian ridge. Panel B illustrates that the subduction zone jumped southward, and the Aleutian Arc began to form. Part of the Kula plate is then trapped north of the Aleutian Ridge, forming the basement of the Bering Sea. Also shown in panel B, the Kula plate rotation, which may have contributed to the jump in subduction to the Aleutian Ridge (Scholl et al., 1987). Panel C illustrates that the Kula plate has decreased in size as it subducts beneath North America, and that the Kula spreading ridge is now dead (dashed lines south of Kula plate). Figure from Lonsdale (1988).

In the east, southern Alaska and the Alaska Peninsula are built from a series of terranes that accreted to central Alaska (Figure 12). The Wrangellia and the Peninsular terranes are two large terranes that collided with southern Alaska between 100 and 55 Ma (Hillhouse, 1987; McClelland et al., 1992). Later, one of the more recent collisions with Alaska, the Chugach terrane accreted 55 Ma (Hillhouse, 1987). These terranes originated near 30° south of Alaska and moved poleward with the Kula oceanic plate (Haeussler et al., 1992; Hillhouse and Coe, 1994). After the Wrangellia and Peninsular terranes accreted, and also possibly after the Chugach terrane accreted, southwestern Alaska underwent counterclockwise rotation of as much as 50°, shaping the position of Alaska and the Aleutian Arc into something we would recognize today (Hillhouse, 1987; Plafker and Berg, 1994). After the rotation from the mid Cretaceous to the early Paleogene, an Andean style arc system developed along southern Alaska due to convergence of the Kula plate. At 43 Ma, the same time as the bend in the Emperor Seamount Chain, volcanism increased along the Alaska Peninsula (Plafker and Berg, 1994). The vast majority of volcanic rocks of Alaska and the Alaska Peninsula provide K-Ar ages from 42 to 30 Ma, except in the southwestern end of the Peninsula where ages are older at 54 to 52 Ma (Vallier et al., 1994) In Late Miocene times around 15 Ma, a second episode of magmatism occurred. Since 15 Ma, the active arc front has migrated northwest and undergone rapid uplift and erosion, exposing large plutons (Vallier et al., 1994). Fournelle et al. (1994) found that 10.5 Ma, Alaska and its Peninsula underwent a frequent series of eruptions occurring every 125 to 500 years. Between 10.5 and 7.5 Ma, the number of eruptions decreased to one only every 9,000 years. Volcanic activity increased again 5 Ma with events every 1,700 to 2,400 years. Since the 1700's when modern recording of volcanic eruptions began, the most active portion of the arc has been the Alaska Peninsula including volcanoes such as Pavlof, Shishaldin, Akutan. More than 40 eruptions have been recorded at Pavlof since 1700. The volcanic activity decreases east and west of the Alaska Peninsula, with most volcanoes having less than 10 eruptions since the 1700's (Fournelle and Marsh, 1994).

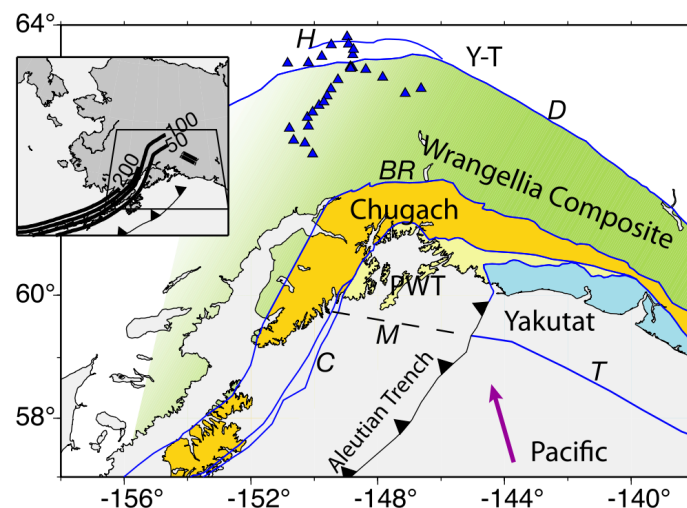


Figure 12: Map of extent of southern terranes including the Chugach terrane and the Wrangellia terrane. PWT is the Prince William terrane. BR is the Border Ranges. Figure from Rossi et al. (2006).

The Aleutian ridge encompasses the Aleutian Islands and the undersea ridge that extends from the Alaska Peninsula to Kamchatka, roughly 2,000 km in distance. The Aleutian ridge began growing 55 to 50 Ma, when the spreading direction of the Kula plate was changed due to a rotation (Scholl et al., 1987; Lonsdale, 1988). At this same time, parts of the Kula plate became trapped north of the now growing Aleutian Arc and became the basement of the Bering Sea (Scholl et al., 1987). 43 Ma, the spreading at the Kula-Pacific spreading center stops, and the Pacific plate becomes welded to the Kula plate (Engebretson et al., 1985; Lonsdale, 1988). The Aleutian arc had grown significantly by that time since its birth 55 Ma. Around 37 Ma, volcanism began to decrease and growth of the ridge slowed. Between 20 to 10 Ma, volcanism waxed every 5 Myr. The dead Kula ridge enters the Aleutian trench 10 Ma (Scholl et al., 1987). At this time, Aleutian volcanism waxed every 2.5 Myr (Hein et al., 1978). Volcanism slowed greatly 5 Ma, and the arc began to subside (Scholl et al., 1987). Today, portions of the arc emerge out of the Pacific Ocean as the Aleutian Islands, but a larger portion of the Aleutian Ridge is submerged (Figure 13).

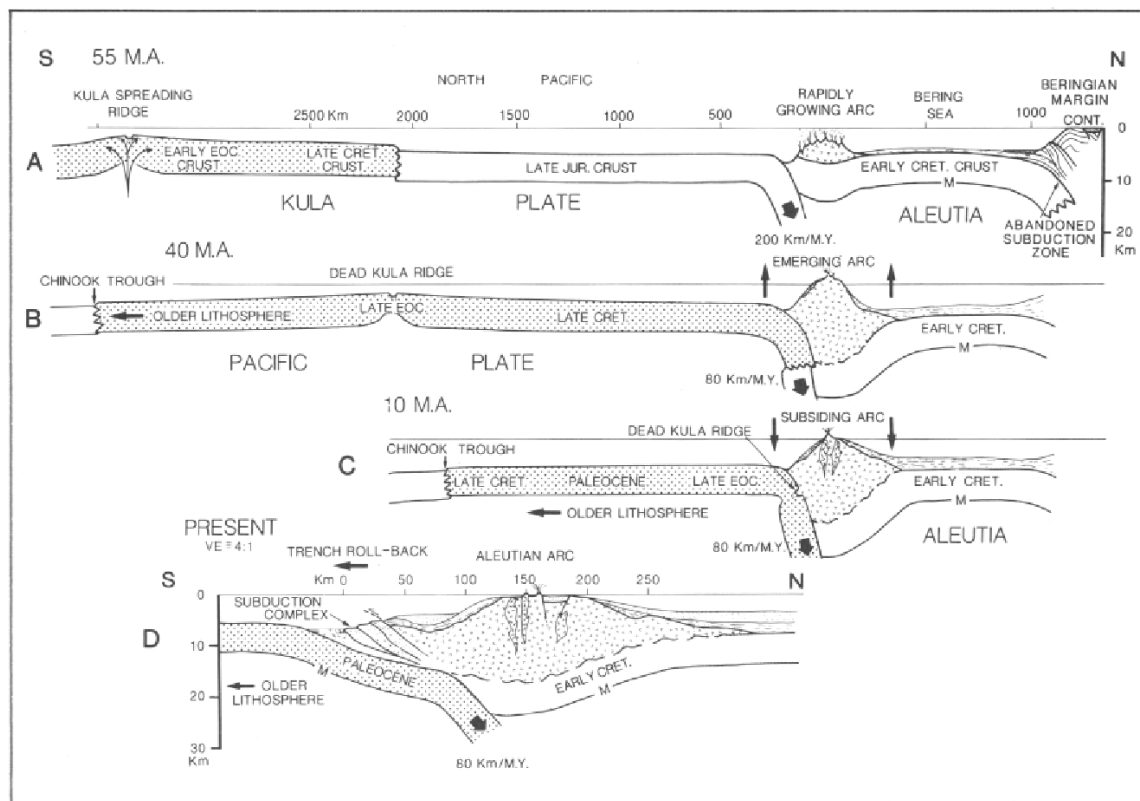


Figure 13: Schematic illustration of the evolution of the Aleutian Ridge from Scholl et al. (1987). 55 Ma the Aleutian ridge began growing when subduction of the Kula plate transferred to the south. The Kula spreading ridge was still active 55 Ma. By 40 Ma spreading at the Kula ridge had stopped, and the Pacific plate and Kula plate became welded together. The dead Kula ridge subducts under the subsiding Aleutian arc 10 Ma

2b. Seismicity, anisotropy, and great earthquakes in the Alaska-Aleutian subduction system

Alaska and the Aleutian Islands are some of the most seismically active regions in the world, with on average 4,000 earthquakes occurring each year in Alaska alone (Stover and Coffman, 1991). The first earthquake in modern records occurred on the Sanak and Shumagin Islands south of the Alaska Peninsula in July 1788. Since the late 19th and early 20th century, several extremely large earthquakes have been recorded. The largest of these earthquakes occurred in 1964 and had a rupture area of over 520,000 km² (Stover and Coffman, 1991).

The majority of earthquakes in Alaska and the Aleutian Islands are thrusting events occurring between 0 and 50 km depth (Figure 14 and 16) as a result of the Pacific Plate subducting beneath North America. These shallow, thrusting events are generally the most devastating earthquakes, causing massive damage to infrastructure and are capable of generating tsunamis. Normal faulting in the outer-rise produces shallow earthquakes as well. The Central Aleutians experience the deepest earthquakes in this system, extending to 300 km depth (Figure 14). In general, the western Aleutians only experience earthquakes above 50 km depth, most likely as a result of the oblique subduction of the Pacific Plate.

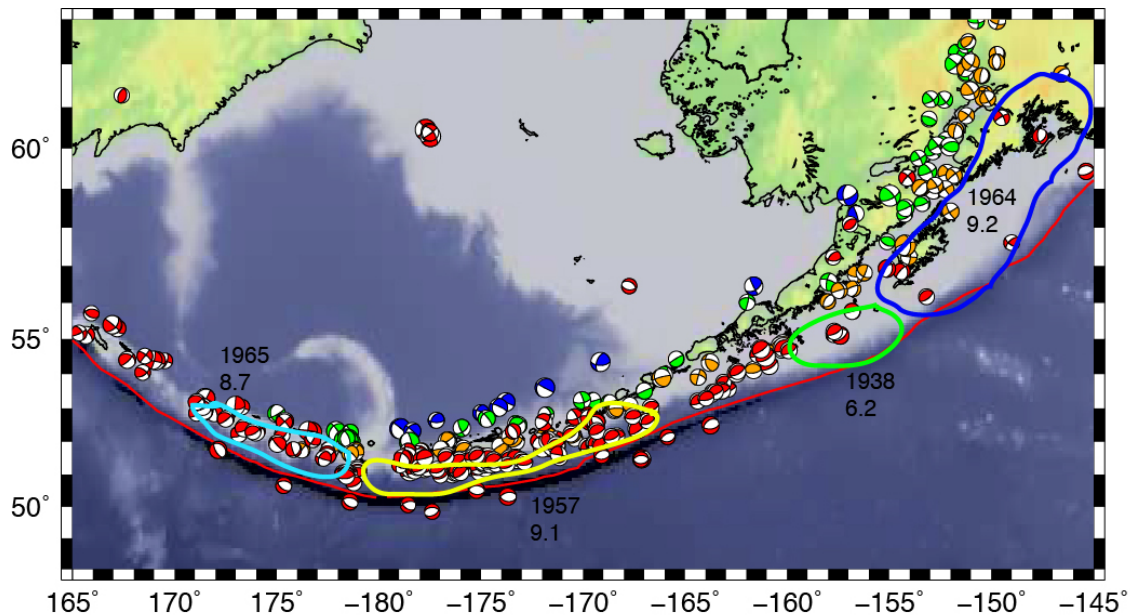


Figure 14: Moment tensor solutions for earthquakes along the Alaska-Aleutian Arc; red are earthquakes between 0 to 50 km depth, orange, 50 to 100 km depth, green, 100 to 200 km depth, and blue, 200 to 300 km depth. Colored circles show rupture areas of different earthquake events, with year and magnitude. Moment tensor data from the global Centroid Moment Tensor catalog (Ekström and Nettles, 2013). Rupture areas from (Freymler et al., 2008).

Alaska and the Aleutian Islands have always proved a difficult region to study due to their remoteness and short field season. Interest in the geologic understanding of this region began after WWII, with the USGS Alaska Volcano Project that ran from the 1940's through the 1960's and focused on understanding the Aleutian Islands (Vallier et al., 1994). The first comprehensive geological summary of the stratigraphy and structure of the Alaska Peninsula was published in 1965 by Burk (Burk, 1965). In the 1970's and 1980's, the Deep Sea Drilling Project conducted a series of multichannel seismic reflection, seismic refraction, and gravity studies, as well as collection of magnetic data, and rock samples, with heavy focus on the Aleutian Islands and Aleutian Ridge. A plethora of research and publications came out of the Deep Sea Drilling Project, including the work of Scholl et al. (1987) and Lonsdale (1988). Also in the 1970's and 1980's, with the theory of plate tectonics well established, seismic studies attempting to identify the Wadati-Benioff zone on the Pacific plate were conducted. Some of the first studies to locate the Wadati-Benioff zone in Alaska were published by van Wormer et al. (1974) and Stephens et al. (1984). Ratchkovski et al. (1997) first identified a double seismic zone beneath Cook Inlet, Alaska. Following the discovery of a double seismic zone in Alaska, seismic studies focused on earthquake relocations and better descriptions of the Wadati-Benioff zone (Ratchkovsky and Hansen, 2002). From 1991 to 2001 the Broadband Experiment Across the Alaska Range (BEAAR) was deployed to collect information on the crust, mantle, and subducting slab beneath Alaska. From BEAAR, the existence of an anomalously cold area in the mantle wedge above 80 km depth, dubbed the cold nose, was confirmed (Figure 15; Abers, 2005). Abers (2005) was also able to establish that earthquakes occurred within the subducting crust in a plane dipping only 2° more steeply than the crust, and that the top of the subducting slab remains seismically slow to depths of 150 km. The author interpreted the disappearance of slow seismicity to eclogization, a mineral assemblage with seismic velocities similar to the surrounding mantle, of the subducting slab. 2D thermal models of eastern Alaska confirmed that seismicity in the slab lies along a narrow pressure and temperature band and is most likely a result of a single or a series of dehydration reactions in eastern Alaska (Abers et al., 2006).

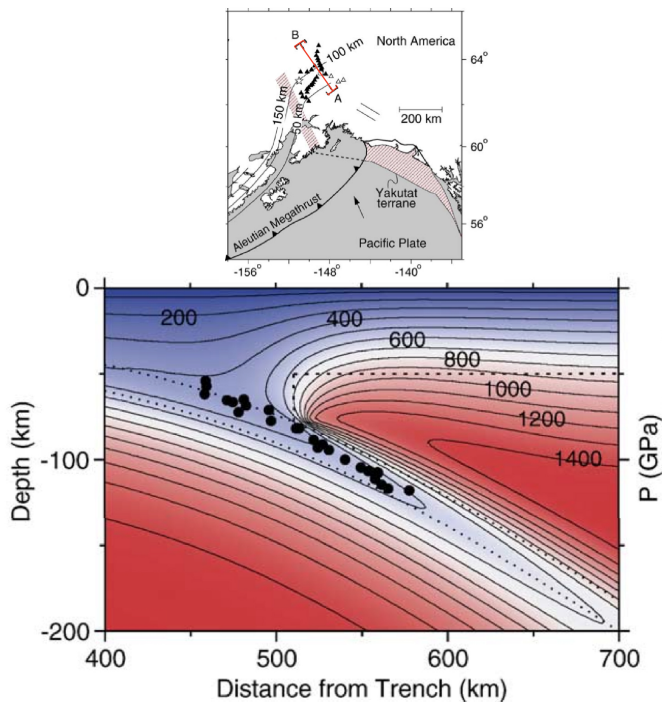


Figure 15: Top: Map of eastern Alaska with cross-section labeled in red from A-B. Bottom: Non-Newtonian 2D model results of cross-section A-B (Abers et al., 2006) Earthquakes are labeled as filled in black circles.

An entire picture of Alaska and the Aleutian arc was put together in 2006 by Syracuse and Abers (2006) with the use of local and teleseismic earthquake catalogs (Figure 16). Other studies that attempted to gain a holistic picture of the Alaska-Aleutian subduction system utilized 3D tomographic images of the downgoing lithosphere and mantle wedge. The tomography studies identified a seismically fast, 3-6% faster than the surrounding mantle, slab subducting to depths of 200 km at least and a seismically slow mantle above the slab (Kissling and Lahr, 1991; Zhao et al., 1995). These studies confirmed that intermediate depth seismicity was occurring in the seismically fast downgoing slab.

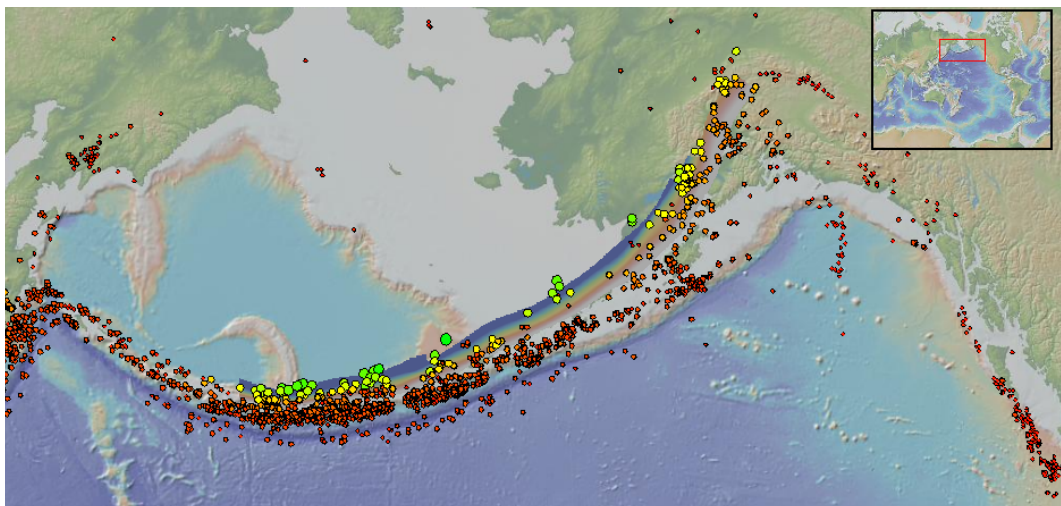


Figure 16: GeoMapApp showing slab contours to 250 km depth dark blue (Syracuse and Abers, 2006). Earthquakes from the EHB catalog are also plotted. Red, orange 0 to 50 km depth, yellow 50 to 100 km depth, green 100 to 250 km depth.

Seismic studies have also been used to map seismic anisotropy along the Alaska-Aleutian Arc. One of the first studies to examine anisotropy in Alaska measured shear wave fast axis near Shumagin Island, 159 °W to 163 °W (Yang et al., 1995). The authors found the fast axis was aligned parallel to the volcanic front or parallel to the trench strike. Numerous studies since the 1990's have demonstrated trench parallel fast axes in subduction zones (Yang et al., 1995; Fischer et al., 1998; Hiramatsu et al., 1998; Polet et al., 2000; Smith et al., 2001; Wiens and Smith, 2003; Nakajima and Hasegawa, 2004; Long and Silver, 2008). Trench parallel fast axes are counter to the standard 2D cornerflow model, which would predict trench perpendicular flow and therefore trench parallel fast splitting axes (Peacock, 1999; van Keken, 2003; Syracuse et al., 2010). However, studies of the shear wave fast axes directions in Alaska and the Aleutians demonstrate that anisotropy is more complex than the 2D cornerflow model predicts. Christensen and Abers (2010) utilized seismic data from BEAAR to estimate the shear wave splitting direction in central Alaska (Figure 17). They found that where the slab is 70 km deep or more, the fast axis is parallel to the trench strike, and the shear wave splitting is most likely originating from either the slab or mantle wedge above the slab. Closer to the Alaska trench, Christensen and Abers (2010) found splitting directions parallel to slab motion, a 90° switch from their deeper measurements. Here the authors suggested that the splitting could be coming from the slab or the mantle above or below the subducting lithosphere. Hanna and Long (2012) found a similar 90° switch from trench parallel near the 70 km deep contour of the subducting slab to trench normal shear wave fast directions near the trench.

Many hypotheses have been proposed to explain the complex shear wave splitting results measured in Alaska and other subduction zones. One idea is torodial flow around the slab or trench parallel flow for curved or oblique subduction (Kincaid and Griffiths, 2003; Kneller et al., 2007; Kneller and van Keken, 2008; Kneller et al., 2008; Bengtson and van Keken, 2012; Billen and Jadamec, 2012; Strak and Schellart, 2014). Another idea is that flow is still dominated by the standard cornerflow trench perpendicular motion, but that B-type olivine, an olivine fabric type which would exhibit trench parallel fast directions with flow moving trench perpendicular, develops in the slab or mantle wedge (Kneller et al., 2005; Kneller et al., 2007). A full 3D velocity model of the entire Alaska-Aleutian Arc may shed light onto the cause for trench parallel fast axes and changes in the splitting direction.

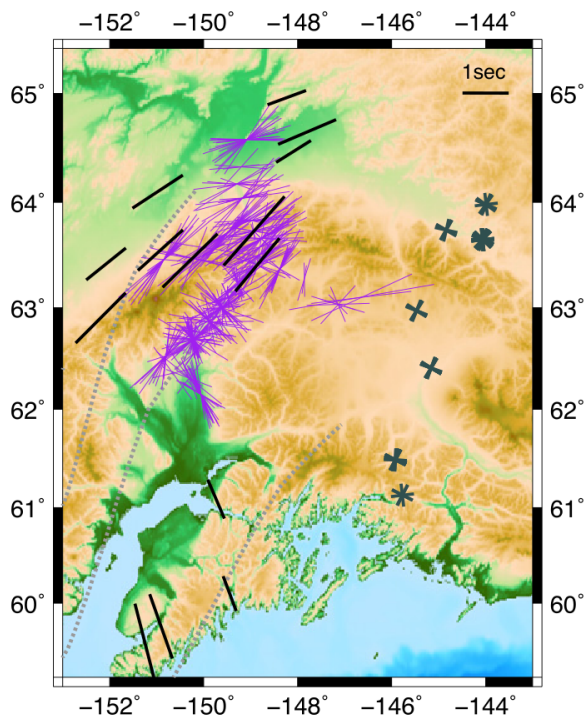


Figure 17: Comparison between results of Hanna et al. (2012) as black bars and gray crosses and Christensen and Abers (2010) as purple bars. Figure from Hanna et al. (2012).

While it is clear that the entire Alaska-Aleutian arc is seismically active, very large seismic events tend to occur repeatedly in similar locations (Ryan and Scholl, 1993; Freymuller et al., 2008). Ryan and Scholl (1993) were the first to report this pattern from the occurrence of the 1957 earthquake near Andreanof Island followed by another large earthquake near the same location in 1986 (Figure 18). The authors attribute this pattern to a forearc structural fabric and argued that the segments where the large earthquakes occur are mechanically stronger. Freymuller et al. (2008) published results from a 1992-2007 GPS study and found that their results supported the asperity model first presented by Thatcher (1990). Here, “asperities” are defined to be areas where high shear stress is required to generate an earthquake and are the location of large earthquakes and thus these regions are by definition not asperities. However, it is not clear what controls the location of asperities. To add to the complexity, there is also evidence for widespread and continuous repeating low frequency earthquakes (LEFs) on the Alaskan subduction interface (Brown et al., 2013). LEFs are small earthquakes of magnitude of less than ~ 2 . Brown et al. (2013) found no correlation with the location of earthquakes or tremors and LEFs. Regions of creeping vs. locked asperities could be related to changes in the overriding plate composition, angle and speed of subduction, incoming sediment composition or water content, or a combination of these factors. 3D models of the entire Alaska-Aleutian arc could incorporate aspects of subduction angle, sediment and water input. These 3D models could thusly provide a picture of the thermal structure and location of metamorphic facies transitions and dehydration reactions, providing one a means of interpreting the locations of asperities.

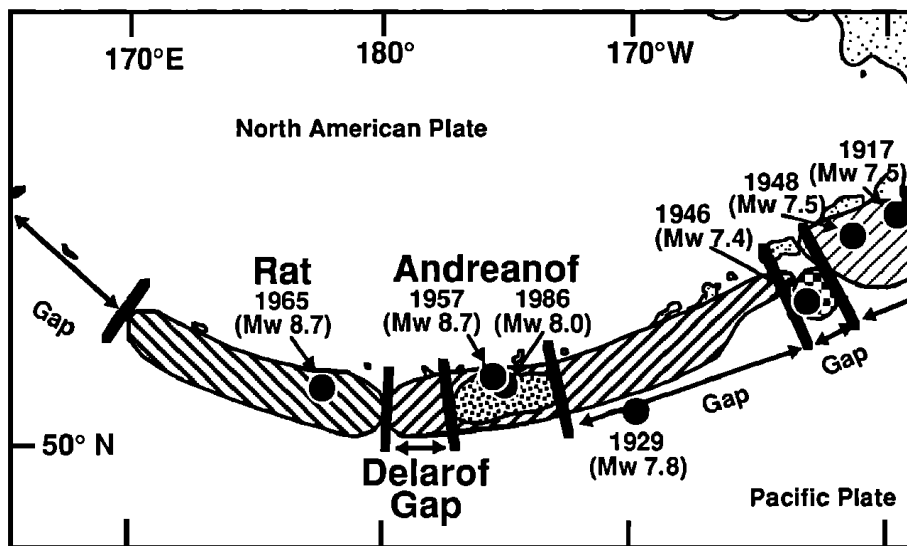


Figure 18: Large earthquakes along the Aleutian Ridge from 1917 to 1986 (circles). Areas of seismic gaps are marked by large arrows. Figure from Ryan and Scholl, 1993.

2c. Volcanology, petrology and geochemistry of the Alaska Aleutian Arc

At Unimak Island on the Alaska Peninsula, the overriding plate transitions from a continental composition in the east, to an oceanic composition in the west (Figure 10). A wide-angle seismic refraction/reflection study near Unimak found a Moho depth of 25 to 30 km beneath the Aleutian Islands. The depth of the Moho increases under the Alaska Peninsula to 40 km (Fliedner and Klemperer, 1999). The transition from the continental arc in the east to an oceanic arc in the west is accompanied by an increase in upper crust velocity from 6.0 km/s under the Alaska Peninsula to 6.5 km/s under the Aleutians; however, the velocities in the lower crust do not change (Fliedner and Klemperer, 1999; Fliedner and Klemperer, 2000).

As the overriding plate transitions from continental to oceanic crust, the style and size of volcanic eruptions changes. Volcanos located on the oceanic portion are basaltic stratovolcanoes that decrease in size from east to west (Marsh and Leitz, 1979). Overtime the stratovolcano matures and smaller vents open up around the initial volcano, which are built simultaneously with the original, larger cone. In the later stages, caldera style eruptions occur with dacite ash flows and rhyodacite pumice. Then activity shifts away to a nearby new location, and a new stratovolcano is built. Volcanoes on the continental portion do not form the smaller, satellite vents. Instead large stratovolcanoes form in a chain along the continental crust (Fournelle and Marsh, 1994).

The Okmok volcano, located on the island of Umnak, is just west of the continental to oceanic transition in the overriding plate. Okmok displays the typical oceanic volcano style as described by Fournelle et al. (1994), and has been fairly active in history with the last eruption occurring in 2008. The volcano underwent two major caldera forming events 12,000 years BP and 2,050 years BP. Prior to 2,050 years BP, an inter-caldera lava sequence known as the Crater Creek series erupted and has been well studied. The lavas are basaltic andesites to andesite in composition. Also present in the inter-caldera

sequence is a basaltic andesite scoria. Shortly after the Crater Creek series was erupted, the 2,050 years BP caldera-forming event occurred. A layer of mafic pyroclastic fall and flow sequences were deposited, as well as a basal rhyodacitic tephra. Following the caldera forming event, The Okmok volcano entered the intra-caldera cone-building stage in which basaltic to andesitic lavas erupted from satellite cones that developed around the caldera event (Finney et al., 2008).

The most recent eruption of the Okmok volcano in 2008 lasted five weeks, starting July 12 and continuing into August (Figure 19, 20, 21). Geologists had very little warning on the impending eruption as it was preceded by an increase in the rate of earthquakes only a few hours before the eruption began. The initial eruption on July 12 produced a 16 km high ash column from the volcano. Measurements from a Moderate Resolution Imaging Spectroradiometer (MODIS) satellite showed two plumes from the volcano, a dark, ash rich plume and a light, water vapor rich plume (Larsen et al., 2009). During that two month long eruption, several hundred million cubic meters of tephra and lahar deposits flowed over the island of Umnak (Figure 19 and 20). The eruption produced basaltic andesite that was slightly more silica rich than the previous eruptions from Okmok (Larsen et al., 2009).

The Island of Umnak is not heavily populated and there was minimal disruption to people on the ground. However, flights across the North Pacific were impacted for several days during the initial stages of the eruption.



Figure 19: Image of the July-August eruption of Okmok volcano. Photo taken August 3, 2008 by Jessica Larsen of the Alaska Volcano Observatory, University of Alaska Fairbanks



Figure 20: A lahar from the July-August 2008 eruption washed away a bridge on the Umak Island. Photo taken July 24, 2008 by Lonnie Kennedy of the Alaska Volcano Observatory, University of Alaska Fairbanks



Figure 21: A 2008 eruption of Mount Okmok produced a new cone with a crater 2,500 ft across. Photo taken September 15, 2008 by C. Neal of the Alaska Volcano Observatory, University of Alaska Fairbanks

The dominant lava type erupted at Alaska-Aleutian volcanoes changes with the changing volcano style. The silica content of lavas along the entire Alaska-Aleutian arc range from 45 to 77 wt% (Fournelle and Marsh, 1994). However for the Aleutians, the oceanic section of the arc, the range is much narrower from 46 to 52 wt% and is dominated by basalts (Myers, 1988). Whereas the higher silica lavas occur mainly on the Alaska Peninsula and Alaska (Fournelle and Marsh, 1994). The change from a higher silica continental crust in the east to lower silica oceanic crust in the west is accompanied by an increase V_p/V_s ratios from east to west (Janiszewski et al., 2013).

The basaltic Aleutian volcanoes span the global range of Fe enrichment from highly enriched tholeiitic basalts to Fe poor calc-alkaline compositions (Zimmer et al., 2010). Volcanoes Mofett, Makushin, Little Sitkin, Islands of Four Mountains, Great Sitkin are all calc-alkaline centers (Figure 22 & 23). Lavas in the central Aleutians spanning 164 to 174 °W are dominated by tholeiitic centers including Okmok and Adagdak (S. M. Kay and R. W. Kay, 1994; Kelemen et al., 2003). The western Aleutians including the Adka area are a mixture of both calc-alkaline and tholeiitic centers. Interestingly though, these variations from calc-alkaline to tholeiitic centers does not vary systematically along the arc or with any subduction zone parameters such as plate age, subduction rate, or obliquity of subduction (Zimmer et al., 2010).

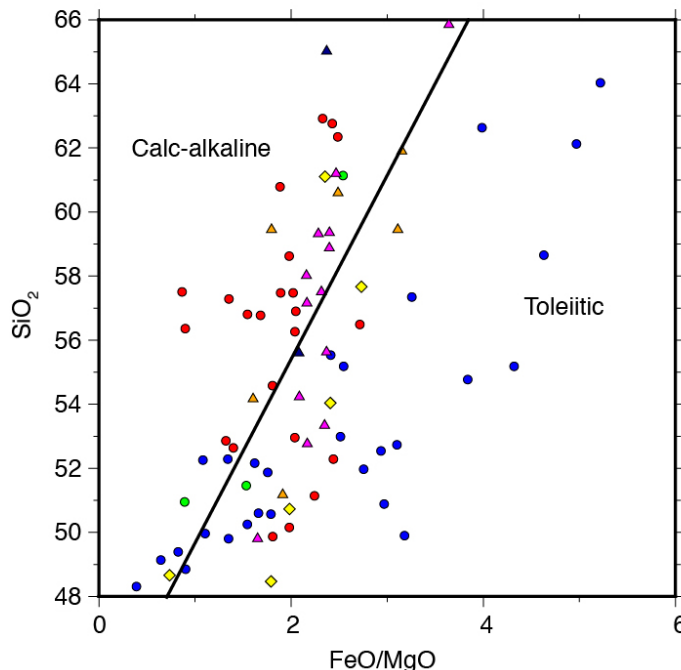


Figure 22: Plot of SiO_2 versus FeO/MgO ratios for Pliocene-recent Aleutian arc volcanic rocks. The black line separates calc-alkaline from tholeiitic. The blue circles are Okmok volcano; red circles, Mofett; green circles, Makushin; darkblue triangles, Little Sitkin; orange triangles, Islands of Four Mountains; magenta triangles, Great Sitkin; yellow diamonds, Adagdak. Data from Kay and Kay (1994).

The formation of tholeiitic basalts is well understood and reproduced in both the laboratory and thermodynamic experiments as the crystal fractionation of dry magma at low pressure. As anhydrous melt crystallizes, olivine and then plagioclase form as the first and second mineral components. Plagioclase then slows the rate of Mg depletion and accelerates the rate of Fe enrichment and thus sets in motion Fe enrichment forming tholeiitic basalts. Calc-alkaline basalts are more complicated. The most apparent drivers in calc-alkaline formation are the suppression of plagioclase as a result of higher water content, high pressure of crystallization, or the bulk composition. Another possible formation mechanism for calc-alkaline basalts is the formation of magnetite which also requires high H_2O contents (Zimmer et al., 2010). Zimmer et al. (2010) measured the H_2O wt% in melt inclusions from eight different volcanoes along the Alaska-Aleutian arc. They found that volcanoes along the arc have H_2O contents that span from 2 to 7 wt%, a range that encompasses both the global high and low of H_2O wt% of melt inclusions ever measured. Mount Shishaldin, located on Unimak Island, is the dry end member of the Aleutian volcanoes measured with only 2 wt% H_2O (Figure 23). In contrast, Mount Augustine has the highest water content of any melt inclusions measured at 7 wt% (Figure 23). Accompanying the variation in H_2O wt%, Zimmer et al. (2010) pointed out that Mount Shishaldin is the most tholeiitic (i.e., the most Fe enriched), while Mount Augustine, located near Cook Inlet, is the most calc-alkaline or FeO depleted volcano. The authors argue that based on their measurements of both the geochemistry and water content of lavas from

volcanic centers along the Alaska-Aleutian arc, there is a strong anti-correlation between iron enrichment or tholeiitic affinities and H₂O wt%. The authors conclude that water leads to calc-alkaline differentiation. Water therefore plays a key role in shaping the geochemistry of the Alaska-Aleutian arc, but it is not clear from this research what exactly is causing the H₂O variations at the different volcanic centers. There is no clear trend in subduction zone parameters, H₂O content of the melt inclusions studies by Zimmer et al. (2010), and Fe enrichment of lavas.

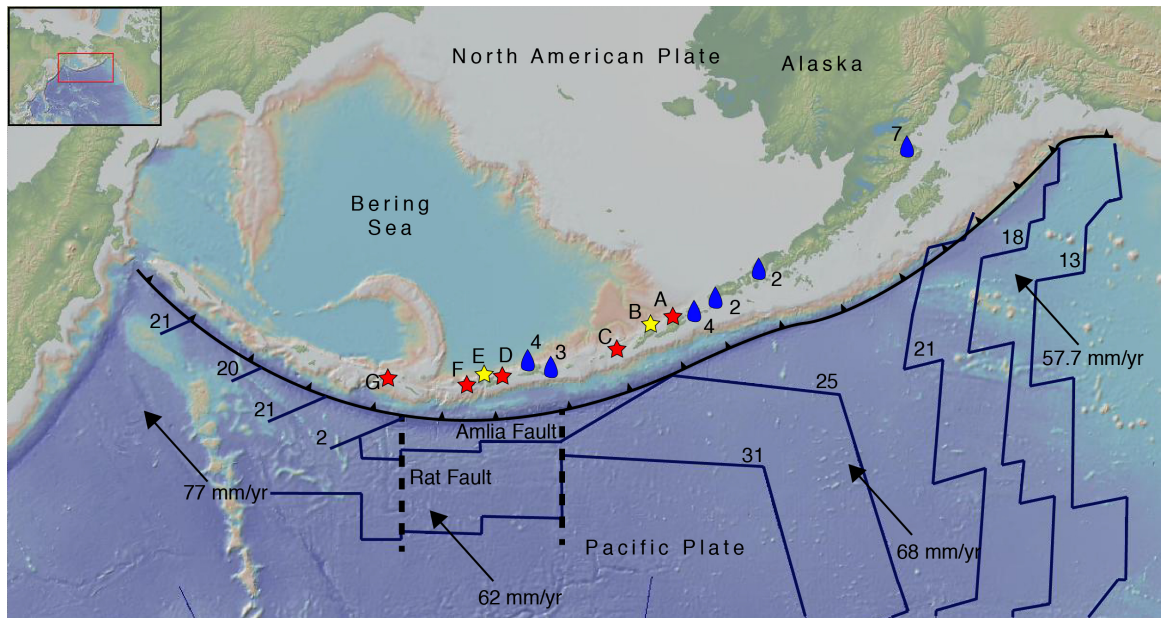


Figure 23: GeoMapApp figure labeling the tholeiitic and calc-alkaline volcanoes along with the measured water content from Zimmer et al. (2010). The blue drops mark the volcanoes where the wt% of H₂O was measured in melt inclusions. The numbers represent the wt% of water. The yellow stars are the calc-alkaline volcanoes B, Mt Okomok and E, Mt Adagak. The red stars are the tholeiitic volcanoes A, Mt Makushin, C, Islands of four Mountains, D, Great Sitkin, F, Mt Mofett, and G, Little Sitkin.

The concentration of major and minor elements varies from the tholeiitic to the calc-alkali centers. For the same silica content, tholeiitic volcanic lavas are higher in Fe, Ti, and K and lower in Mg, Ca, and Al content than the calc-alkaline lavas. These differences increase with increasing silica content. In general, both the tholeiite and calc-alkaline basalts are enriched in trace elements compared to chondrites and ocean ridge basalts, with the greatest enrichment in Cs, K, Ba, and U (Figure 24). Higher K and Ti content of the tholeiitic lavas indicate a higher degree of fractionation at the same silica content.

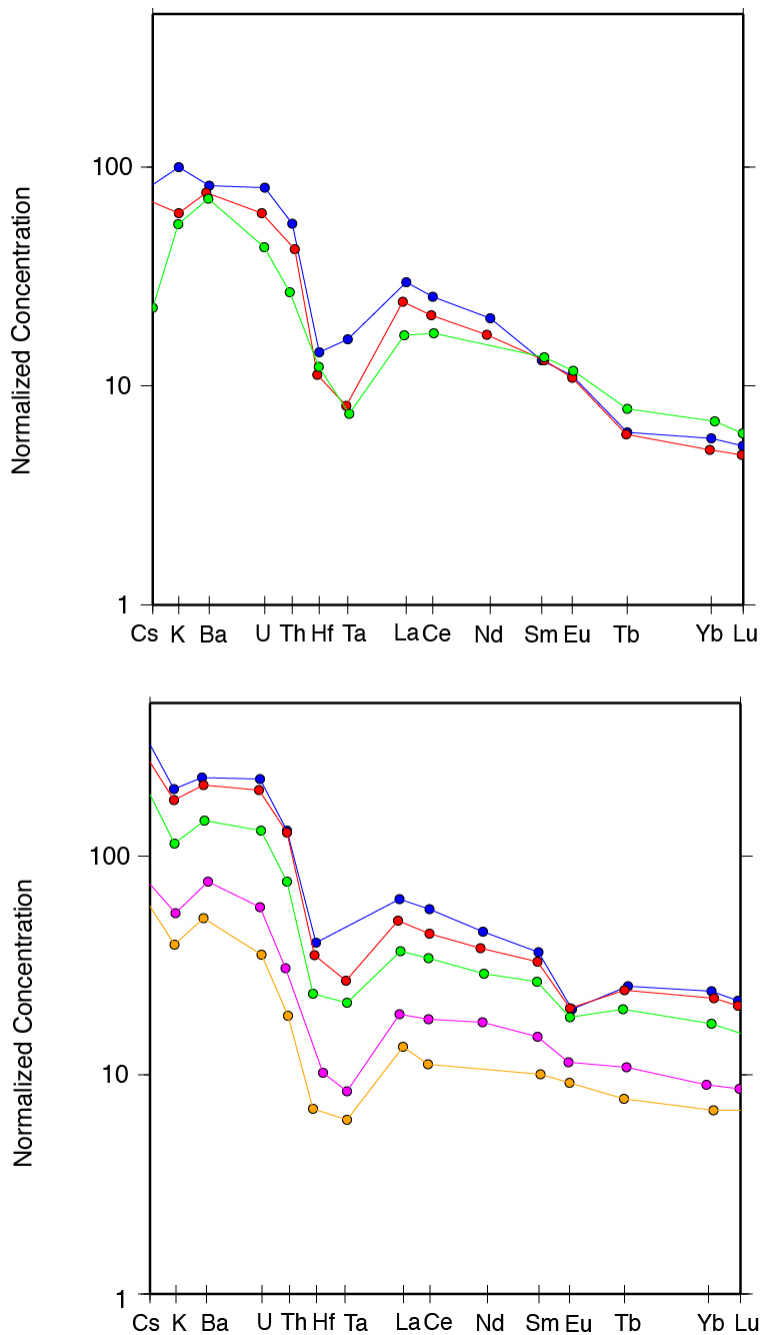


Figure 24: Trace element concentrations along the Aleutian Arc normalized to chondrites. Top: trace element concentrations of three volcanic rock samples from the volcano Buldir (blue is sample BUL3A, red is sample BUL4D, green is sample BUL6A). Bottom: trace element concentrations of samples from the Okmok volcano (blue is sample UM6, red is OK17, green is OK15, pink is OK9, orange is OK6). Data from Kay and Kay (1994).

The majority of basalts (67%) analyzed from the Aleutian arc are low in magnesium ($\text{MgO} < 6\%$) and high in aluminum (Al_2O_3 , 18-22%) (Myers, 1988). These high aluminum basalts are porphyritic (25 to 50%) and dominated by plagioclase phenocrysts which makes up three quarters of the phenocryst assemblage. Olivine is also present (Myers et al., 1985; Myers et al., 1986; S. M. Kay and R. W. Kay, 1994). A minor amount of the basalts from the Aleutians, around 10%, are high in magnesium ($> 9 \text{ wt}\% \text{ MgO}$) and low aluminum (Al_2O_3). The high magnesium basalts are also porphyritic although less so than the high aluminum basalts with the dominant phenocryst being olivine followed by clinopyroxene. Both the high aluminum and high magnesium basalts occur at tholeiitic and calc-alkaline centers alike. High magnesium lavas, which are generally absent from most subduction zones, are abundant in Adka and the western Aleutians (Kelemen et al., 2003).

A long standing debate in the geochemical community is whether the high magnesium basalts are the parental magma that gives rise to the more dominant high aluminum magmas, or if the more dominant composition, the high aluminum lava, is the parental magma. Kay and Kay (1994) argue that olivine tholeiite high in magnesium is the parental magma, produced from mantle peridotite and altered by the material from the subducting slab. They contend that the high aluminum basalts form at the base of the crust from crystallization of olivine and clinopyroxene of the high Mg basalts. Mass balance models have been used to support a high magnesium parental magma for the Aleutian arc (Conrad and R. W. Kay, 1984; Brophy, 1986; Gust and Perfit, 1987). Gust and Perfit (1987) found that fractionation of approximately 20% olivine and pyroxene from high magnesium basalts can produce high aluminum basalts. However, Myers et al. (1986) argue against the crystal fractionation model proposed by Kay and Kay (1994) because the concentration of incompatible elements in the high magnesium basalts are higher than in the high aluminum basalts. Myers (1988) also points to overlap in rare Earth element (REE) patterns, and trace element composition of the high aluminum and high magnesium basalts, as another argument against the high aluminum basalts being formed from crystal fractionation of the high magnesium basalts (Figure 25). Instead Myers et al. (Myers et al., 1985; 1986) proposed that the more dominant lava, the high aluminum basalts, are the parental magma formed from melting of the eclogized subducting slab. Then as high aluminum basalts ascend through immature magma chambers, the magma interacts with the host rock wall to produce high magnesium basalts (Myers and Marsh, 1987). As more magma passed through the host rock wall, the magma would be altered. By this hypothesis high magnesium basalts would be secondary in origin and be most abundant in immature magma chambers. High aluminum basalts should dominate in the later stages of volcanic eruptions. Myers et al. (1985) use geochemical data from two different volcanic centers, Adka and Atka, to support their hypothesis.

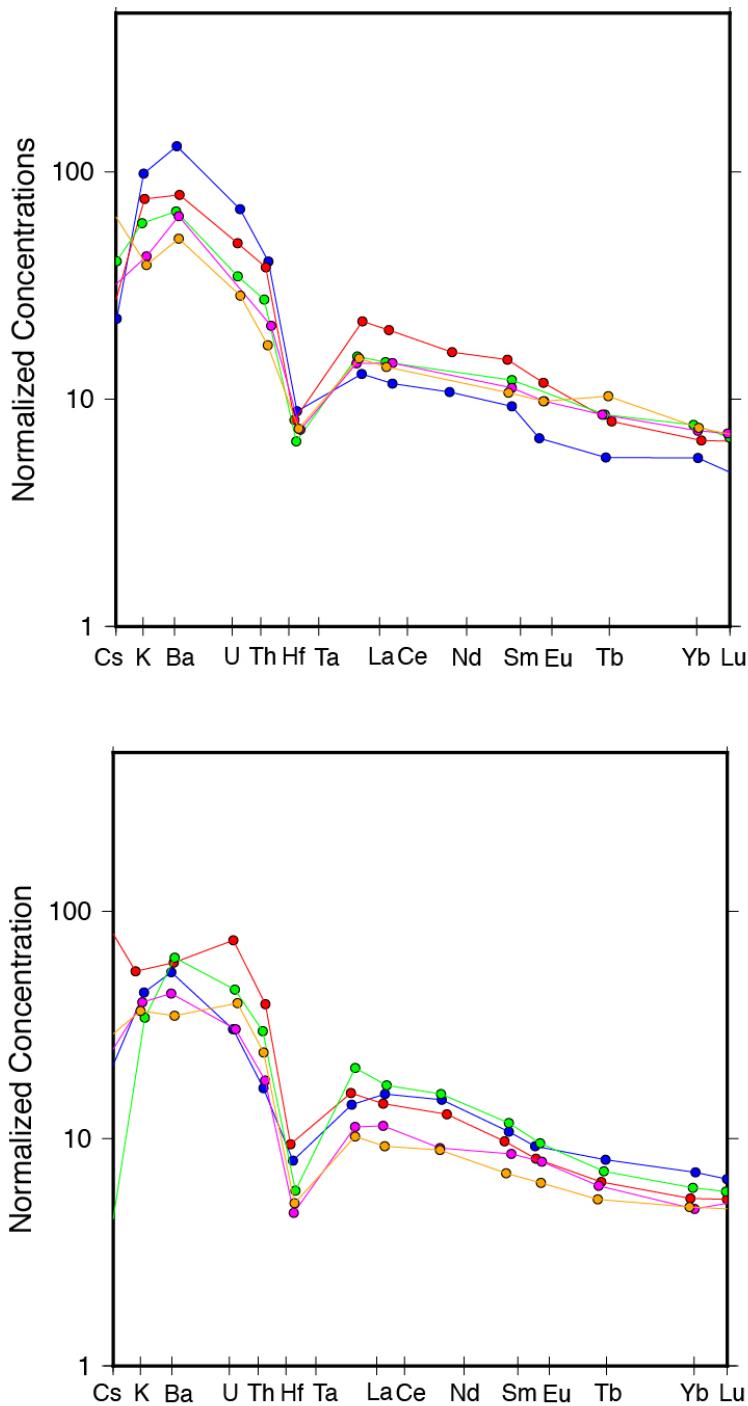


Figure 25: Trace element concentrations along the Aleutian Arc normalized to chondrites. Top: trace element concentrations of three volcanic rock samples from the volcano Buldir (blue is sample BUL3A, red is sample BUL4D, green is sample BUL6A). Bottom: trace element concentrations of samples from the Okmok volcano (blue is sample UM6, red is OK17, green is OK15, pink is OK9, orange is OK6). Data from Kay and Kay (1994)

The volcanoes Adka and Atka are located in the central Aleutians, approximately 150 km apart. Similar to other lavas on the Aleutian arc, lavas from Adka and Atka are highly porphyritic with the dominant phenocrysts being plagioclase, followed by olivine, orthopyroxene, and clinopyroxene. Lava from the Atka center contains fewer phenocrysts than Adka. Both Adka and Atka are calc-alkaline with high aluminum lavas and elevated alkali oxides such as K_2O and CaO . MgO and TiO_2 are present in lower concentrations in Adka and Atka lavas. Lavas from Atka show a systematic trend in which Al_2O_3 , FeO , MgO , and CaO all decrease with increasing silica. However lavas from Adka show no such systematic trend. Furthermore Atka lavas show much less variability in major and trace elements than Adka. For example $^{87}Sr/^{86}Sr$ of Atka ranges from 0.70320 - 0.70345 whereas the $^{87}Sr/^{86}Sr$ range for Adka is broader 0.70285 - 0.70330 (Figure 26). Myers et al. (1985) propose that smaller, younger, and less mature volcanic plumbing system will result in more wallrock and ascending lava interaction. Lavas erupted from these centers, such as Adka, should exhibit greater chemical and petrological variability. In contrast, magmas erupted from established magma plumbing systems should have less contamination by wallrock that has been altered by successive pulses of ascending magma. The magma erupted from mature volcanic centers should be insulated against heat loss and contamination of the surrounding wall rock, and show less chemical and petrological variability as a result. The insulation from cold wallrock in mature magma systems would promote crystal fractionation and generate more systematic chemical variations. Another indicator Myers et al. (1985) use to support their hypothesis is the greater abundance of xenoliths at Adka. They argue that early crystallization of phenocrysts might also lead to gases and vapor building up and more explosive eruptions, causing more abundant xenoliths for immature volcanic centers.

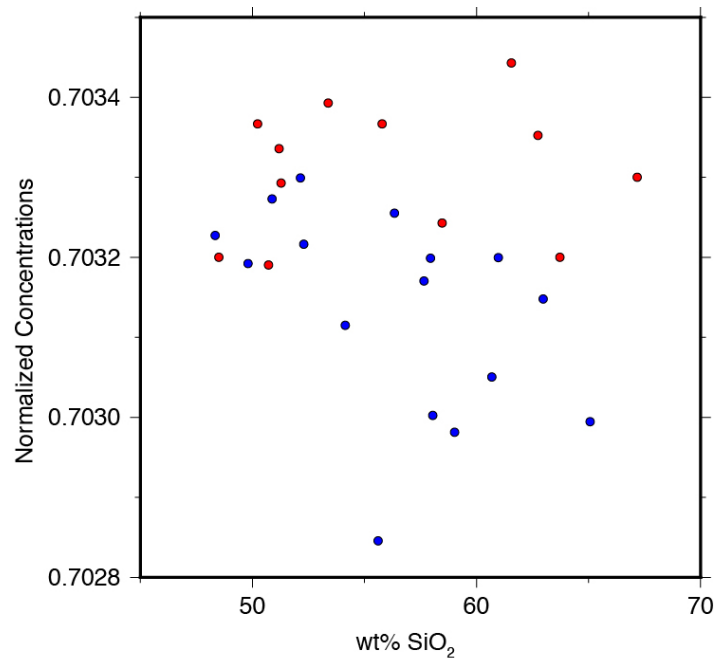


Figure 26: Initial $^{87}Sr/^{86}Sr$ versus SiO_2 from Atka (red circles) and Adak (blue circles). Data from (Myers et al., 1985).

The less abundant high magnesium lavas in the Aleutians are of special interest because they have similar characteristics to continental crust. Average continental crust is andesitic, has a high magnesium number (magnesium number is $Mg/Mg+Fe$) ranging from 0.45 to 0.54, has a silica wt% > 54%, and is enriched in incompatible elements. Also, the average P wave seismic velocity of continental crust is 6.45 km/s (Smithson et al., 1981; Braile et al., 1989; Kelemen, 1995; Rudnick, 1995; Rudnick and Fountain, 1995; Nikolas I Christensen, 1995). Lavas with similar properties only occur at arcs, such as in the western Aleutians. The only other regions around the globe with lavas close to continental crust composition are arcs underlain by older, continental basements such as Central America, southern Andes, SW Japan, and the Cascadia Arc (Kelemen et al., 2003). As a result, many people have hypothesized that continental crust is born at volcanic arcs (Taylor, 1967; McLennan and Taylor, 1982). However, it is puzzling how abundant continental crust, that is generally andesitic, has been created when the only place where lavas with similar characteristics occur at island arcs. Furthermore, most arc lavas are dominated by low Mg number basalts and andesites. Thus, how do we create continental crust? If arcs are not generating continental crust initially, then perhaps island arcs are altered after formation to a continental crust composition (Smithson et al., 1981), possibly through secondary melting or delamination of the lower crust (Arndt and Goldstein, 1989; S. M. Kay and R. W. Kay, 1994). Others have hypothesized that there are actually more high Mg# andesites at arcs than we see at the surface because these high Mg# andesites are crystallizing at great depths due to their higher viscosity. Shillington et al. (2004) conducted a wide-angle seismic data study in the eastern and central Aleutians. They found that the upper crustal velocity on the Aleutians is between 6.0 to 6.5 km/s. The authors conclude that it is difficult to tell the composition of the upper crustal layer from these velocities due to fractures. Outcrops at the surface suggest that the upper crust is dominated by basaltic lava flows with plutonic rocks of andesitic composition present as well. The middle crust velocities range from 6.5-7.3 km/s with an average of 6.92 km/s. The authors interpret these velocities to represent both mafic and intermediate plutons. While there is a large range in velocities in the middle crust allowing for variable composition, the average suggests that overall the middle crust is mafic. However, the slower portions of the middle crust support the hypothesis presented by Kelemen et al. (2003), that the middle crust contains andesitic plutons that crystallize at depth. For example, Shillington et al. (2004) find velocities of 6.8 km/s in the middle crust near the Four Mountains and argue that these velocities cannot represent mafic rock. Shillington et al. (2004) also point out that middle-crustal rocks sampled from obducted arcs support their velocity finds of a mixture of basaltic and andesitic compositions for this region of the crust. The lower crust is characterized by high velocities of 7.3 - 7.7 km/s, and the authors interpret this to indicate garnet bearing rock, gabbros, and ultramafics. Similar findings of lower crustal velocities are reported by other authors (Fliedner and Klemperer, 2000; Janiszewski et al., 2013), producing the consensus that if continental crust is being generated at the Alaska-Aleutian arc, then the ultramafic lower crust would have to be highly altered or removed via delamination (Holbrook et al., 1999; 2004).

2d. Sedimentation and water content of the Alaska-Aleutian Arc

From the above discussion on the petrology and geochemistry of the Aleutian Arc, it is clear that water plays a significant role, for example, in the anti-correlation between water content and Fe enrichment of volcanic lavas. But how does water become incorporated into the subduction process? Subducting plates originate at mid-ocean-ridges where magmas have the lowest H₂O content recorded around the globe, < 0.5 wt% (Zimmer et al., 2010). However, Zimmer et al. (2010) report a range of 2 to 7 wt% H₂O in Aleutian Arc melt inclusions. Somewhere between a plate's birth at a mid-ocean-ridge and its subduction, water becomes incorporated into the oceanic crust. One method of incorporating water into a downgoing plate is through the sediments. We know that sediments deposited on the ocean floor are subducted into the trench and return to the surface via the volcanic arc in a relatively short time period, because of the presence of ¹⁰Be, a cosmic-ray produced nuclide with a short 1.5 Myr half-life, in arc lavas (S. M. Kay and R. W. Kay, 1994). Another indicator of sediment subduction comes from the Pb isotopic data. Aleutian Arc Pb isotopic values consistently are more similar to terrigenous sediment values than MORB or ocean island basalts (Figure 27).

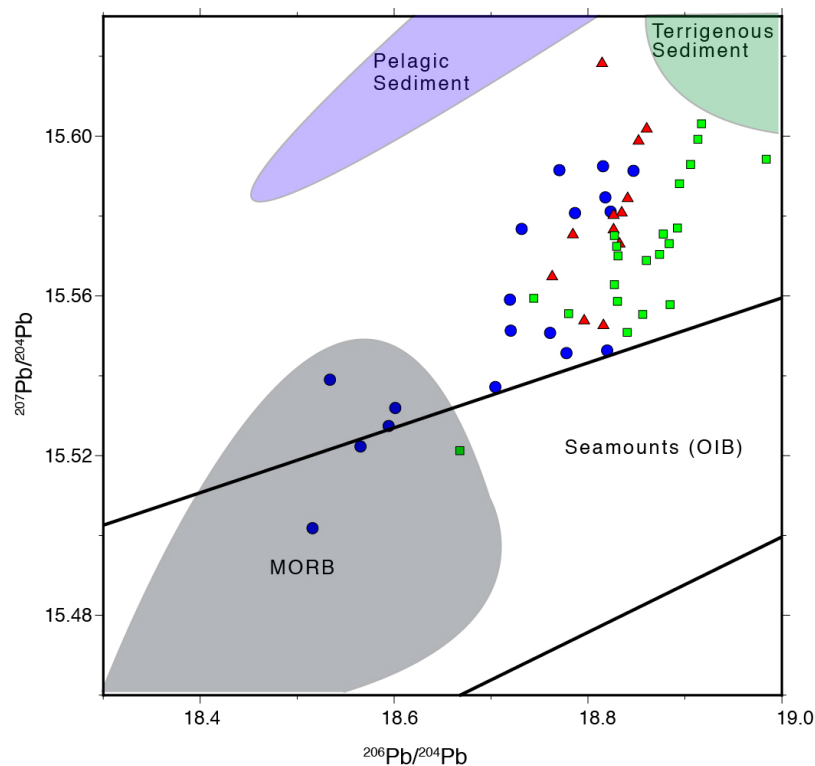


Figure 27: Plot shows $^{207}\text{Pb}/^{204}\text{Pb}$ versus $^{206}\text{Pb}/^{204}\text{Pb}$ for Aleutian Arc. The blue circles are Adak Island, the green squares are Umnak Island, and the red triangles are Atka Island. The data trends are consistent with mixing of oceanic type magmas and sediments. Data from Kay and Kay (1994).

It is clear that sediments are entrained in the subduction zone process and returned to the surface at the arc, but how much sediments are involved? Roughly half of the material eroded off the Aleutian Arc goes northward into the Bering Sea, and the other half southward into the Pacific. The bulk of the sediments entering the Pacific pool in the forearc basin and do not enter the trench. Sediments that do make it to the trench thicken from the eastern side of the Alaska Peninsula to the eastern end of the Aleutian Islands (160 to 172 °W). In the eastern and central Aleutians (east of 185 °W), a 20-40 km wide, and as much as 6 km thick, accretionary prism of sediment lies along the Aleutian trench. West of 185 °W, the wedge rapidly decreases in size. Sediment thickness changes rapidly across fracture zones. At the Rat fracture zone (182 °W) sediments are 1 km thick. By 190 °W that thickness decreases to just a few hundred meters (Figure 28 and 29). Other sediment thickness estimates are thicker for the Alaska and the Aleutians at 2.5 km and 1.5 km respectively (Clift, 2004). Kelemen et al. (2003) showed that the flux of sediment to the Aleutian subduction system increases from east to west. From 67 m³ of sediment per meter of arc-length per year (m³/m/yr) at Cold Bay (163 °W) to 95 m³/m/yr at Seguam (172.5 °W) where Amlia Fracture zone. West of Seguma the sediment flux decreases systematically to 20 m³/m/yr (Figure 30).

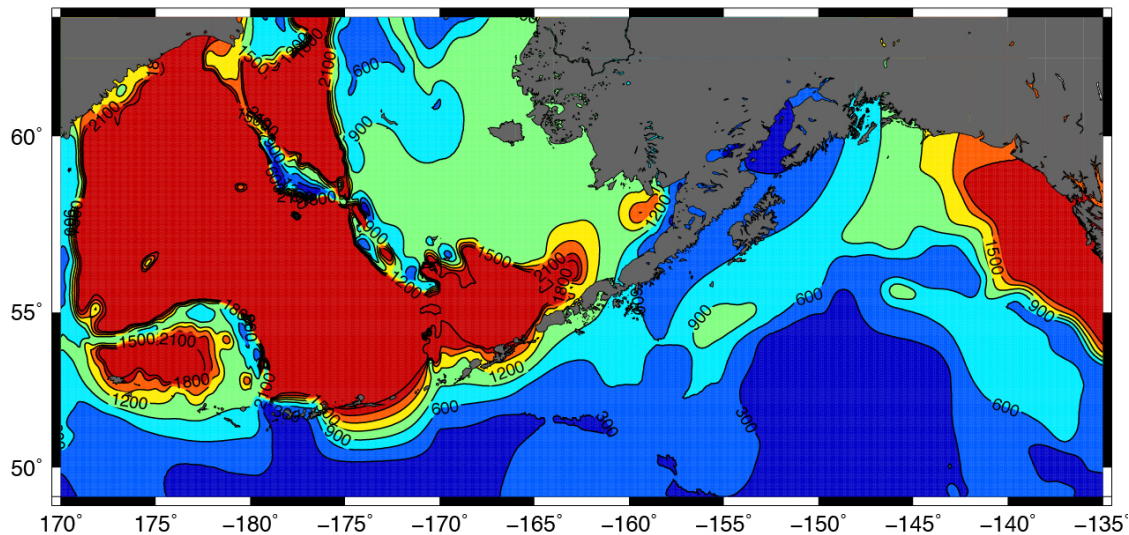


Figure 28: Sediment thickness map of the North Pacific and Bering Sea. The contour interval is 300 m. The sediment thickness is greatest near the 170 °W longitude (Divins, 2002)

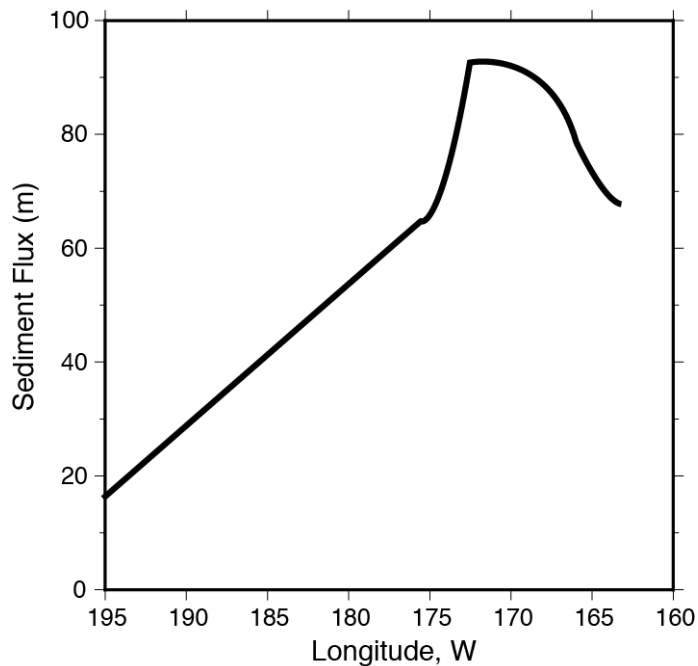


Figure 29: Sediment thickness with respect to longitude. Sediment thickness increases along the Alaska Peninsula to 170 °W, and then drops rapidly toward the west to 175 °W, along the central and western Aleutians sediment thickness generally decreases. Data from Kelemen et al. (2003).

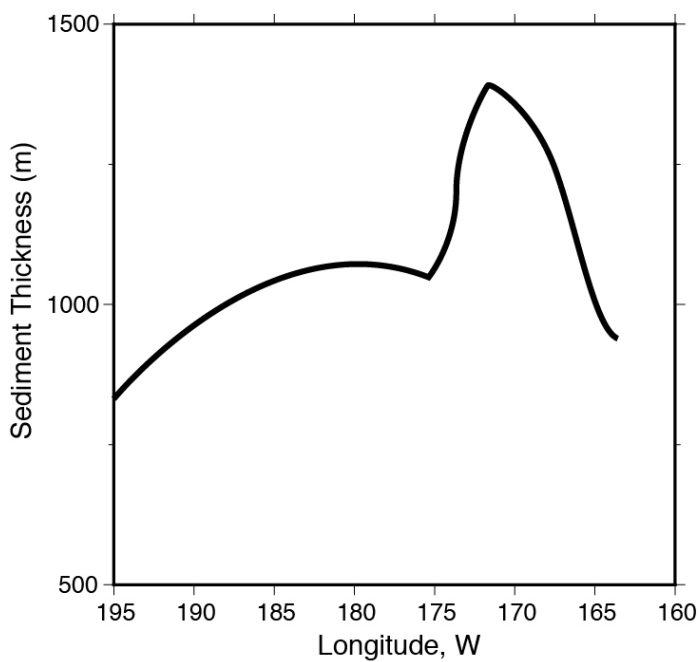


Figure 30: The flux of sediment into the Pacific mirrors the sediment thickness profile in that sediment flux increases to 170 °W and then decreases west of 170 °W. Data from Kelemen et al. (2003).

There are only two drill sites along the Alaska-Aleutian subduction system that allow for a detailed study of sediments near the trench. Site 183 is located on the northern edge of the Aleutian abyssal plain, off the coast of the Alaska Peninsula (J. S. Creager and Scholl, 1973). The drill site 183 comprises a 505 m thick core of Holocene to middle Miocene pelagic deposits (0-210 m) (Figure 31). Above 185 m a diatom-rich silty clay and diatom ooze with ash layers exists, above 127 m ice rafted pebbles are common, from 210-239 m is Miocene and upper Oligocene pelagic clay. Nannofossil chalk of middle to lower Oligocene occurs at 239 to 248 m, and 248 to 501 m depth in the core contains lower Oligocene to upper late Eocene turbidite beds, with clay, size graded silt, and silty sand. From 501-505 m nannofossil limestone, calcareous ferruginous clay, and pyritic and aragonitic limestone is present. Conifer dominated pollen assemblages and large populations of nannofossils in lower Oligocene and Eocene implies that the sediment source for Alaska was high latitudes, which is what we expect for that time period. The oldest datable sediment is 12 my younger than the basalt it lies on top of (anomaly 24), and this may reflect non-deposition of Paleocene deposits, which is also observed at site 192 (J. S. Creager and Scholl, 1973). Plank and Langmuir (Plank and Langmuir, 1998) consider site 183 to be the only representation of the seafloor south of the trench. Seismic reflection data suggests that there is more than 1 km of sediment at the trench but only 500 m of sediment was drilled above the basalt.

Site 192, the only other drill site in the north Pacific along the Alaska-Aleutian subduction system, is located on the summit of Meiji Guyot, the northernmost seamount on the Emperor chain (J. S. Creager and Scholl, 1973). At only 3000 m water depth atop Meiji Guyot, the sediment thickness at site 192 is 1044 m (Figure 31). From 0-320 m depth is composed of Holocene and Pliocene diatomaceous silty clay and diatom ooze with abundant volcanic ash beds, and ice rafted erratics through the first 110 m. From 320-550 m upper Miocene diatom rich clay persists. Lower to middle upper Miocene is composed of diatom rich clay 550 - 705 m, This is followed by claystone with calcareous layers, 704 to 940 m, of lower middle Miocene through Oligocene in age. From depths 940-1044 m chalk and calcareous claystone, 950-1000 m these beds are composed of graded sand and silt. An unconformity separates the lower Eocene and Cretaceous. At 1044 m the sedimentary sequence overlies alkali basalt. The occurrence of ice rafted debris and volcanic ash deposits in the middle Pliocene indicates the formation of glaciers in Kamchatka and intense volcanism in the Kamchatka and Kuril region 3 Ma. 550 m thick of diatom-rich clay indicates high fertility in the water back to late Miocene 8-10 Ma. In the Oligocene, the seamount was buried beneath 500 m of pelagic clay, now full of worm burrows. Miocene times suggest a 50 m/Myr sedimentation rate which is very high for pelagic sediment. Earlier during the lower Miocene and Oligocene rates are much slower, less than 10 m/Myr (J. S. Creager and Scholl, 1973).

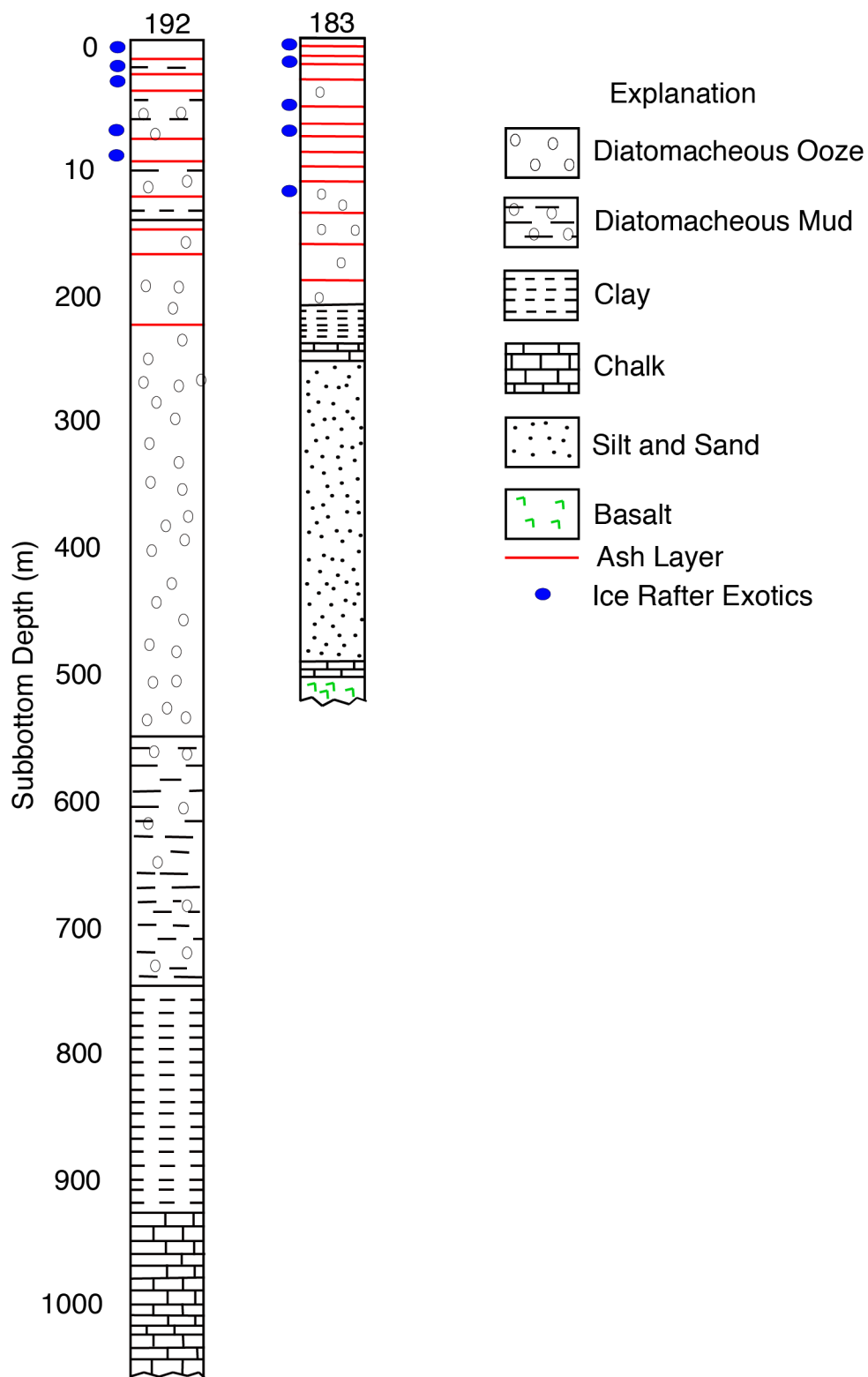


Figure 31: Stratigraphic columns of DSDP drilling sites 192 and 183 both in the far north Pacific. Data from Creager and Scholl (1973).

Sediment porosity is estimated between 30 and 40%, however most of this porosity is lost during subduction and compaction (Clift, 2004). From the drill cores 183 and 192, Plank and Langmuir (1998) estimated that the average sediment thickness for Alaska is 780 m, density 1.8 g/cc, and water 32.4% content. For the Aleutians they estimated the average sediment thickness 350 m, density 1.64 g/cc, water 41.54%. Only around 0.4 km of sediment is estimated to be subducted in Alaska and 0.3 km of sediment is subducted in the Aleutians, the rest of the sediment is scraped off into the accretionary prism (Scholl and Huene, 2007). The sediments are more than likely highly hydrated prior to subduction, but during subduction that water is squeezed out as the sediment compacts. Therefore, hydration of the subduction zone via sedimentation is likely low.

The subducting crust and mantle most likely play a key role in bringing water down into the subduction zone. Estimates of the hydration of the crust and upper mantle of the incoming plate are highly uncertain. Recent work conducted in Nicaragua found slow P wave velocities most likely due to hydration of the incoming plate correlate to the depth of extensional earthquakes in the incoming plate (Lefeldt et al., 2009). The extensional outer rise earthquakes are thought to facilitate serpentinization and thus hydration of the crust and mantle (Faccenda et al., 2009). Emry and Weins (2015) examine the maximum depth of outer-rise earthquakes in the Alaska-Aleutian subduction zone as a means of estimating the amount of hydration of the incoming plate. They find that the majority of earthquakes occur to 5 km depth below the mantle. However, outer-rise extensional earthquakes can occur to depths as great as 25-30 km (Figure 32). In the north Pacific, outer-rise earthquakes are deepest in the central and western Aleutians, and shallower in Alaska and the Alaska Peninsula. Using lateral variations in incoming plate earthquake depths as an estimate to serpentinization depth and assuming partially hydrated mantle to these depths of 0.5 wt% H₂O, the authors estimate 4.4×10^8 Tg/Myr of water is carried into the Alaska-Aleutian subduction zone, with the deepest hydration occurring in the central and western Aleutians. The authors then assume a general constant pattern of lateral heterogeneity of incoming plate earthquake depth and thus hydration globally and estimate that $14\text{-}18 \times 10^8$ Tg/Myr of water is input into the Earth's mantle via subduction zones. The estimate of incoming plate hydration in Emry and Weins (2015) is 1.5 times greater than the global estimate presented by van Keken et al. (2011), slightly larger than Hacker (2008), two times that of Jarrard (2003). While it is difficult to estimate the fluid flux into subduction zones, research by George et al. (2003) suggests fluid plays a large role in the subduction systems. Those authors examined young lavas erupted along the Alaska-Aleutian arc and found a correlation between convergence rate, volcano volume, and ²³⁸U suggest magmatic output is closely linked to the size of fluid flux that occurred less than 10 years before eruption.

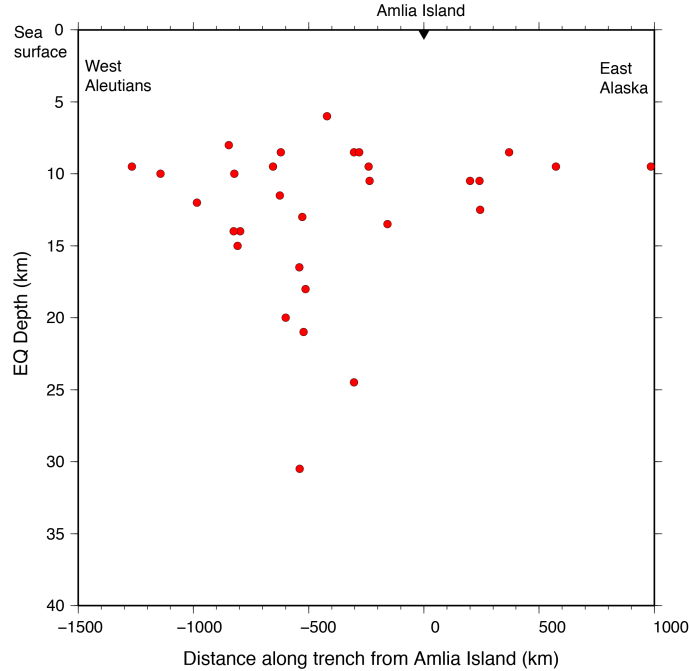


Figure 32: Depth of outburst earthquakes along the Alaska-Aleutian trench. Data from Emry and Wiens (Emry and Wiens, 2015).

3. Methods

3a. Solving the governing equations

For the 3D benchmarking and resolution testing I conducted, I used the Sepran finite element modeling package (Cuvelier et al., 1986). The slab and wedge flow are evaluated by solving the conservation of mass and momentum equations in an incompressible fluid. It has been demonstrated by Lee and King (2009) that for shallow depths, an incompressible model is appropriate. I ignore any effects of compressibility such as viscous dissipation, adiabatic heating and cooling, and secondary thermal buoyancy in the wedge. The equations of motion are

$$\nabla \cdot \mathbf{v} = 0 \quad (1)$$

$$\nabla(\eta \dot{\boldsymbol{\varepsilon}}) - \nabla P = 0 \quad (2)$$

where \mathbf{v} is velocity, η is viscosity, $\dot{\boldsymbol{\varepsilon}}$ is the strain rate tensor, and P is dynamic pressure. We also solve the steady-state heat equation.

$$\rho c p (\mathbf{v} \cdot \nabla) T = \nabla \cdot (k \nabla T) + Q \quad (3)$$

where ρ is density, cp is specific heat capacity, T is temperature, k is thermal conductivity, and Q is the internal heating component. Both an isoviscous mantle rheology and a non-Newtonian, temperature and stress dependent dislocation creep laws for dry olivine

(Karato and Wu, 1993) are used in the 3D benchmark and resolution testing models, with effective viscosity given by

$$\eta(T, \dot{\epsilon}) = A^{-1/n} \mu e^{[E/nRT] \dot{\epsilon}^{(1-n)/n}} \quad (4)$$

where A is a constant, μ is the shear modulus, E is the thermal activation energy, n is the stress exponent, and R is the gas constant. All physical parameters used in these models are given in Table 1.

All models presented here are semi-kinematic-dynamic in that I solved for the velocity in the slab and wedge, prescribing velocity only along the top of the subducting slab. The only other velocity prescribed in the model is that the overriding plate is held stationary. The upper portion of the mantle wedge, from the base of the overriding plate to 95 km depth, is an open inflow boundary. Below 95 km and between the slab and edge of model, the boundary is an outflow boundary. The base of the mantle wedge is also an outflow boundary.

The temperature boundary conditions are such that the top of the overriding crust is 0 °C. The slab inflow is defined by the half-space cooling model. The mantle inflow persists from the base of the overriding plate to 95 km. The mantle potential temperature is 1300 °C for the 3D benchmark in accordance with van Keken et al. (2008). For all other models presented here, the mantle potential temperature of 1421.5 °C (C. A. Stein and S. Stein, 1992). The overriding plate is defined by a linear crustal geotherm. I do not take shear heating into account.

T mantle	1421.5 °C*
ρ	3300 kg/m ³
cp	1250 KJ/kg/K
k	2.5 W/m/K
A	$3.5 * 10^{22} \text{ s}^{-1**}$
μ	80 GPa**
E	540 kJ/mol**
n	3.5**

Table 1: Physical parameters used in the thermal modeling. * from (C. A. Stein and S. Stein, 1992), ** from (Karato and Wu, 1993)

3b. Benchmark and resolution testing

To verify that the 3D models are solving the governing equations correctly and to determine the required resolution for an accurate solution, I set up a 3D model following the 2D benchmark models from van Keken et al. (van Keken et al., 2008). In 2D the

question of mesh resolution was less vital because 2D meshes are much smaller and can be easily overresolved for the problem. However in 3D the balance between an accurate solution, memory space, and CPU time is of critical importance. The 3D benchmark models are set up similar to the 2D benchmark models in which the models are 600 km in depth by 660 km wide with a 45° dipping slab (Figure 33). The overriding plate in the benchmark is 50 km thick. I tested both isoviscous and olivine rheology for a slab velocity of 5 cm/yr, and a slab age of 50 Myr. The model boundary conditions are set up according to van Keken et al. (2008). I also compared the 3D benchmark results with an entirely kinematic slab, similar to the 2D models of van Keken et al. (2008), to a semi-kinematic dynamic slab in which the slab velocity is only prescribed on the slab surface and the conservation of momentum equation is solved in the slab volume.

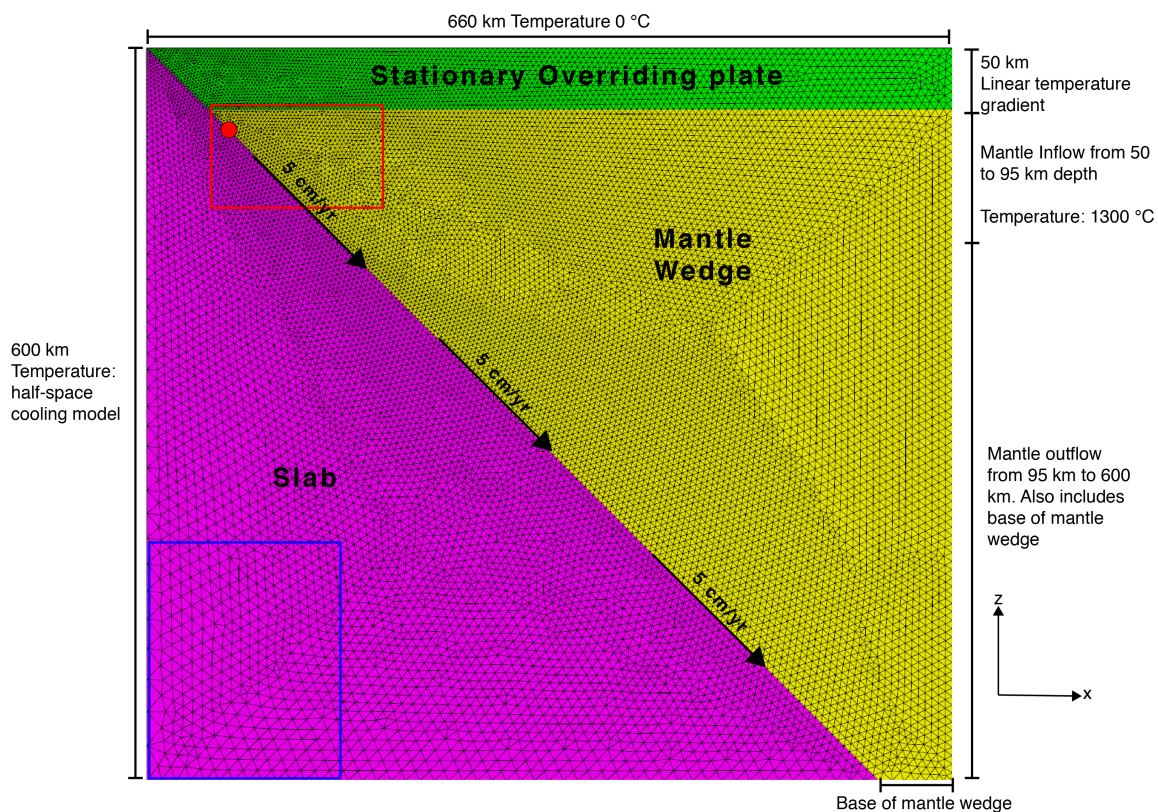


Figure 33: Side view of 3D benchmark mesh. The slab is pink, the mantle wedge is yellow, and the overriding plate is green. The red box outlines the mantle wedge where velocity and temperature change most rapidly, and therefore the region has the highest resolution of 2 km. The red dot is the 60 km depth point on the slab surface. The base of the slab, mantle inflow, and mantle outflow area have resolution of 7 km. The largest elements in the mesh, outlined by the blue box, occur in the base of the slab inflow area and are 30 km. The black arrow indicates the subduction velocity on the slab.

I compared the temperature of the slab surface at the 60 km depth point (marked by red dot on Figure 33) of the 3D models to the 2D model results presented in van Keken et

al. (2008). I also compared the 2D and 3D model slab surface temperature between 0 and 210 km depth as defined by the L2 norm.

$$T_{slab} = \sqrt{\frac{\sum T_{ij}^2}{36}} \quad (5)$$

where T_{slab} is the temperature of the slab from depths 0 to 210 km.

3c. 2D vs. 3D model comparison

To test if the 3D Alaska-Aleutian model is solving for velocity and temperature accurately, I set up 2D and 3D meshes based on a cross-section from the rotated and flattened Alaska-Aleutian model (Figure 34 and 35). The 2D mesh resolution is 4 km in the mantle wedge, 12 km at the base of the slab, 9 km at the mantle inflow, and 32 km for the largest elements in the model.

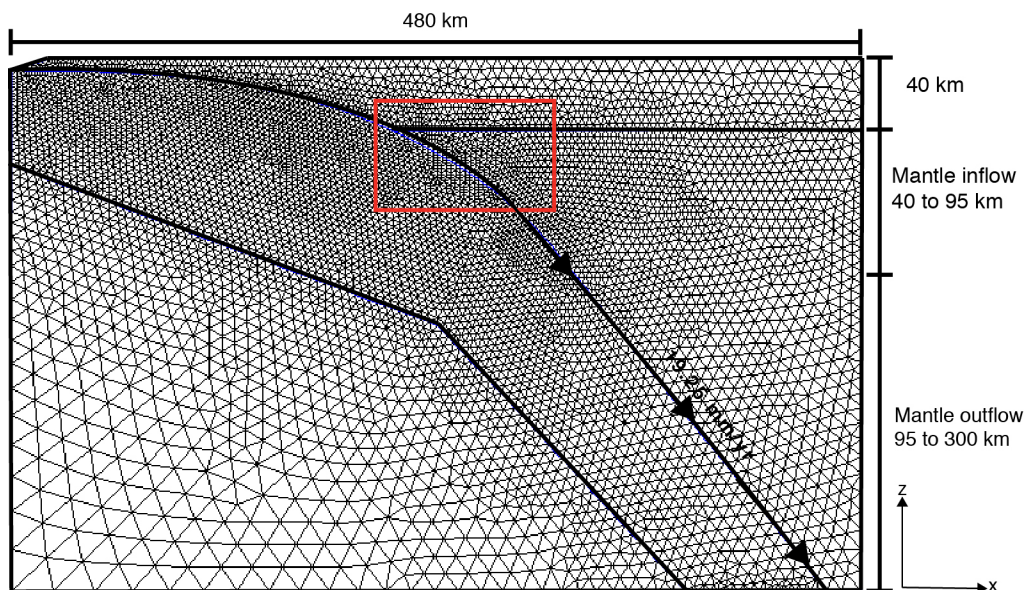


Figure 34: Image of the 2D Alaska-Aleutian cross section. Red box outlines area of highest resolution at 4 km. The resolution for the mantle inflow, outflow, and base of the mantle wedge is 9 km. The largest elements are 32 km. The slab velocity is 19.25 mm/yr

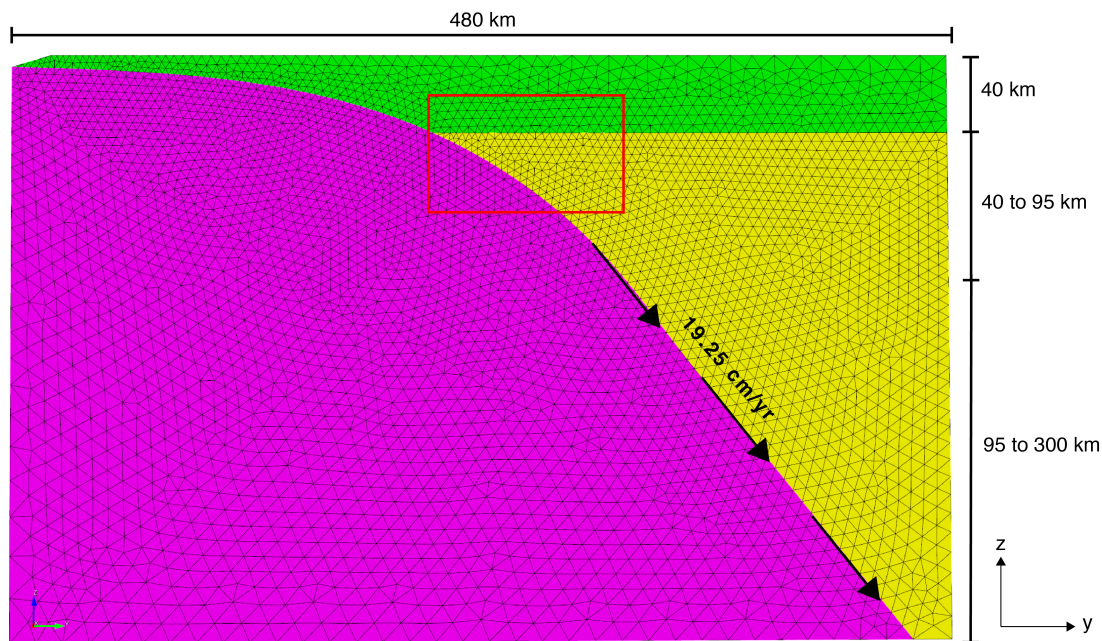


Figure 35: Image of the 3D Alaska-Aleutian cross section. Red box outlines area of highest resolution at 4 km. The resolution for the mantle inflow, outflow, and base of the mantle wedge is 9 km. The largest elements are 32 km. The slab velocity is 19.25 mm/yr

The model parameters were set up such that for both the 2D and 3D case, the slab speed was 19.25 mm/yr, the age of the subducting plate was 100 Ma, and the overriding plate was 40 km thick. The slab speed is much lower than the actual rate of the Pacific Plate subduction. However, a more realistic speed could not be used due to the coarse resolution of the block. I did not have the memory space to use a more resolved block.

3d. Mesh development

The finite element mesh of the Alaska-Aleutian arc is created in the finite element meshing program Trelis, and extends from the Alaska Peninsula to the western Aleutian Islands, approximately 3,000 km distance. The base of the model is 300 km depth. Trelis is commercial finite element software based on the open source software CUBIT first developed by the Sandia National Laboratory. It provides an interface for geometry development, geometry cleanup tools, and finite element meshing algorithms that allow the user to produce complex 3D finite element meshes.

The estimation of the slab surface is based on interpolation points from Syracuse and Abers (2006) which used both local and teleseismic earthquake catalogs to construct slab contours based on the Wadati-Benioff zone for 33,000 km of global arcs. In Alaska, seismicity generally extends no deeper than 200 km depth. Seismicity as deep as 300 km only occurs under the eastern Aleutians. Our models extend to 300 km depth everywhere, and thus interpolations of the slab surface deeper than the Wadati-Benioff zone is necessary in some locations. Because we do not have high resolution information on the deep slab surface, continuation of the slab surface below interpolation point depth was based on the assumption that in the absence of information to the contrary, the slab

continues at depth without changing in angle or curvature. Before utilizing the Syracuse and Abers (2006) interpolation points for the Alaska-Aleutian slab, I removed the curvature of the earth, flattening the models. A spline is used to interpolate between slab surface points and the base of the slab at 300 km. Once a series of cross-sections are built, they are linked together into a 3D geometry via another spline.

The geometry is meshed using finite element meshing techniques and tetrahedron elements. Tetrahedrons were used because currently it is the only element shape Sepran supports. The mesh is resolved according to the benchmark results with 2 km in the mantle wedge, 7 km for the mantle inflow, and the largest elements at 32 km.

3e. Velocity in the slab

Previous 2D subduction zone modeling defined velocity in the slab kinematically (van Keken, 2003; van Keken et al., 2008; van Keken et al., 2011). In the 3D models, we solved Stokes flow in both the mantle wedge and slab. In 2D, solving for velocity in a subduction zone is straightforward; all flow remains parallel to the slab surface and thus no violation of conservation of mass occurs. However, in 3D with a slab that bends and curves, velocity convergence or divergence can occur, creating violations in conservation of mass in the slab. Because we are using the Boussinesq approximation, conservation of mass must be maintained.

One method we have employed to minimize the divergence in the slab is to prescribe a velocity along the entire subducting slab surface. In this case, the velocity is taken to be parallel to the incoming plate velocity at the surface. With the constrained velocity on the slab surface, we solve for Stokes flow in the entire slab volume. Flow along the slab surface could also follow the steepest descent of the slab. In this case, for each element in the slab surface we find the direction in which water would roll off the element. We then prescribe the velocity in that direction. A third approach to finding the velocity vector that minimizes deformation in the slab is to simply randomly generate the direction of the slab surface velocity, and then choose the velocities in which the second invariant of the strain rate of deformation in the subducting slab is minimized. The question is which of these three methods produces the least amount of deformation to the subducting slab.

To estimate the deformation in the subducting slab, I calculate the second invariant of the strain rate tensor for each slab element.

$$\dot{\epsilon} = \sqrt{1/2 \dot{\epsilon}_{ij}^2} \quad (6)$$

I compare the second invariant of the strain rate tensor for three different velocity prescription techniques: parallel to the incoming plate velocity, in the direction of steepest descent, and random vectors. The only constraint on the random vector was the z-component needed to be in the downward direction since velocity in the slab is downward. Once a random vector was generated, the velocity of the slab was calculated and projected in the direction of the random vector.

I used the same 3D model to test the three velocity methods. The model has 4 km mesh resolution in the mantle wedge, 12 km at the base of the slab, 8 km at the mantle

inflow, and the largest elements in the bottom left corner were 32 km (Figure 36 & 37). The 3D model with this resolution contains ~1.2 million elements.

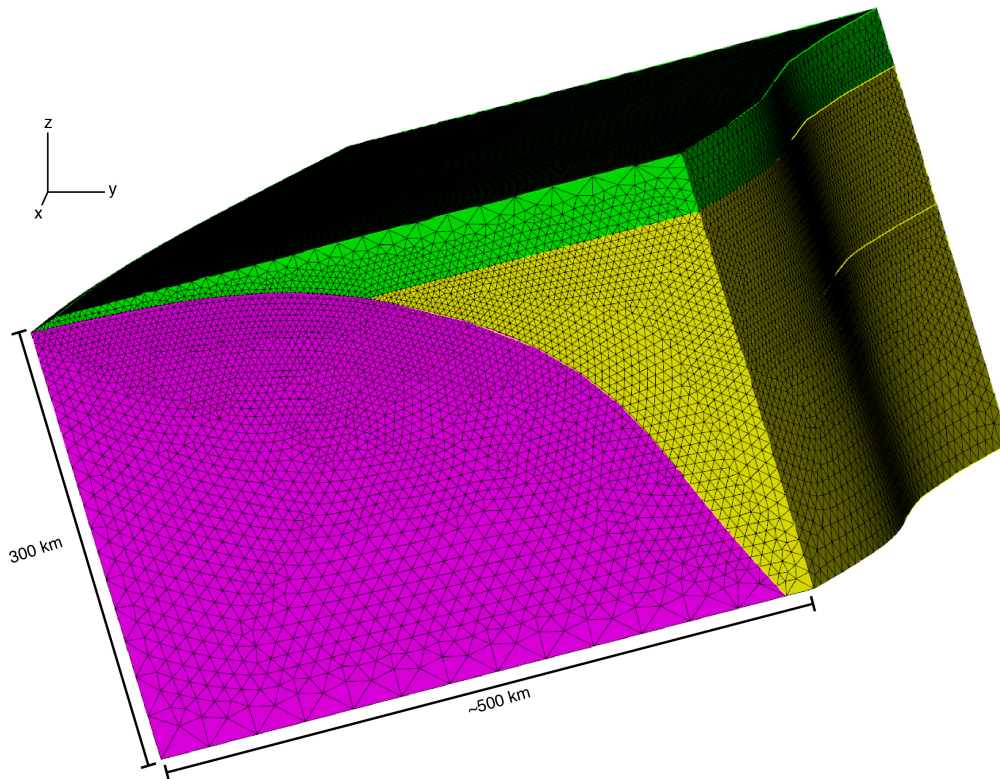


Figure 36: 3D model in which pink is the subducting slab, yellow is the mantle wedge, and green is the overriding plate. Plate convergence is in the positive y-direction.

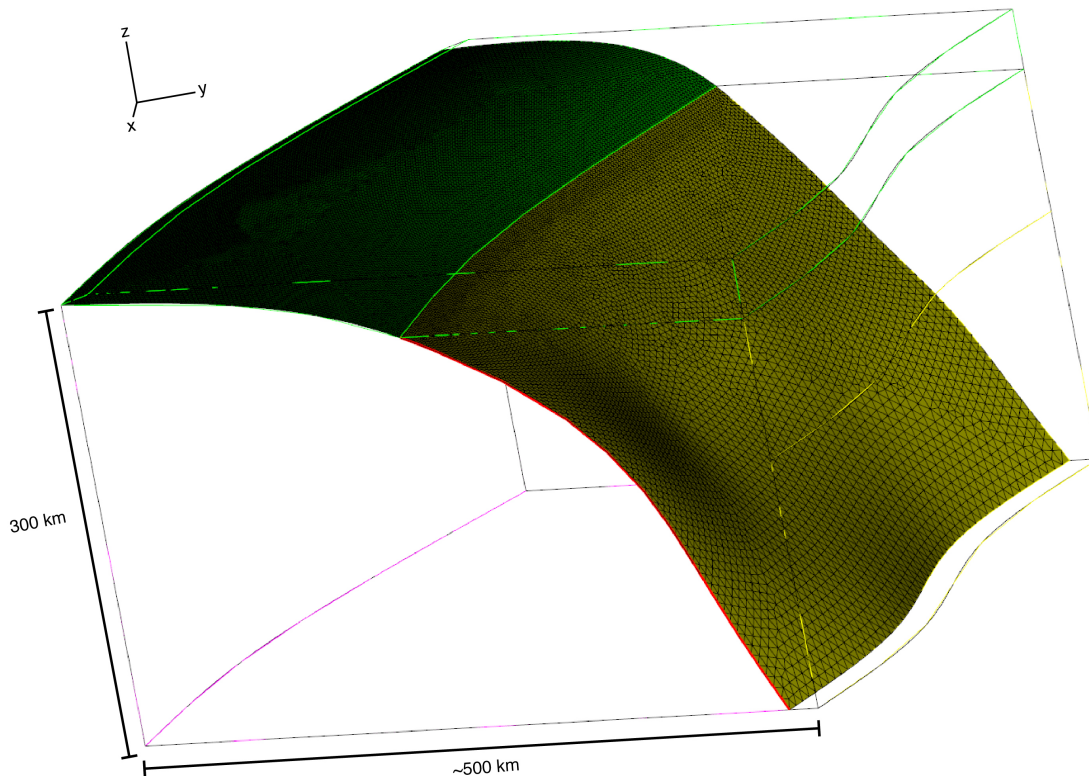


Figure 37: 3D model with the subducting slab show. The mesh resolution is finest at the yellow-green interface of the slab and is 4 km.

For the random vector approach, I tried a total of 50 models. The “best” random vector model (the one in which the second invariant of strain in the slab was lowest) was compared to the model in which velocity was forced to remain parallel to the incoming plate velocity and the steepest descent velocity.

4. Results

4a. Benchmarking 3D code and mesh resolution

I conducted a series of divergence tests of 3D models set up similar to the 2D benchmark models of van Keken et al. (2008). For the case of isoviscous rheology, I found that as coarse as 2 km in the mantle wedge and 10 km for the base of the slab and mantle inflow reproduces the temperatures at 60 km depth on the slab surface and the L2 norm results from 0 to 210 km depth along the slab surface as reported by van Keken et al. (2008) with 1 °C (Table 2; Figure 38 & 39). As the resolution of the 3D models were increased, the temperature at 60 km depth on the slab surface and L2 norm of the slab surface converged on the values reported by van Keken et al. (2008) respectively.

3D Corner points Resolution (km)	Point of (60, 60 km) van Keken et al. (2008) 387.84 °C	L2 norm 0 to 210 km depth van Keken et al. (2008) 503.13 °C
1	387.85	503.19
2	387.43	502.67
3	385.97	501.52

Table 2: Isoviscous model temperature results for three model resolutions at point 60 km depth on the slab surface as well as the L2 norm of the temperature of the slab surface.

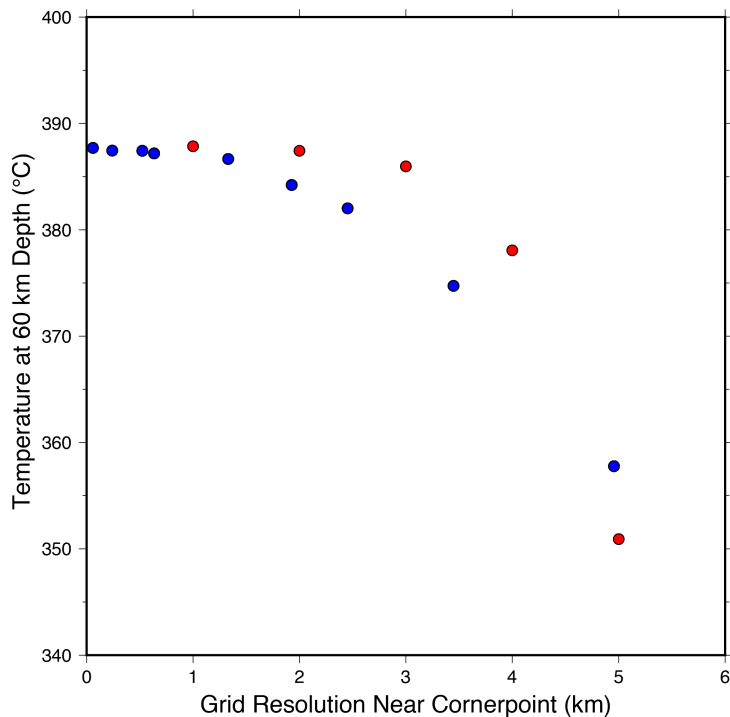


Figure 38: Isoviscous model temperature results at point 60, 60 km depth on the slab surface for varying grid resolutions near the cornerpoint for the 3D benchmark (red) compared to the results from van Keken et al. (2008) (blue).

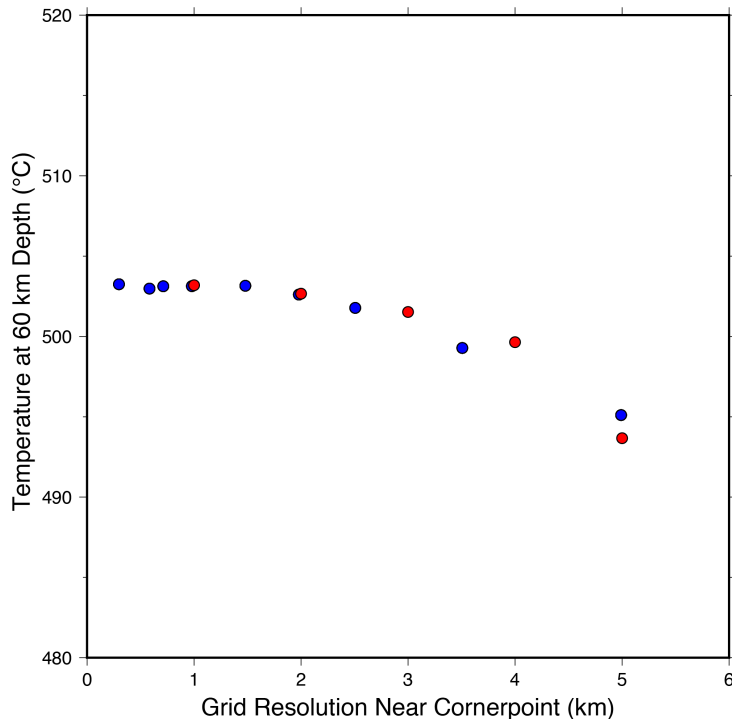


Figure 39: Isoviscous model L2 norm of slab surface temperature from 0 to 210 km for varying grid resolution near cornerpoint (red) compared to results from van Keken et al. (2008) (blue).

When olivine rheology is implemented, the coarsest resolution one can use and still maintain accuracy in the solution is 2 km in the mantle wedge, 7 km in the mantle inflow, and 30 km as the largest element in the mesh. This is more refined than for the isoviscous case.

3D Corner points Resolution (km)	Point of (60,60 km) van Keken et al. (2008) 580.66 °C	L2 norm 0 to 210 km depth van Keken et al. (2008) 607.11 °C
1	576.51	606.60
2	572.48	605.00

Table 3: Olivine rheology model temperature results for three model resolutions at point 60 km depth on the slab surface as well as the L2 norm of the temperature of the slab surface.

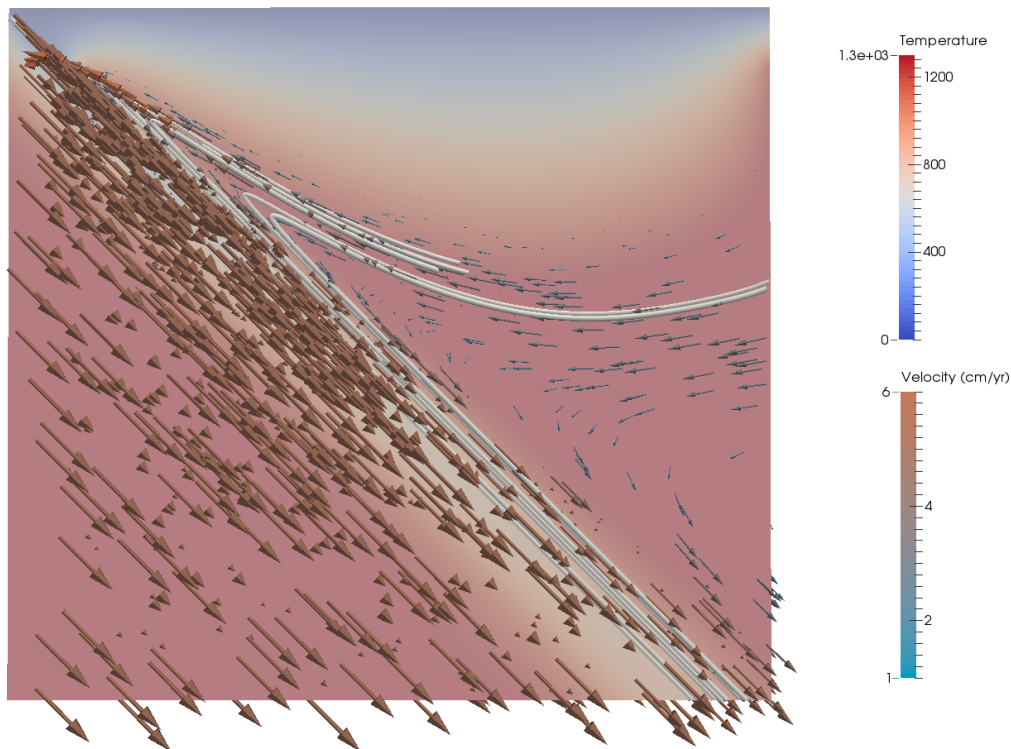


Figure 40: Temperature and velocity field in the 3D benchmark model with olivine rheology.

Velocity vectors for the olivine rheology 3D benchmark are shown in Figure 40 along with the thermal structure of the subducting slab and mantle wedge.

4b. 3D Alaska-Aleutian mesh development

Based on the results from the benchmark testing, I have set the mesh resolution of the entire Alaska-Aleutian arc to be 2 km in the mantle wedge, 7 km in the mantle wedge inflow, and 32 km as the largest element size (Figure 41, 42, 43 and 44). The model extends from the Alaska Peninsula to the western Aleutians with a total number of more than 23 million elements (Figure 41).

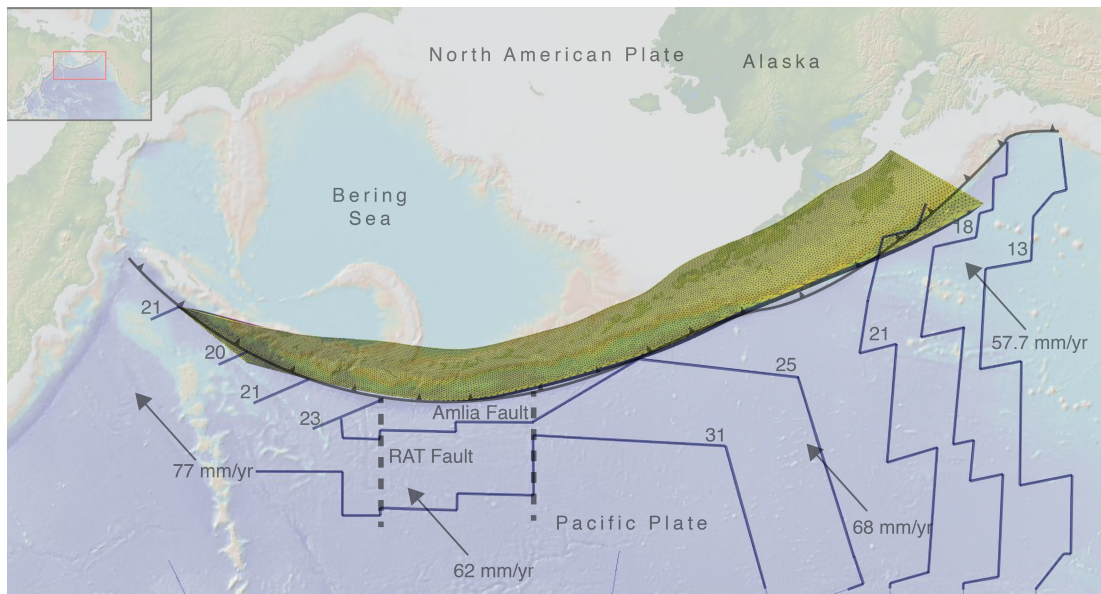


Figure 41: General overlay of meshed subducting slab (yellow) onto Alaska-Aleutian Map

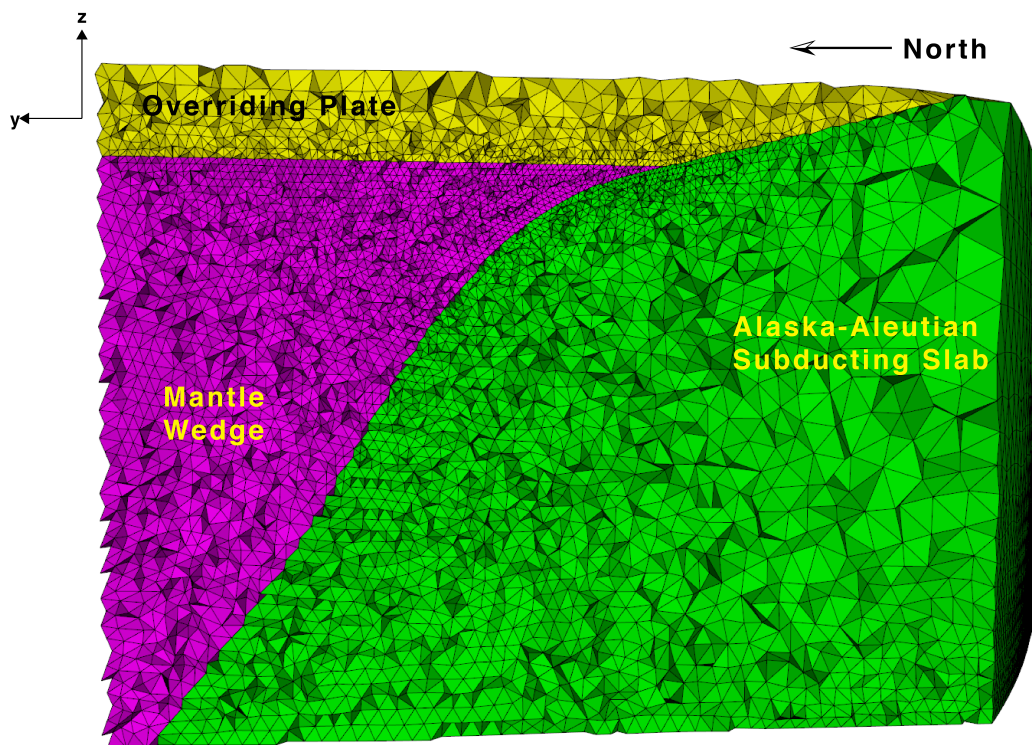


Figure 42: Slice of Alaska-Aleutian 3D mesh from the eastern Aleutians. The mesh resolution is 2 km near the point where the overriding plate, mantle wedge, and slab meet. The resolution is 7 km in the mantle wedge inflow, and 32 km as the largest element size.

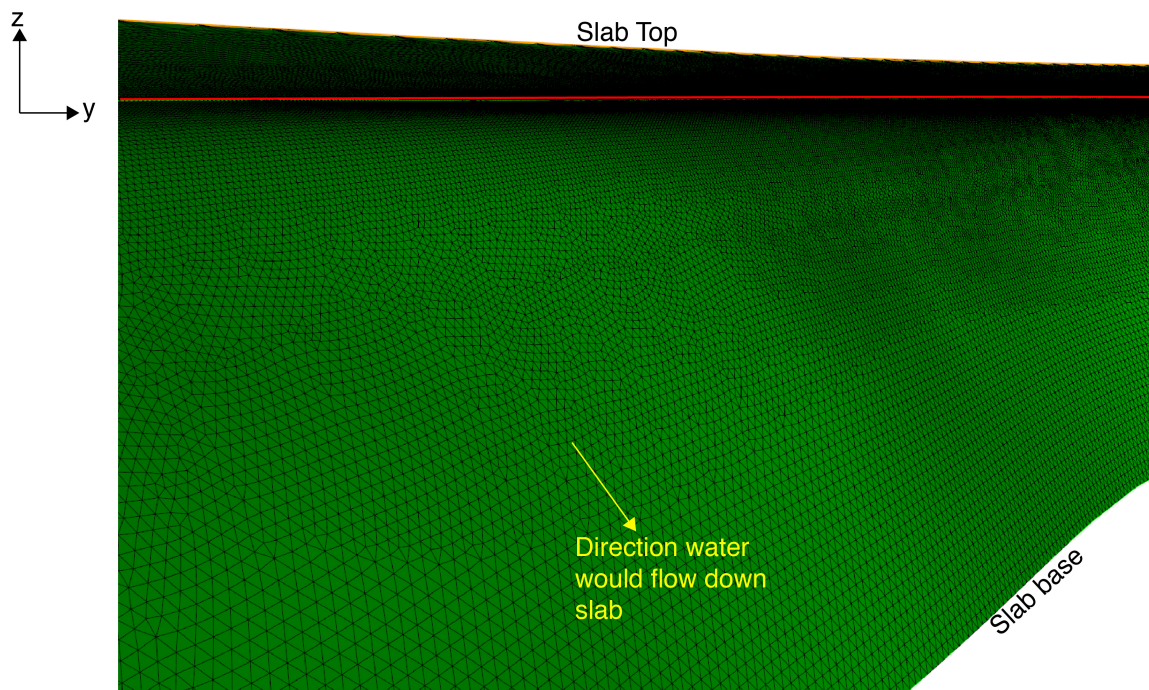


Figure 43: Image of slab surface where red line marks location at which overriding plate, mantle wedge, and slab meet. The resolution is highest near the top of the slab at 2 km and coarsens towards the base at 7 km.

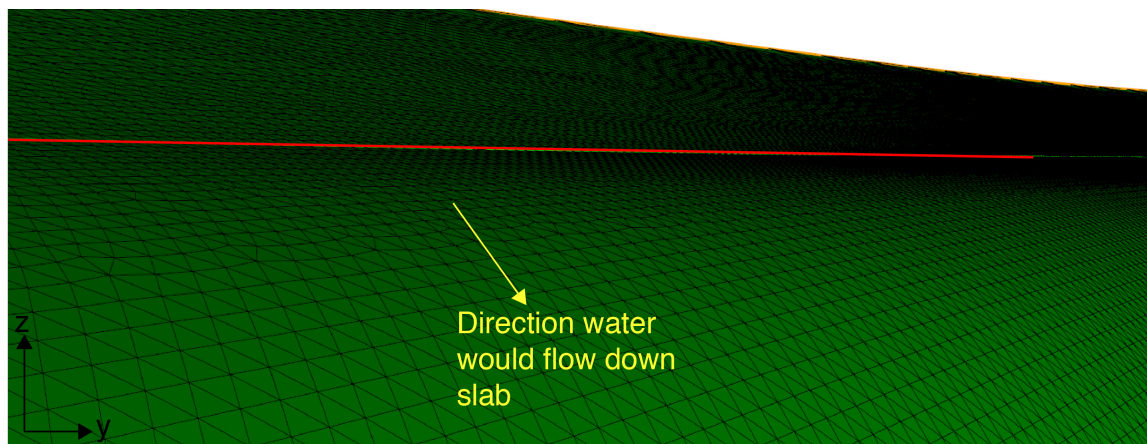


Figure 44: Zoomed in image of slab surface where red line marks location at which overriding plate, mantle wedge, and slab meet.

4c. 2D and 3D model comparison

The comparison of the 2D and 3D models demonstrate that when the models are set up with similar geometry and model parameters, the slab surface temperatures correspond for both the isoviscous and olivine rheology (Figure 45 and 46).

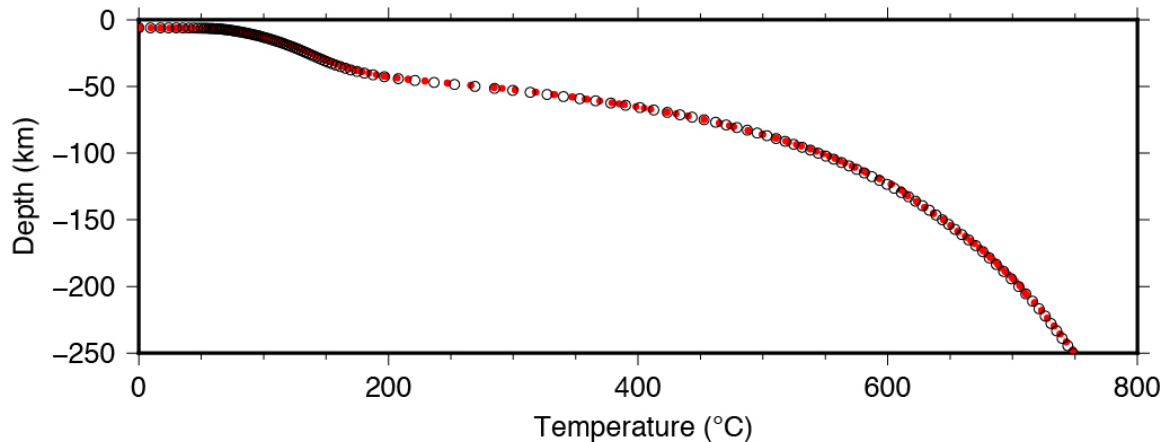


Figure 45: Isoviscous slab surface temperature results for 2D, black open circles, and 3D, red circles.

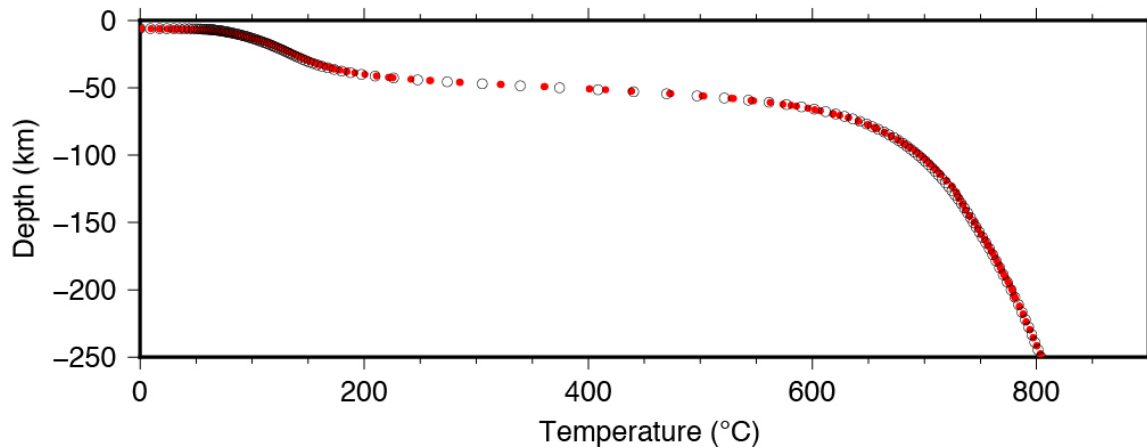


Figure 46: Olivine rheology slab surface temperature results for 2D, black circles, and 3D, red circles.

4d. Slab velocity testing results

To determine the velocity vector along the slab surface that produces the lowest amount of deformation in the slab, I tested three methods of applying velocity. Method one assumes that velocity along the slab surface remained parallel to the incoming plate direction (the “parallel method”). Method two assumed that velocity along the slab surface is in the steepest descent direction of each element (the “steepest descent method”). Finally, in the third method I find the direction of prescribed velocity such that it minimizes the second invariant of the strain rate, an approximation of deformation in the slab. In this last method, I find the velocity vector by randomly generating vectors in a Monte Carlo fashion (the “Monte Carlo method”). Results are presented in Figure 47 and Table 5, which show the second invariant of the strain rate information from a 2D slice taken at $x=1147$ km in the model domain.

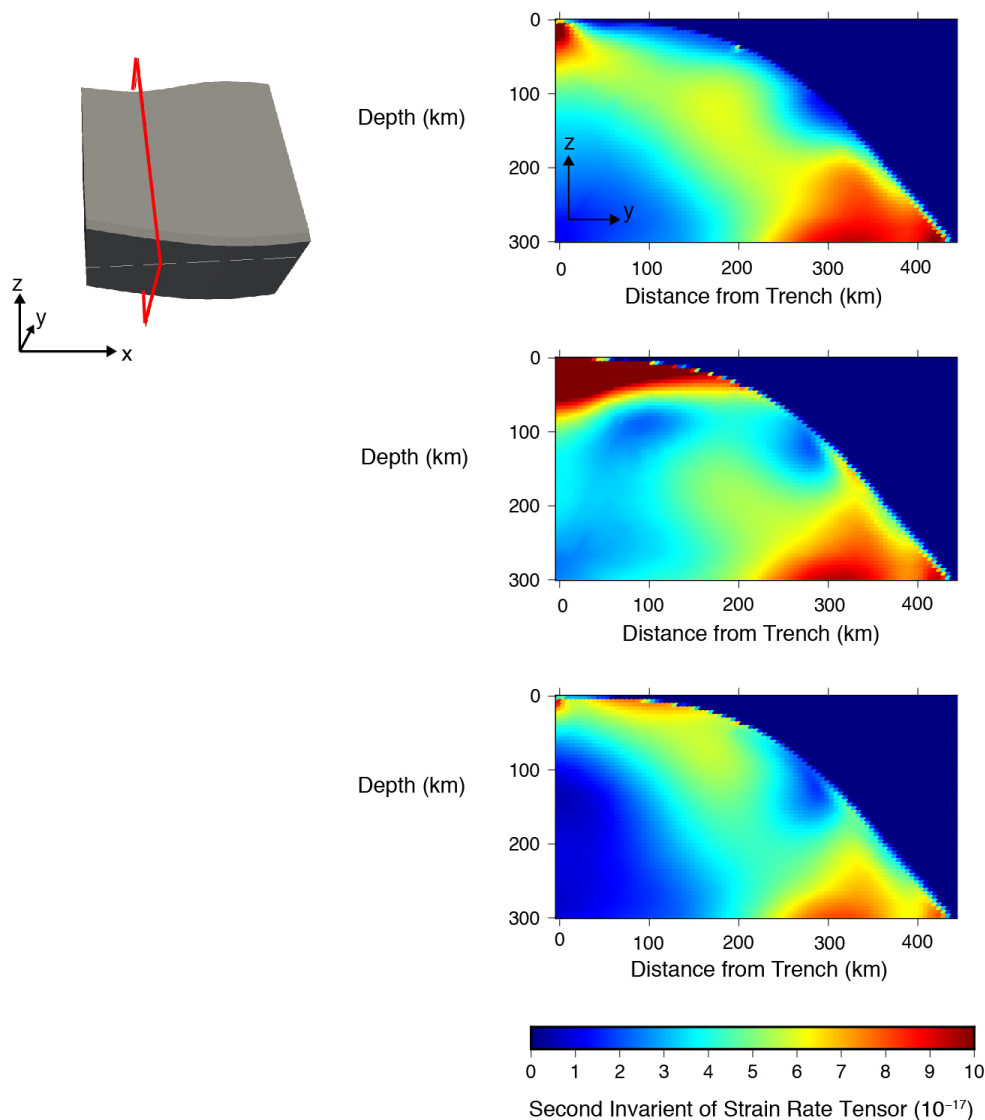


Figure 47: Second invariant of the strain rate tensor for a 2D slice of the 3D model for the parallel method (top), the steepest descent method (middle), and Monte Carlo method (bottom). Top left 3D model outline with red cross-section outlined at $x=1147$ km. Plate motion for 3D block can be visualized as toward the top of the page.

Model Type	Second Invariant sum (s^{-1} , 10^{-12})	Second Invariant mean (s^{-1} , 10^{-16})
Parallel	2.860	5.239
Steepest Descent	4.557	8.210
Monte Carlo	1.508	2.762

Table 5: Summation and mean of the second invariant of the strain rate tensor for each of the three velocity methods tested. The summation and mean are calculated over the entire slab volume.

From these results, the random vector method generates the lowest second invariant of the strain rate. Table 6 shows the average velocity vector of the parallel method, steepest descent, and the best model from the Monte Carlo simulation.

Method	v_x	v_y	v_z
Average Parallel	0	0.7671	-0.4252
Average descent	0.0563	0.7468	-0.4282
Monte Carlo	-0.0369	0.5269	-0.2628

Table 6: Average velocity vectors for the three velocity methods. The average velocity vector of the Monte Carlo approach is the best model of the 50 models tested.

5. Discussion

5a. Benchmark

The results of the 3D benchmarking analysis show that while we can reduce resolution somewhat from the 2D benchmark models of van Keken et al. (2008), the finite element mesh in the mantle wedge still must have nodal spacing of 2 km for flow with olivine rheology to accurately resolve the rapidly changing temperature and pressure of this region. The mantle inflow also must be resolved to at least nodal spacing of 7 km, as the inflow of mantle into the model controls temperatures for the rest of the mantle wedge.

In the isoviscous rheology case, the 3D slab surface temperature agrees with the results reported in van Keken et al. (2008) within one degree for mantle wedge resolution of 1 km and 2 km nodal spacings (Table 2). In the olivine rheology case, even when the 3D models are resolved to 1 km in the mantle wedge and 5 km for mantle inflow, the temperature at the point 60 km depth on the slab surface is nearly 4 °C lower than that reported by van Keken et al. (2008). The slab surface temperature between 0 and 210 km depth are within a degree of that reported in van Keken et al. (2008). The lower temperature of the 3D model resolved to 1 km in the mantle wedge could be accounted for by slight advection across the slab surface in 3D, as observed by Bengtson and van Keken (2012).

For the 3D olivine rheology models, there is a 4 °C difference in temperature at 60 km depth along the slab surface between the 1 km mantle resolution and 2 km resolution. While ideally, we would use a 1 km mantle wedge resolution for all 3D models, because 3D models are much larger this may not always be possible due to constraints on memory and CPU time. Therefore, it is pertinent to ask whether the 4 °C change at a point 60 km deep on

the slab surface affects the location of the metamorphic facies and dehydration reactions. For temperatures less than 600 °C, a depth of 60 km along the slab surface will fall in the broad epidote blueschist stability region, and a change in temperature of 5 °C will not affect the stability of water or metamorphic facies present. The H₂O saturated melting temperature at 60 km depth occurs just above 600 °C (van Keken et al., 2011). Therefore if we expected temperatures greater than 600 °C, a 5 °C change resulting from finite element nodal spacings from 1 km to 2 km may impact the geochemical interpretation of the models. However, for a temperature greater than 600 °C to occur 60 km deep in the slab, the velocity of the incoming plate would have to be less than 5 cm/yr which does not occur anywhere on the Alaska-Aleutian Arc. Furthermore, the temperature between 0 and 210 km depth based on the L2 norm of the 2 km grid resolution is within 1 °C of the 1 km resolution. Hence, while the 3D model with 2 km grid resolution at shallow slab depths do not exactly match the 3D model with 1 km grid resolution, the differences will not impact the metamorphic facies or dehydration reaction interpretations of the large Alaska-Aleutian model.

5b. Mesh development in Trelis

One of the benefits of using Trelis is that its GUI interface allows the user to see the 3D geometry as it is being developed. Users can build the geometry from the command line by entering commands to create a vertex, curve, surface etc. The user can also use a command panel, allowing the user to select to create a vertex for example without typing the exact language for the command. Trelis allows the user to build complex geometries. Once the geometry is built, Trelis provides a series of geometry diagnostic testing to check for things such as overlapping surfaces, too small angles, or small surfaces. This checking feature allows the user to optimize the geometry and eliminate errors.

A common problem that occurs in building complex geometries is overlapping surfaces. Some of these issues can be resolved in Trelis by merging all surfaces. However, a simple merge does not always fix all overlapping surfaces. In subduction zone geometries, the most common area this occurs is the slab surface. In order to merge overlapping surfaces, for example two surfaces outlining the shallow slab surface, Trelis requires the curves to exactly match. If the curves do not exactly match, which is almost always the case, the user must collapse curves on one of the surfaces. For example, the shallow slab surface should be defined by four curves, two of the curves being the top of the spline defining the slab shape, a curve separating the deep slab surface from the shallow slab surface, and a curve at the edge of the model (Figure 48). Often times Trelis will dice up one of these curves into several smaller curves. The smaller curves must be collapsed until there are only four curves making up the shallow slab surface for each surface that must be merged. Then a forced merge can take place, eliminating the problem of overlapping shallow slab surfaces.

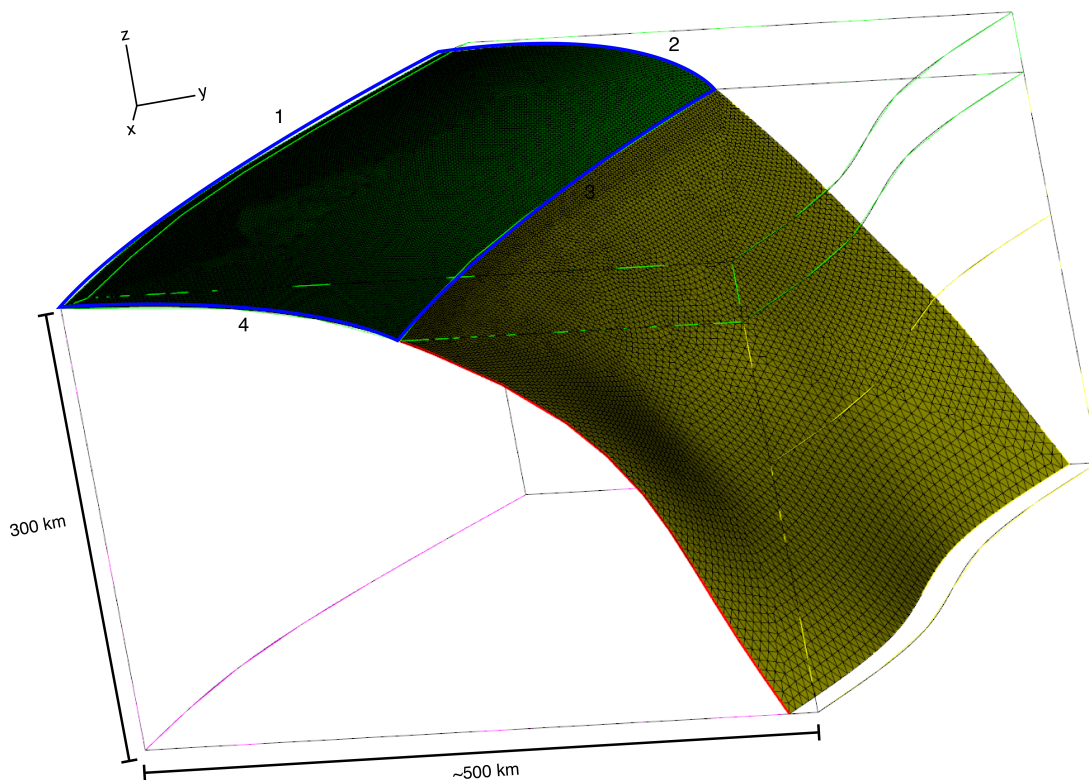


Figure 48: Shallow slab surface outlined in 4 blue curves. Trelis frequently divides up the four curves outlining the shallow slab surface into many smaller curves. These smaller curves must be collapsed before two overlapping shallow slab surface can be forced merged. The issue of overlapping surfaces, especially on the shallow and deep slab is common in Trelis. It is also often necessary to need to collapse curves before merging.

Trelis allows the user to define the meshing scheme and resolution by direct command line entries for each curve, surface, or volume. Trelis also can build the mesh automatically. I use a combination of the two meshing techniques. We want the finest resolution in the areas where velocity and temperature are changing rapidly. For the subduction zone, this region is near the point where the overriding plate, subducting slab, and mantle meet. We also want the models to be resolved near the mantle inflow region. The most efficient means of building the finite element mesh is to define the desired mesh resolution of the slab inflow, slab surface, and mantle and slab inflow and outflow surfaces. Once those three surfaces have the finite element mesh applied with the necessary variable resolution, I use the automatic meshing tool in Trelis to mesh the entire volume. Trelis fills in the mesh with elements according to the specified mesh resolutions.

5c. 2D vs. 3D mesh comparison

In the 2D and 3D model comparison, the 3D slab surface corresponds to the 2D but is extended into the third dimension. The slab surface temperature of the 2D and 3D models correspond, indicating that the 3D model is solving the thermal and velocity

structure accurately. However, to better determine the 3D models solution accuracy to 2D, I need a more refined mesh. At this time, the current version of Sepran does not allow for a more refined 3D mesh to be calculated. The 3D model with 3 km nodal spacing in the mantle wedge contains more than 2 million elements. The Fortran memory limit on one core is 4 Gb. From my model testing, I have found a rough estimate that 2 million elements requires 4 Gb of memory. I cannot run a 3D model with the resolution necessary for an accurate solution with the current limitation of Sepran.

Besides memory, CPU time can also be a limiting factor in running large 3D subduction zone models. I calculated the CPU time required to run 3D olivine rheology models with varying resolution. The results show that for every $\sim 10,000$ element increase in the model an addition one minute of computation time is required (Figure 49). By this estimate, a 23 million elements model would require around 35 hours to run on one core. Therefore CPU time is not a limiting factor in the large, subduction zone model runs using the Sepran finite element package.

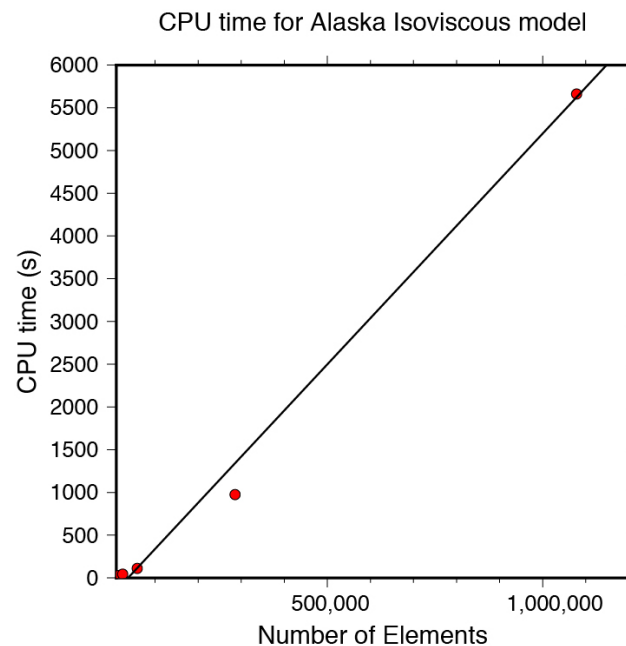


Figure 49: CPU time versus number of elements for olivine rheology 3D model. The CPU time increases roughly 1 minute for 10,000 additional elements, which means a model of 23 million elements would take about 35 hours to run on one core.

5d. Velocity in the slab

A 3D slab flow model that minimizes deformation in the slab was first done by Creager and Boyd (1991) with a 3D kinematic slab model of the Aleutian subduction zone. They assume that particles within the cold, strong slab follow a path of least deformation rate. To estimate that particle path, they used the position of three particles, x_{i-1} , x_i , and x_{i+1} , at three different times, $t - \tau$, t , $t + \tau$ (Figure 50). From the nine position points marked (small circles in Figure 50) they calculated six mean position points (large circles in Figure 50) and velocity vectors. The authors then varied flow as an inverse problem to find the

minimization of the volume integral of the square of the effective strain rate in the slab, a measure of slab deformation. Because of computational limits more than 20 years ago, Creager and Boyd (1991) based the deformation in the slab only on six velocity vectors. Their models also assumed isoviscous rheology. My tests of flow in a 3D model follow the same logic as Creager and Boyd (1991), minimization of the strain rate in the slab, but I am able to calculate the second invariant of the strain rate tensor for each element in the entire slab volume. Furthermore I use olivine rheology for both the mantle wedge and subducting slab.

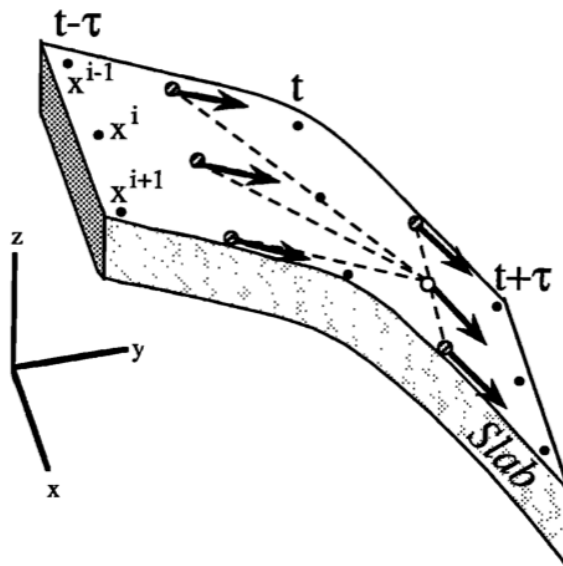


Figure 50: Illustration from Creager and Boyd (1991) that describes the grid they used to calculate the strain field. The small black circles are the three position vectors x_{i-1} , x_i , and x_{i+1} , at three different time steps $t - \tau$, t , $t + \tau$. The position of these particles is held fixed at time $t - \tau$, and t while those at $t + \tau$ are iteratively varied to minimize the second invariant of the strain rate.

At first glance, the results of testing the three methods to determine the prescribed velocity on the slab surface shows that choosing the best random vector as the direction of flow in the slab produces the least amount of slab deformation. However, at closer examination this may not be the case because the higher strain rates in the parallel and steepest descent method is caused by a few incorrect velocity vectors (Figure 51 and 52) which is not present in the Monte Carlo method (Figure 53).

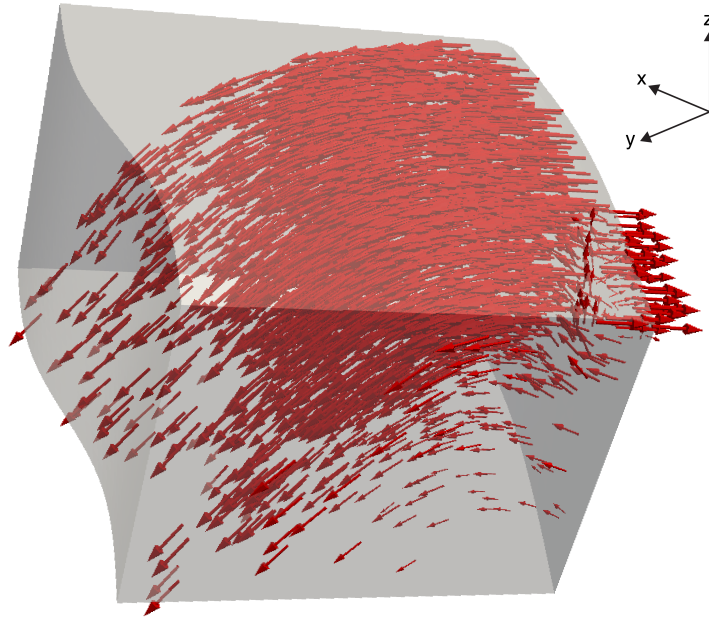


Figure 51: Velocity vectors for parallel method. The velocity vectors follow the direction parallel to incoming plate velocity except in a small corner at the shallow portion of the incoming plate.

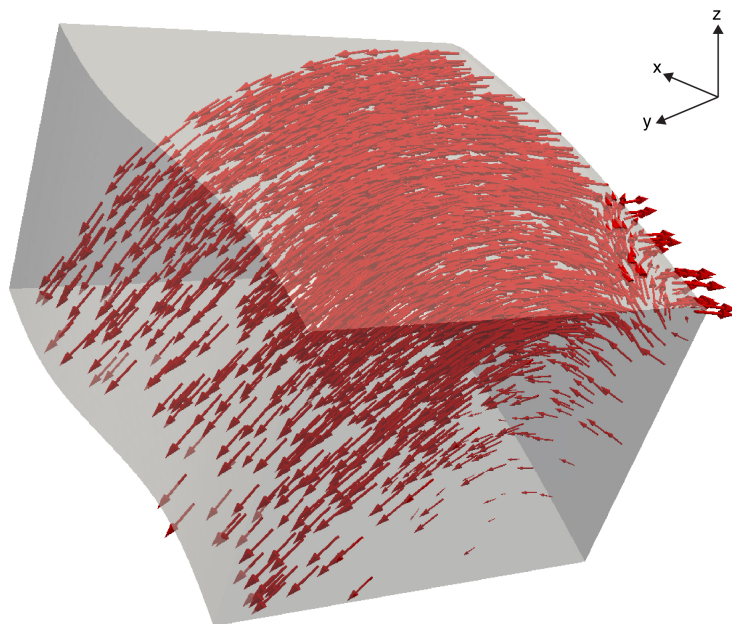


Figure 52: Velocity vectors for the steepest descent method. The velocity vectors follow the direction of steepest descent except in a small corner at the shallow portion of the incoming plate.

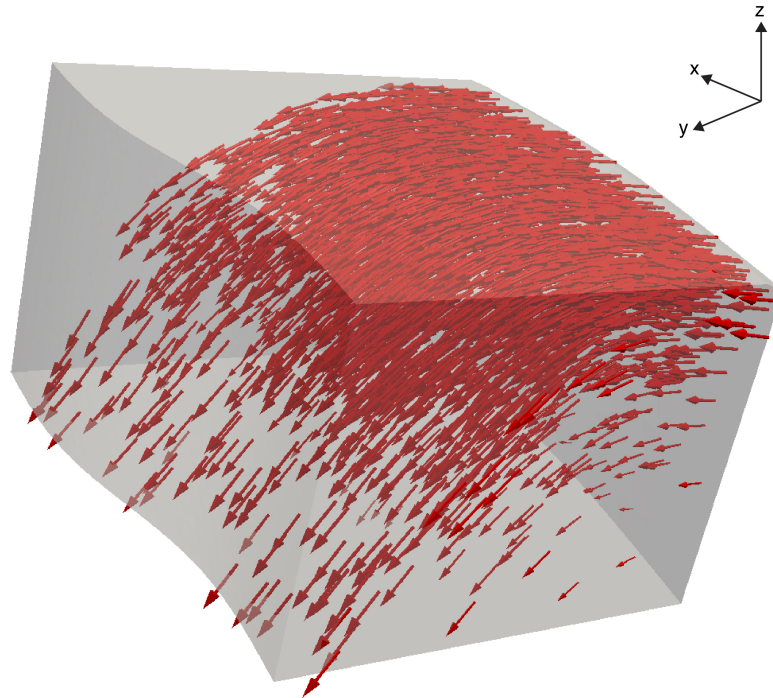


Figure 53: Velocity vector of best model in the Monte Carlo method

In both the parallel and steepest descent method, there is a region in which the velocity vectors are pointed opposite the direction of the incoming plate (Figure 51 and 52). The reason for the wrong vectors in the parallel method is that in order to find a velocity on each element, the element normal is crossed with the negative x vector $(-1,0,0)$ which gives the vector parallel to the incoming plate, perpendicular to $(-1,0,0)$, on the element surface. However, elements that are very shallow (less than 6 km depth) have a nearly horizontal dip in many places so that the element normal is nearly parallel to the z-axis (average normal vector $(-0.03, 0.31, -13.88)$). When the negative x vector is crossed with the nearly z vector, the resulting vector can point either in the positive y or negative y direction. The code as it is written now checks that the resulting vector is pointed in the downward direction so that flow does not go up the slab. However the code does not check that the vector is in the positive y direction so that flow moves in the same direction as the incoming plate. Therefore I added a second code check to guarantee that the flow moves both in the same direction as the incoming plate and the downward direction. When the negative y vectors are flipped, the deep red or high areas of second invariant of the strain rate tensor are reduced significantly (Figure 54).

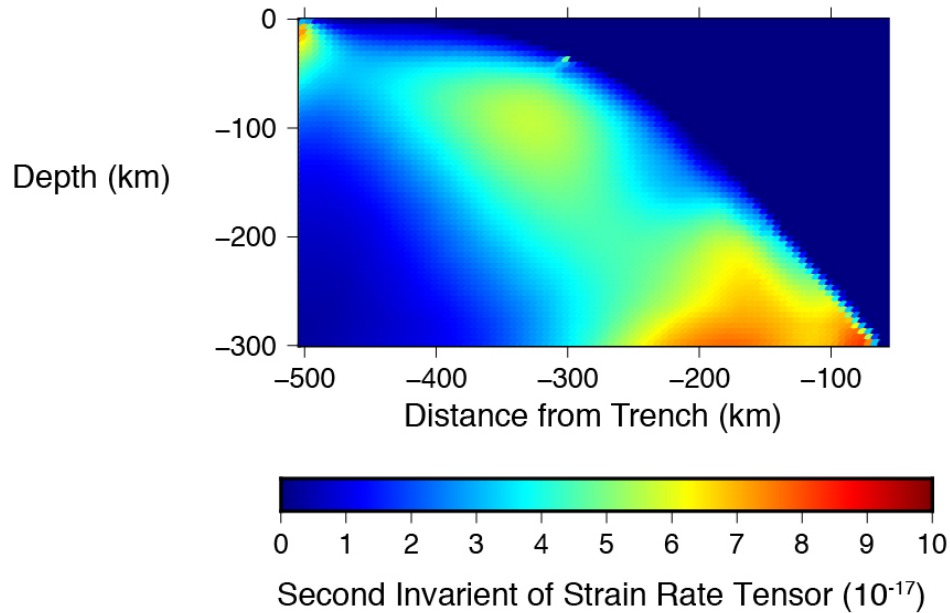


Figure 54: Cross-section plot of the second invariant of strain rate for parallel method with the vector correction such that slab flow cannot be in the opposite direction of the incoming plate velocity.

In the steepest descent method the velocity vector is defined in the direction of element dip. For the nearly horizontal elements, the element dip is ambiguous and could point in any direction. As a result the check I used in the parallel method to flip the vector from the negative y to positive y does not work. A possible solution to this problem is to use the parallel method for the shallow, nearly horizontal elements, and the steepest descent method for the deeper elements. The question then becomes what is the best depth to switch from the parallel method to the steepest descent method. I tested this by varying the depth of the switch from the parallel method to steepest descent method from 10 km depth to 200 km depth in 10 km increments. The results show that placing the switch between 160 and 180 km depth produces the lowest second invariant of the strain rate and reduces small areas of high strain rate (Figure 55).

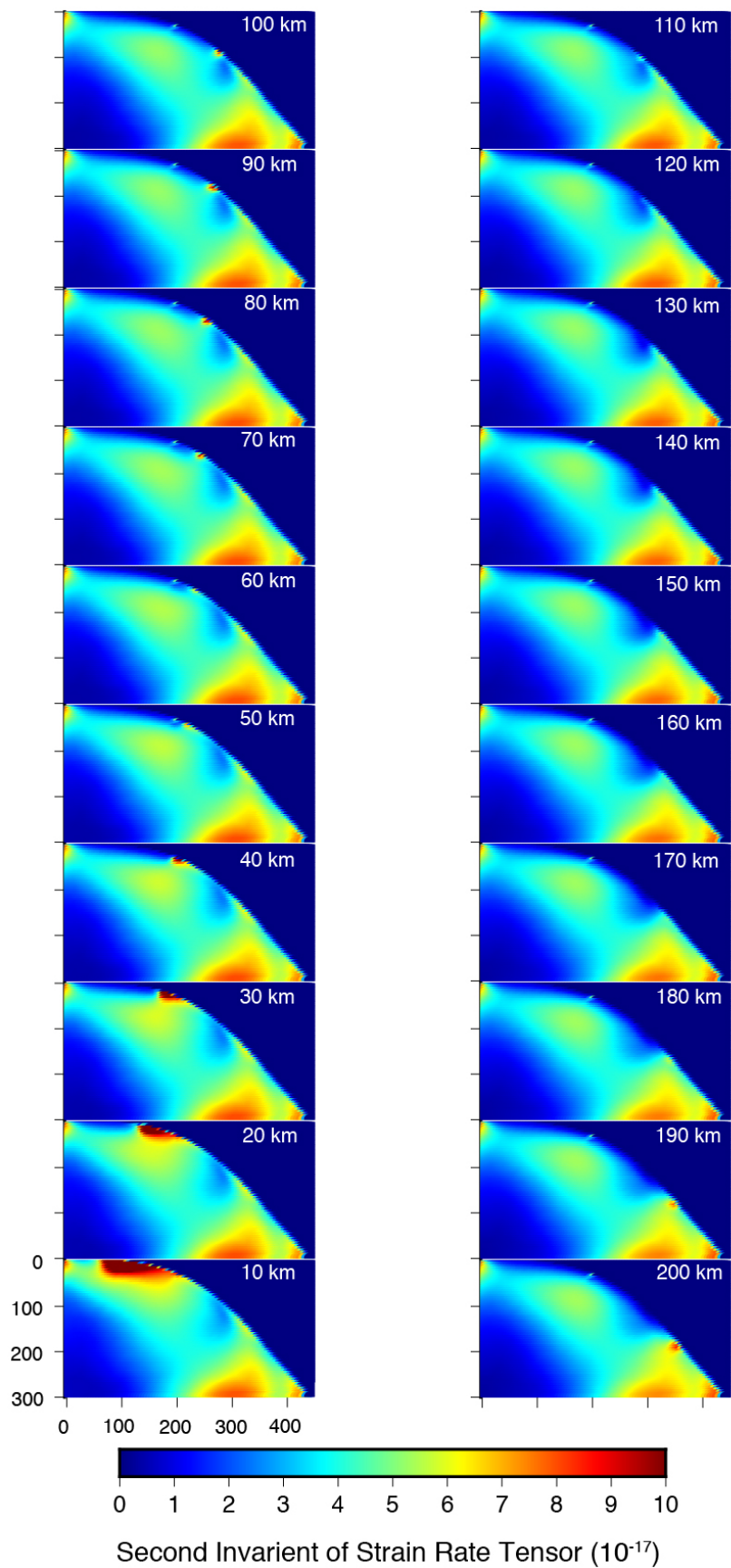


Figure 55: Cross-section plot of the second invariant of the strain rate tensor for models utilizing both the parallel method (shallow) and steepest descent method (deep). The depth at which the parallel method is switched to the steepest descent method is written on the figure in white.

Therefore I conclude that when using the Boussinesq approximation to solve for flow in the subducting slab, the best method directing velocity which prevents deformation of the slab is a combination of defining the velocity vector parallel to the incoming plate to ~ 170 km depth and defining the vector in the direction of element dip from 170 km to 300 km depth. The result that a generally parallel to the incoming plate velocity agrees with Creager and Boyd (1991) who found that slab particles follow paths close to but not exactly the same as the velocity of the incoming plate.

Now that it is clear that the best model contains vectors that change with depth, I went back to the Monte Carlo simulation to examine if different random vectors produced lower second invariant of the strain rate for different depths. I found the model that produced the lowest sum of the second invariant of the strain rate for depths 0 to 50 km, 51 to 100 km, 101 to 200 km, 201 to 250 km, and 251 to 300 km depth. The best x-component of the random vector between depths between 0 and 200 km was on the order of 10^{-2} , indicating a nearly parallel direction with the incoming plate. Between 201 and 300 km depth, the best x-component vector varied away from the nearly parallel direction (Table 7). The Monte Carlo approach then agrees with my results that, in general, a velocity vector nearly parallel to the incoming plate velocity vector produces the least slab deformation.

Depth (km)	Vector x	Vector y	Vector z
50	0.022	0.366	-0.931
100	0.027	0.171	-0.985
150	0.027	0.171	-0.985
200	0.027	0.171	-0.985
250	0.120	0.644	-0.756
300	-0.181	0.512	-0.840

Table 7: Starting vector for best model, model with lowest summation of second invariant of strain rate, for different depths

6. Conclusion

Full 3D models of the Alaska-Aleutian Arc are a key piece to understanding the complexities of the subduction zone, such as changes in arc water content along arc, shear wave splitting directions, and the nature of disparities and locked regions of the subducting and overriding plate. However, it is clear from the resolution testing I conducted, that a full

3D finite element mesh of the Alaska-Aleutian arc will require more than 23 million elements. As a result, the Sepran code that is based in Fortran 77 must be setup for parallel computing. Finally a complex issue of large 3D models with variably shaped slabs is solving for slab velocity while still maintain the Boussinesq approximation. A possible solution to this problem is to prescribe slab velocity parallel to the incoming plate down to 170 km depth. Between 170 km to 300 km depth a method of steepest descent (direction water would roll off element) should be utilized. The combination of prescribing velocity on the slab surface parallel to incoming plate velocity to a depth of 170 km followed by the steepest descent method to 300 km depth produces the least deformation in the subducting slab with the Stokes flow solution.

- Abers G. A. (2005) Seismic low-velocity layer at the top of subducting slabs: observations, predictions, and systematics. *Physics of the Earth and Planetary Interiors* **149**, 7–29.
- Abers G. A., van Keken P. E., Kneller E. A., Ferris A. and Stachnik J. C. (2006) The thermal structure of subduction zones constrained by seismic imaging: Implications for slab dehydration and wedge flow. *Earth and Planetary Science Letters* **241**, 387–397.
- Arndt N. T. and Goldstein S. L. (1989) An open boundary between lower continental crust and mantle: its role in crust formation and crustal recycling. *Tectonophysics* **161**, 201–212.
- Barcheck C. G., Wiens D. A., van Keken P. E. and Hacker B. R. (2012) The relationship of intermediate- and deep-focus seismicity to the hydration and dehydration of subducting slabs. *Earth and Planetary Science Letters* **349-350**, 153–160.
- Bengtson A. K. and van Keken P. E. (2012) Three-dimensional thermal structure of subduction zones: effects of obliquity and curvature. *Solid Earth* **3**, 365–373.
- Billen M. I. and Jadamec M. (2012) Origin of localized fast mantle flow velocity in numerical models of subduction. *Geochem. Geophys. Geosyst.* **13**, 1–16.
- Braile L. W., Hinze W. J., Frese von R. R. B. and Keller G. R. (1989) Chapter 28: Seismic properties of the crust and uppermost mantle of the conterminous United States and adjacent Canada. *Geological Society of America Memoirs* **172**, 655–680.
- Brophy J. G. (1986) The Cold Bay Volcanic Center, Aleutian Volcanic arc. *Contrib Mineral Petrol* **93**, 368–380.
- Brown J. R., Prejean S. G., Beroza G. C., Gomberg J. S. and Haeussler P. J. (2013) Deep low-frequency earthquakes in tectonic tremor along the Alaska-Aleutian subduction zone. *J. Geophys. Res.* **118**, 1079–1090.
- Burk C. A. (1965) Geology of the Alaska Peninsula and island arc and continental margin (part 1). *Geological Society of America Memoirs* **99**, 1–265.
- Christensen D. H. and Abers G. A. (2010) Seismic anisotropy under central Alaska from SKS splitting observations. *J. Geophys. Res.* **115**, 1–12.
- Clague D. A. (1981) Linear Island and Seamount Chains Aseismic Ridges and Intraplate Volcanism Results from Dsdp. *The Society of Economic Paleontologists and Mineralogists* **32**, 7–22.
- Clift P. (2004) Controls on tectonic accretion versus erosion in subduction zones: Implications for the origin and recycling of the continental crust. *Rev. Geophys.* **42**, 1–31.

- Conrad W. K. and Kay R. W. (1984) Ultramafic and Mafic Inclusions from Adak Island: Crystallization History, and Implications for the Nature of Primary Magmas and Crustal Evolution in the Aleutian Arc. *Journal of Petrology* **25**, 88–125.
- Creager J. S. and Scholl D. W. (1973) Deep Sea Drilling Project Initial Reports Volume 19. 1–14.
- Creager K. C. and Boyd T. M. (1991) The geometry of Aleutian subduction: Three-dimensional kinematic flow model. *Journal of Geophysical Research: Solid Earth (1978–2012)* **96**, 2293–2307.
- Cuvelier C., Segal A. and Van Steenhoven A. A. (1986) *Finite element methods and Navier-Stokes equations*, Springer Science & Business Media.
- DeMets C., Gordon R. G. and Argus D. F. (1994) Effect of recent revisions to the geomagnetic reversal time scale on estimates of current plate motions. *Geophysical research Letters* **21**, 2191–2194.
- Divins D. L. (2002) *Total sediment thickness of the world's oceans and marginal seas*, NOAA National Geophysical Data Center, See <http://www.ngdc.noaa.gov/mgg/sedthick/sedthick>.
- Dobson D. P., Meredith P. G. and Boon S. A. (2002) Simulation of Subduction Zone Seismicity by Dehydration of Serpentine. *Science* **298**, 1407–1410.
- Ekström G. and Nettles M. eds. (2013) Global CMT catalog search. Available at: <http://www.globalcmt.org/CMTsearch.html>.
- Emry E. L. and Wiens D. A. (2015) Incoming plate faulting in the Northern and Western Pacific and implications for subduction zone water budgets. *Earth and Planetary Science Letters* **414**, 176–186.
- Engelbreton D. C., Cox A. and Gordon R. G. (1985) Relative Motions Between Oceanic and Continental Plates in the Pacific Basin. *Geological Society of America Special Papers* **206**, 1–60.
- Faccenda M., Gerya T. V. and Burlini L. (2009) Deep slab hydration induced by bending-related variations in tectonic pressure. *Nature Geoscience* **2**, 790–793.
- Ferris A., Abers G. A., Christensen D. H. and Veenstra E. (2003) High resolution image of the subducted Pacific (?) plate beneath central Alaska, 50–150 km depth. *Earth and Planetary Science Letters* **214**, 575–588.
- Finney B., Turner S., Hawkesworth C., Larsen J., Nye C., George R., Bindeman I. and Eichelberger J. (2008) Magmatic Differentiation at an Island-arc Caldera: Okmok Volcano, Aleutian Islands, Alaska. *Journal of Petrology* **49**, 857–884.

- Fischer K. M., Fouch M. J., Wiens D. A. and Boettcher M. S. (1998) Anisotropy and Flow in Pacific Subduction Zone Back-arcs. *Pure and Applied Geophysics* **151**, 463–475.
- Fliedner M. M. and Klemperer S. L. (2000) Crustal structure transition from oceanic arc to continental arc, eastern Aleutian Islands and Alaska Peninsula. *Earth and Planetary Science Letters* **179**, 567–579.
- Fliedner M. M. and Klemperer S. L. (1999) Structure of an island-arc: Wide-angle seismic studies in the eastern Aleutian Islands, Alaska. *Journal of Geophysical Research: Solid Earth (1978–2012)* **104**, 10667–10694.
- Fournelle J. H. and Marsh B. D. (1994) Age, character, and significance of Aleutian arc volcanism. **G-1**, 723–757.
- Freytmuller J. T., Woodard H., Cohen S. C., Cross R., Elliott J., Larsen C. F., Hreinsdóttir S. and Zweck C. (2008) Active Deformation Processes in Alaska, Based on 5 Years of GPS Measurements. 1–42.
- Frohlich C. (1989) The nature of deep-focus earthquakes. *Rev. Earth Planet. Sci.* **17**, 227–254.
- George R. (2003) Melting processes and fluid and sediment transport rates along the Alaska-Aleutian arc from an integrated U-Th-Ra-Be isotope study. *J. Geophys. Res.* **108**, 2252–25.
- Grove T. L., Parman S. W., Chatterjee N. and Médard E. (2006) The influence of H₂O on mantle wedge melting. *Earth and Planetary Science Letter* **249**, 74–89.
- Gust D. A. and Perfit M. R. (1987) Phase relations of a high-Mg basalt from the Aleutian Island Arc: Implications for primary island arc basalts and high-Al basalts. *Contrib Mineral Petrol* **97**, 7–18.
- Hacker B. R. (2008) H₂O subduction beyond arcs. *Geochem. Geophys. Geosyst.* **9**, 1–24.
- Hacker B. R., Yin A., Christie J. M. and Snoke A. W. (1990) Differential stress, strain rate, and temperatures of mylonitization in the Ruby Mountains, Nevada: Implications for the rate and duration of uplift. *Journal of Geophysical Research: Solid Earth (1978–2012)* **95**, 8569–8580.
- Haeussler P. J., Coe R. S. and Onstott T. C. (1992) Paleomagnetism of the Late Triassic Hound Island Volcanics: Revisited. *J. Geophys. Res.* **97**, 19–617–19–639.
- Hanna J. and Long M. D. (2012) SKS splitting beneath Alaska: Regional variability and implications for subduction processes at a slab edge. *Tectonophysics* **530-531**, 272–285.

- Hasegawa A., Nakajima J., Uchida N., Okada T., Zhao D., Matsuzawa T. and Umino N. (2009) Plate subduction, and generation of earthquakes and magmas in Japan as inferred from seismic observations: An overview. *Gondwana Research* **16**, 370–400.
- Hein J. R., Scholl D. W. and Miller J. (1978) Episodes of Aleutian Ridge explosive volcanism. *Science* **199**, 137–141.
- Hillhouse J. W. (1987) Accretion of southern Alaska. *Tectonophysics* **139**, 107–122.
- Hillhouse J. W. and Coe R. S. (1994) *Paleomagnetic data from Alaska*, The Geological Society of America.
- Hiramatsu Y., Ando M., Tsukuda T. and Ooida T. (1998) Three-dimensional image of the anisotropic bodies beneath central Honshu, Japan. *Geophysics* **135**, 801–816.
- Holbrook W. S., Lizarralde D., McGeary S., Bangs N. and Diebold J. (1999) Structure and composition of the Aleutian island arc and implications for continental crustal growth. *Geol* **27**, 31–34.
- International Seismological Center (2009) EHB Bulletin. Available at: <http://www.isc.ac.uk>.
- Ishikawa T. and Nakamura E. (1994) Origin of the slab component in arc lavas from across-arc variation of B and Pb isotopes. *Nature* **370**, 205–208.
- Iwamori H. (2004) Phase relations of peridotites under H₂O-saturated conditions and ability of subducting plates for transportation of H₂O. *Earth and Planetary Science Letters* **227**, 57–71.
- Janiszewski H. A., Abers G. A., Shillington D. J. and Calkins J. A. (2013) Crustal structure along the Aleutian island arc: New insights from receiver functions constrained by active-source data. *Geochem. Geophys. Geosyst.* **14**, 2977–2992.
- Jarrard R. D. (2003) Subduction fluxes of water, carbon dioxide, chlorine, and potassium. *Geochem. Geophys. Geosyst.* **4**, 1–50.
- Karato S.-I. and Wu P. (1993) Rheology of the Upper Mantle: A synthesis. *Science* **260**, 771–778.
- Kay S. M. and Kay R. W. (1994) Aleutian magmas in space and time. *The Geological Society of America* **G-1**, 687–722.
- Kelemen P. B. (1995) Genesis of high Mg# andesites and the continental crust. *Contrib Mineral Petrol* **120**, 1–19.

- Kelemen P. B., Yogodzinski G. M. and Scholl D. W. (2003) Along—Strike Variation in the Aleutian Island Arc: Genesis of High Mg# Andesite and Implications for Continental Crust. *Inside the Subduction Factory*.
- Kincaid C. and Griffiths R. W. (2003) Geochemical evidence for efficient aquifer isolation over geological timeframes. *Nature* **425**, 55–58.
- Kirby S. H. and Kronenberg A. K. (1987) Rheology of the lithosphere: selected topics. *Rev. Geophys.* **25**, 1219–1244.
- Kirby S., Engdahl R. E. and Denlinger R. (1996) *Intermediate-Depth Intraslab Earthquakes and Arc Volcanism as Physical Expressions of Crustal and Uppermost Mantle Metamorphism in Subducting Slabs*, American Geophysical Union.
- Kissling E. and Lahr J. C. (1991) *Tomographic image of the Pacific slab under southern Alaska*, *Ecolgae Geologicae Helvetiae*.
- Kita S., Okada T., Nakajima J., Matsuzawa T. and Hasegawa A. (2006) Existence of a seismic belt in the upper plane of the double seismic zone extending in the along-arc direction at depths of 70–100 km beneath NE Japan. *Geophys. Res. Lett.* **33**, 1–5.
- Kneller E. A. and van Keken P. E. (2008) Effect of three-dimensional slab geometry on deformation in the mantle wedge: Implications for shear wave anisotropy. *Geochemistry* **9**, 1–21.
- Kneller E. A., Long M. D. and van Keken P. E. (2008) Olivine fabric transitions and shear wave anisotropy in the Ryukyu subduction system. *Earth and Planetary Science Letters* **268**, 268–282.
- Kneller E. A., van Keken P. E., Karato S.-I. and Park J. (2005) B-type olivine fabric in the mantle wedge: Insights from high-resolution non-Newtonian subduction zone models. *Earth and Planetary Science Letters* **237**, 781–797.
- Kneller E. A., van Keken P. E., Katayama I. and Karato S. (2007) Stress, strain, and B-type olivine fabric in the fore-arc mantle: Sensitivity tests using high-resolution steady-state subduction zone models. *J. Geophys. Res.* **112**, 1–17.
- Larsen J., Neal C., Webley P. and Freymueller J. (2009) Eruption of Alaska volcano breaks historic pattern. *Geophysical research Letters* **90**.
- Lee C. and King S. D. (2009) Effect of mantle compressibility on the thermal and flow structures of the subduction zones. *Geochem. Geophys. Geosyst.* **10**, 1–24.
- Lefeldt M., Grevemeyer I., Goßler J. and Bialas J. (2009) Intraplate seismicity and related mantle hydration at the Nicaraguan trench outer rise. *Geophysical Journal International* **178**, 742–752.

- Long M. D. and Silver P. G. (2008) The Subduction zone flow field from seismic anisotropy: a global view. *Science* **319**, 312–315.
- Lonsdale P. (1988) Paleogene history of the Kula plate: Offshore evidence and onshore implications. 733–754.
- Marsh B. D. and Leitz R. E. (1979) Geology of Amak Island, Aleutian Islands, Alaska. *The Journal of Geology* **87**, 715–723.
- Marshak S. and Repcheck J. (2004) *Essentials of geology*,
- McClelland W. C., Gehrels G. E. and Saleeby J. B. (1992) Upper Jurassic-Lower Cretaceous Basinal Strata Along the Cordilleran Margin: Implications for the Accretionary History of the Alexander-Wrangellia-Peninsular Terrane. *Tectonics* **11**, 823–835.
- McLennan S. M. and Taylor S. R. (1982) Geochemical constraints on the growth of the continental crust. *The Journal of Geology* **90**, 347–361.
- Müller R. D., Roest W. R., Royer J. Y., Gahagan L. M. and Sclater J. G. (1997) Digital isochrons of the world's ocean floor. *Journal of Geophysical Research: Solid Earth (1978–2012)* **102**, 3211–3214.
- Myers J. D. (1988) Possible petrogenetic relations between low- and high-MgO Aleutian basalts. **100**, 1040–1053.
- Myers J. D. and Marsh B. D. (1987) Aleutian lead isotopic data: additional evidence for the evolution of lithospheric plumbing systems. *Geochimica et Cosmochimica Acta* **51**, 1833–1842.
- Myers J. D., Frost C. D. and Anglewine C. L. (1986) A test of a quartz eclogite source for parental Aleutian magmas: A mass balance approach. *Journal of Geology* **94**, 811–828.
- Myers J. D., Marsh B. D. and Sinha K. (1985) Strontium isotopic and selected trace element variations between two Aleutian volcanic centers (Adak and Atka): implications for the development of arc volcanic plumbing systems. *Contrib Mineral Petrol* **91**, 221–234.
- Nakajima J. and Hasegawa A. (2004) Shear-wave polarization anisotropy and subduction-induced flow in the mantle wedge of northeastern Japan. *Earth and Planetary Science Letters* **225**, 365–377.
- Nakajima J., Uchida N., Shiina T., Hasegawa A., Hacker B. R. and Kirby S. H. (2013) Intermediate-depth earthquakes facilitated by eclogitization-related stresses. *Geol* **41**, 659–662.
- National Geophysical Data Center (2015) National Geophysical Data Center/World Data Service (NGDC/WDS): Global Historical Tsunami Database. Available at: http://ngdc.noaa.gov/hazard/tsu_db.shtml.

- Nikolas I Christensen W. D. M. (1995) Seismic velocity structure and composition of the continental crust: A global view. *J. Geophys. Res.* **100**, 9761–9788.
- Peacock S. M. (1999) Seismic Consequences of Warm Versus Cool Subduction Metamorphism: Examples from Southwest and Northeast Japan. *Science* **286**, 937–939.
- Plafker G. (1969) The Alaska Earthquake. *Geological Survey Professional Paper*, 1–88.
- Plafker G. and Berg H. (1994) The Geology of Alaska. *The Geological Society of America* **G-1**, 1–16.
- Plank T. and Langmuir C. H. (1998) The chemical composition of subducting sediment and its consequences for the crust and mantle. *Chemical Geology* **145**, 325–394.
- Polet J., Silver P. G., Beck S., Wallace T., Zandt G., Ruppert S., Kind R. and Rudloff A. (2000) Shear wave anisotropy beneath the Andes from the BANJO, SEDA, and PISCO experiments. *Journal of Geophysical Research: Solid Earth (1978–2012)* **105**, 6287–6304.
- Raleigh C. B. and Paterson M. S. (1965) Experimental deformation of serpentinite and its tectonic implications. *J. Geophys. Res.* **70**, 3965–3985.
- Ratchkovsky N. A. and Hansen R. A. (2002) New Evidence for Segmentation of the Alaska Subduction Zone. *Bulletin of the Seismological Society of America* **92**, 1754–1765.
- Ratchkovsky N. A., Pujol J. and Biswas N. N. (1997) Stress pattern in the double seismic zone beneath Cook Inlet, south-central Alaska. *Tectonophysics* **281**, 163–171.
- Rea D. K. and Dixon J. M. (1983) Late Cretaceous and Paleogene tectonic evolution of the north Pacific Ocean. *Earth and Planetary Science Letters* **65**, 145–166.
- Ringwood A. E. (1974) The petrological evolution of island arc systems Twenty-seventh William Smith Lecture. *Journal of the Geological Society* **130**, 183–204.
- Rossi G., Abers G. A., Rondenay S. and Christensen D. H. (2006) Unusual mantle Poisson's ratio, subduction, and crustal structure in central Alaska. *J. Geophys. Res.* **111**, 1–16.
- Rudnick R. L. (1995) Making continental crust. *Nature* **378**, 571–578.
- Rudnick R. L. and Fountain D. M. (1995) Nature and composition of the continental crust: a lower crustal perspective. *Rev. Geophys.* **33**, 267–309.
- Ryan H. F. and Scholl D. W. (1993) Geologic implications of great interplate earthquakes along the Aleutian arc. *Journal of Geophysical Research: Solid ...* **98**, 22–135–22–146.
- Schmidt M. W. and Poli S. (1998) Experimentally based water budgets for dehydrating slabs and consequences for arc magma generation. *Earth and Planetary Science Letters* **163**, 361–379.

- Scholl D. W. and Huene von R. (2007) Crustal recycling at modern subduction zones applied to the past—Issues of growth and preservation of continental basement crust, mantle geochemistry, and supercontinent reconstruction. In *4-D Framework of Continental Crust* Geological Society of America Memoirs. Geological Society of America. pp. 9–32.
- Scholl D. W., Vallier T. L. and Stevenson A. J. (1987) Geologic Evolution and Petroleum Geology of the Aleutian Ridge. **6**, 123–155.
- Scholl D. W., Vallier T. L. and Stevenson A. J. (1982) Sedimentation and Deformation in the Amlia Fracture-Zone Sector of the Aleutian Trench. *Marine Geology* **48**, 105–134.
- Shillington D. J., Van Avendonk H., Holbrook W. S., Kelemen P. B. and Hornbach M. J. (2004) Composition and structure of the central Aleutian island arc from arc-parallel wide-angle seismic data. *Geochem. Geophys. Geosyst.* **5**, 1–32.
- Smith G. P., Wiens D. A., Fischer K., Dorman L. M., Webb S. C. and Hildebrand J. A. (2001) A complex flow pattern of mantle flow in the Lau backarc. *Science* **292**, 709–713.
- Smithson S. B., Johnson R. A. and Wong Y. K. (1981) Mean crustal velocity: a critical parameter for interpreting crustal structure and crustal growth. *Earth and Planetary Science Letters* **53**, 323–332.
- Stein C. A. and Stein S. (1992) A model for the global variation in oceanic depth and heat flow with lithospheric age. *Nature* **359**, 123–129.
- Stephens C. D., Fogleman K. A., Lahr J. C. and Page R. A. (1984) Wrangell Benioff zone, southern Alaska. *Geol* **12**, 373–376.
- Stover C. W. and Coffman J. L. (1991) *Seismicity of the United States, 1568-1989 (Revised)*,
- Strak V. and Schellart W. P. (2014) Evolution of 3-D subduction-induced mantle flow around lateral slab edges in analogue models of free subduction analysed by stereoscopic particle image velocimetry technique. *Earth and Planetary Science Letters* **403**, 368–379.
- Syracuse E. M. and Abers G. A. (2006) Global compilation of variations in slab depth beneath arc volcanoes and implications. *Geochem. Geophys. Geosyst.* **7**, 1–18.
- Syracuse E. M., van Keken P. E. and Abers G. A. (2010) The global range of subduction zone thermal models. *Physics of the Earth and Planetary Interiors* **183**, 73–90.
- Talley H. C. and Cloud W. K. (1962) United States earthquakes, 1960.
- Taylor S. R. (1967) The origin and growth of continents. *Tectonophysics* **4**, 17–34.
- Thatcher W. (1990) Order and diversity in the modes of Circum-Pacific Earthquake recurrence. *Journal of Geophysical Research: Solid Earth (1978–2012)* **95**, 2609–2623.

- USGS (2013) M8.3 Sea of Okhotsk. *USGS Earthquake Summary*. Available at: http://earthquake.usgs.gov/earthquakes/eventpage/usb000h4jh#general_summary [Accessed November 29, 2015].
- Vallier T. L., Scholl D. W., Fisher M. A. and Bruns T. R. (1994) *Geologic framework of the Aleutian arc, Alaska*, The Geological Society of America.
- van Keken P. E. (2003) The structure and dynamics of the mantle wedge. *Earth and Planetary Science Letters* **215**, 323–338.
- van Keken P. E., Currie C., King S. D., Behn M. D., Cagnioncle A., He J., Katz R. F., Lin S.-C., Parmentier E. M., Spiegelman M. and Wang K. (2008) A community benchmark for subduction zone modeling. *Physics of the Earth and Planetary Interiors* **171**, 187–197.
- van Keken P. E., Hacker B. R., Syracuse E. M. and Abers G. A. (2011) Subduction factory: 4. Depth-dependent flux of H₂O from subducting slabs worldwide. *J. Geophys. Res.* **116**, 1–15.
- van Keken P. E., Kiefer B. and Peacock S. M. (2002) High-resolution models of subduction zones: Implications for mineral dehydration reactions and the transport of water into the deep mantle. *Geochem. Geophys. Geosyst.* **3**, 1–20.
- Van Wormer J. D., Davies J. and Gedney L. (1974) Seismicity and plate tectonics in South Central Alaska. *Bulletin of the Seismological Society of America* **64**, 1467–1475.
- Wada I. and Wang K. (2009) Common depth of slab-mantle decoupling: Reconciling diversity and uniformity of subduction zones. *Geochem. Geophys. Geosyst.* **10**, 1–26.
- Wiens D. A. and Smith G. P. (2003) Seismological constraints on structure and flow patterns within the mantle wedge. *Geophysical Monograph-American*.
- Yamasaki T. (2003) Double seismic zone and dehydration embrittlement of the subducting slab. *J. Geophys. Res.* **108**, 2212.
- Yang X., Fischer K. M. and Abers G. A. (1995) Seismic anisotropy beneath the Shumagin Islands segment of the Aleutian-Alaska subduction zone. *Journal of Geophysical Research: Solid Earth (1978–2012)* **100**, 18165–18177.
- Zhao D., Christensen D. H. and Pulpan H. (1995) Tomographic imaging of the Alaska subduction zone. *J. Geophys. Res.*, 1–18.
- Zimmer M. M., Plank T., Hauri E. H., Yogodzinski G. M., Stelling P., Larsen J., Singer B., Jicha B., Mandeville C. and Nye C. J. (2010) The Role of Water in Generating the Calc-alkaline Trend: New Volatile Data for Aleutian Magmas and a New Tholeiitic Index. *Journal of Petrology* **51**, 2411–2444.